

**DEVELOPMENT OF A NEW HIGH-STRESS
DYNAMIC-LOADING RING-SHEAR
APPARATUS AND ITS APPLICATION TO
LARGE-SCALE LANDSLIDES**

Dang Quang Khang

2015

**DEVELOPMENT OF A NEW HIGH-STRESS
DYNAMIC-LOADING RING-SHEAR
APPARATUS AND ITS APPLICATION TO
LARGE-SCALE LANDSLIDES**

(動的載荷高圧リングせん断試験機の開発と大
規模地すべりへの適用)

by

Dang Quang Khang

A dissertation

**Submitted in partial fulfillment of the requirements for the
Degree of Doctor of Engineering**

Department of Civil and Earth Resources Engineering

Kyoto University, Japan

September 2015

Acknowledgements

This research has been carried out from October 2012 to September 2015 in the Innovative Disaster Prevention Technology and Policy Research Section (Takara Lab.) of the Division of Disaster Management for Safe and Secure Society, the Disaster Prevention Research Institute (DPRI), Kyoto University, and also in the Laboratory by the UNESCO-Kyoto University-International Consortium on Landslides (ICL) joint programme. During studying time in Japan, I have received great and valuable supports and encouragements from the professors, researchers, colleagues, friends, and family members.

First and foremost, I would like to express my deep appreciation and thanks to my respected professors, Professor Emeritus Kyoji SASSA, Executive Director of the ICL, who invited to join to ICL as a researcher contributing to a Japan-Vietnam joint project, and Professor Kaoru TAKARA, Director of the DPRI who accepted me to become a doctoral student in his Laboratory. They have continuously guided, supported and advised me from the very beginning of this research.

I would also like to thank Prof. Yasuto Tachikawa, Assoc. Prof. Sunmin Kim, Prof. Bin He, Dr. Osamu Nagai, Prof. Masahito Ishihara, Assoc. Prof. Takahiro Sayama and other professors in Kyoto University and ICL for their valuable guidance, suggestions, and discussions.

I take this opportunity to show my sincere gratitude to Prof. Mai Trong Nhuan, and Assoc. Prof. Do Minh Duc in Vietnam National University (VNU) who recommended me as a joint researcher of the Japan-Vietnam joint project, and have always encouraged and supported me in research as well as in life. I also would like to thank VNU University of Science, the Institute of Transport Science and Technology of the Ministry of Transport for giving me a chance to take this doctoral course at Kyoto University.

In addition, I wish to express gratitude to all of the staff members of the ICL office and Takara Laboratory: Mrs. Mie Ueda, Ms. Kumiko Fujita, Ms. Waka Kataoka, Mrs. Sono Inoue, Mrs. Mayumi Nishimura, Ms. Saho Matsuda, and Mrs. Kaori Saidera for their kind assistance for my working and studying life in Japan.

I would like to give my thanks to colleagues in Takara Laboratory for their useful suggestions and friendship during the course of research: Mr. PingPing Luo, Ms.

Tomoko Teramoto, Ms. Maja Ostric, Mrs. Nor Eliza Binti Alias, Mr. Weili Duan, Mr. Bounhieng Vilaysane, Mr. Josko Troselj, Mr. Hendy Setiawan, Mr. Han Xue, Mr. Masaki Azuma, Mr. Maochuan Hu, Mr. Toshiharu Sasaki, Mr. Shota Kurokawa, Mr. Doan Huy Loi, Mr. Pham Van Tien, Mr. Adnan Arutyunov, Mr. Tsukawa Goto, Mr. Yohei Kurose, Mr. Emmanuel Akpabio, Ms. Chong Khai Lin, Ms. Eva Mia Siska, and Ms. Karlina.

I am very grateful to the GCOE-ARS Program “Sustainability/Survivability Science for a Resilient Society Adaptable to Extreme Weather Conditions” of Kyoto University. And I wish to thank for all Marui & Co., Ltd. members, especially to Mr. Yuji Ikari, Mr. Osamu Hiroi, and Mr. Takaaki Hirano for their instruction, help and improvement for the practical use of the new ring-shear apparatus.

A special thanks to my family. Words cannot express how grateful I am to my mother, my father, my mother-in-law, my father-in-law, and all other family members for their endless support and encouragement. I am also thankful to my friends here (Mr. Châu Lân, Mrs. Quỳnh Anh, Mr. Quang Minh, Mr. Ngọc Hòa, Mr. Hữu Thọ, Mr. Phạm Tiền, Mrs. Hương Trà, Mr. Nguyễn Hoàng, Mr. Xuân Tráng, Mr. Huy Lợi, Mr. Tấn Bùi, Mr. Cảnh Hào, Mr. Hồ Lam, Mr. Thanh Mến, and all others) who helped to make my stay in Japan a very pleasant one.

At the end I would like to express appreciation to my beloved wife Lam Ngọc who has always stood by me, supported me to stick on to the difficult task of writing the thesis.

Kyoto, September 2015

Abstract

There are many historical and recent megaslides and large-scale landslides which may trigger Tsunami, landslide dams and causing great debris flows or floods as well as causing direct damages. Some cases of megaslides have been studied in detail such as the 2006 Leyte landslide in the Philippines, the 2008 Aratozawa landslide in Japan. The depths of these megaslides are from 120 m to 200m (Leyte landslide), or over 150 m (Aratozawa landslide). But dynamics of such megaslides has not been well-studied so far. It is needed to develop a reliable and effective tools for studying the mechanism and hazard assessing for those landslides kind.

DPRI series (from the model DPRI-1 through DPRI-2, 3, 4, 5, 6, 7) and ICL-1 ring-shear apparatus developed by Professor Sassa were great success in reproducing sliding-surface formation and measuring post-failure motion in rain-and earthquake-induced landslides. In spite of getting such many successes but these devices could not apply to large-scale landslides and megaslides which have the depth of over 100 m in depth, greater than 10 million m³ in volume causing a great effect either on land, coastal or under water.

The undrained ring shear apparatus ICL-1 was improved to maintain the undrained state up to 1000 kPa in 2011. Based on this result, the ICL group has designed a new high-stress ring-shear apparatus ICL-2 to simulate the initiation and motion of megaslides in 2012. The ICL-2 apparatus was expected to test very deep landslides with the capacity of maintaining an undrained state up to 3 MPa, namely around 200m deep landslides can be simulated effectively. The author has had a great opportunity for contributing to develop the new apparatus and used the results obtained from it to fulfill this thesis.

The concept, design, construction and testing procedures of the latest ring-shear apparatus ICL-2 were presented in chapter 2. The greatest difference between ICL devices and other in DPRI series is the system for loading normal stress. Model DPRI has a long loading frame consisting of two long vertical pillars and one horizontal beam. In ICL-2, the loading frame was removed and the loading system was replaced by a loading piston. The normal stress acting on the sliding surface (upward) is retained by the central axis (downward), and this load is measured by the vertical load cell (N). The change in loading system contributed to high-stress achievement of ICL-2.

Another significant difference between the DPRI series apparatus and the ICL-2 series is the rubber edge which has a critical role for sealing. Rubber edges of all DPRI series apparatus were glued to the shear box. A constant thickness of glue is impossible to achieve and the height of the upper surfaces of the rubber edges of the inner ring and the outer ring must be the equal to maintain an undrained condition. In the ICL-2, the rubber edges are fixed without glue. The rubber edge is simply placed on the lower ring and pressed by a Teflon ring holder, and this holder is pressed in turn by a steel ring holder fixed by a set of screws.

ICL-2 was created to be used for basis tests to determine soil parameters and for the landslide simulation tests. The difference is in the size and level of stress and shearing speed. Model ICL-1 is small, lightweight and transportable and capable of testing up to 1 MPa at low shearing speed (5.4 cm/s), Model ICL-2 was designed for up to 3 MPa and up to 50 cm/s.

Two real cases of large-scale landslide were applied to ICL-2. The first is the historical 1792 Unzen-Mayuyama megaslide in Japan triggered by an earthquake and the second is the active Hai Van large-scale landslide in Viet Nam. A series of tests were conducted on the samples taken from the two landslides to examine the performance of the new high-stress ring-shear apparatus as well as to simulate initiation and motion of the landslides. The tests results indicated that undrained tests were successful up to 3 MPa in the monotonic speed-control test, monotonic stress control test, pore-water pressure control test, cyclic-shear-stress loading test and seismic-shear-stress loading test using the real earthquake records.

Then, all parameters measured from the undrained ring-shear tests were applied to the integrated landslide simulation model (LS-RAPID) for studying the mechanism of the historical 1792 Unzen-Mayuyama megaslide and assess the hazard of the active Hai Van landslide. The simulation results of the former landslide triggered by an earthquake indicated that the hazard area and its central section were similar to actual landslide. In case of the latter landslide, we input a pore-water pressure ratio as the triggering factor and other parameters obtained from the ring-shear tests and our field investigation to the computer simulation. The mechanism and hazard area of the Hai Van landslide have been demonstrated.

These applications of the new high-stress dynamic-loading ring-shear apparatus to the large-scale landslides showed that the device and the integrated computer simulation are effective tools for understanding the mechanism of the large-scale landslides and their hazard assessment.

Table of Contents

List of Figures	vii
List of Tables	x
Chapter 1 Introduction	1
1.1 Background for this Study	4
1.2 Research Objectives	5
1.3 Thesis Outline	6
Chapter 2 Development of a New High-Stress Dynamic-Loading Ring-Shear Apparatus (ICL-2)	9
2.1 Introduction to Ring-Shear Apparatus	9
2.2 Purposes to Develop the New High-Stress Dynamic-Loading Ring-Shear Apparatus	12
2.3 Design and Construction of the New Ring-Shear Apparatus ICL-2	13
2.3.1 Design	13
2.3.2 Construction	14
2.4 Testing Procedures	22
2.4.1 Rubber Edge Friction Checking	22
2.4.2 Sample Saturation	23
2.4.3 Saturation Checking	24
2.4.4 Sample Consolidation	24
2.4.5 Shearing	25
Chapter 3 Application of the New High-Stress Dynamic-Loading Ring-Shear Apparatus to Large-Scale Landslides	27
3.1 Introduction of Studied Landslides	27
3.1.1 The Historical 1792 Unzen-Mayuyama Megalide in Japan	27
3.1.2 The Recent Hai Van Large-Scale Landslide in Vietnam	32
3.2 Basic Tests of the ICL-2	40

3.2.1 <i>Drained Speed Control Test</i>	41
3.2.2 <i>Undrained Stress Control Test</i>	42
3.3 ICL-2 Tests for Simulating Initiation and Motion of the Landslides	46
3.3.1 <i>Pore Water Pressure Control Test</i>	46
3.3.2 <i>Undrained Cyclic Loading Test</i>	48
3.3.3 <i>Undrained Seismic Loading Test</i>	50
3.3.4 <i>Undrained Dynamic-loading Test</i>	52
Chapter 4 Application of the Measured Parameters to Landslide Hazard Assessment	55
4.1 Introduction to LS-RAPID Simulation Program	55
4.2 Application for Simulating the Mechanical Process of the 1792 Unzen-Mayuyama Megaslide in Japan	59
4.3 Application for Landslide Hazard Assessment of the Hai Van Station Large-Scale Landslide in Vietnam	63
Chapter 5 Conclusions	71
References	76

List of Figures

Fig. 1.1 Global landslide risk	1
Fig. 1.2 Exposure and fatalities associated with rainfall-triggered landslides by income class	2
Fig. 1.3 Large-scale debris flow disaster in Vargas, Venezuela on 16 December 1999	2
Fig. 1.4 Badakhshan mudslide, Afghanistan on 2 May 2014	4
Fig. 2.1 General View of ICL-2	14
Fig. 2.2 Concept of the ring-shear apparatus (left-modified from Sassa 2013) and photo showing sliding surface after testing (right)	15
Fig. 2.3 Mechanical structure of ICL-2 apparatus (central section of main body)	16
Fig. 2.4 Control System of ICL-2 apparatus	18
Fig. 2.5 Gap system of ICL-2 apparatus	20
Fig. 2.6 Pore water pressure control unit	21
Fig. 2.7 Rubber edge friction test	23
Fig. 2.8 Samples were fully saturated by vacuum tank	24
Fig. 3.1 Area view of earthquake-triggered landslide in Las Colinas, El Salvador, January 13, 2001	27
Fig. 3.2 Location map of the Unzen-Mayuyama landslide and sampling positions	28
Fig. 3.3 Section of Mayuyama landslide and its interpretation	29
Fig. 3.4 Geologic sketch map of Unzen volcano with age data	30
Fig. 3.5 Photos show the sampling locations	31
Fig. 3.6 Grain size distribution of sample Unzen-1 and Unzen-2	32
Fig. 3.7 Dry and saturated unit weight of Unzen-1 sample at different consolidation pressure	32
Fig. 3.8 Location and topography of Hai Van station landslide, Da Nang city, Central region in Vietnam	32
Fig. 3.9 Topography (up) and section (down) of Hai Van station landslide	34
Fig. 3.10 Location map of bore holes and monitoring equipment on Hai Van station slope	35
Fig. 3.11 Monitored rainfall and slope movement at Hai Van station	36

Fig. 3.12 Average monthly precipitation in Da Nang area, Vietnam	37
Fig. 3.13 Geological structure of Hai Van Mountain and location of Hai Van station landslide	37
Fig. 3.14 Lithologic description of the Hai Van station slope collected from the bore holes	38
Fig. 3.15 The sampling location in Hai Van pass area (image from Google Earth) (A) and photos of white granitic sand (Hai Van-2) taken for deep-seated landslide	39
Fig. 3.16 Dry and saturated unit weight of Hai Van-1 sample (left) and Hai Van-2 sample (right) at different consolidation pressure	40
Fig. 3.17 Grain size distribution of sample Hai Van-1 and Hai Van-2	40
Fig. 3.18 Drained speed control test on Unzen-1 sample	41
Fig. 3.19 Drained speed control test on Hai Van-2 sample	42
Fig. 3.20 Stress paths (left side) and time series data (right side) of the undrained monotonic stress control tests on Unzen-1 sample with different normal stress from 300 kPa to 3000 kPa	43
Fig. 3.21 Stress paths of undrained monotonic stress control tests on Unzen-1 sample	45
Fig. 3.22 Undrained monotonic stress control test on Hai Van-2 sample	46
Fig. 3.23 Mechanism of landslide initiation due to pore-water pressure rise (Sassa et al. 2013)	47
Fig. 3.24 Pore-water pressure control test on sample Unzen-1	48
Fig. 3.25 Pore pressure control test on Hai Van-2 sample	48
Fig. 3.26 Undrained cyclic loading test on Unzen-1 sample	49
Fig. 3.27 Mechanism of Landslide initiation due to combined effect of seismic loading and pore-water pressure rise	50
Fig. 3.28 Undrained seismic loading test on Unzen-1 sample taken from the source area	52
Fig. 3.29 Undrained dynamic-loading test on Unzen-2 sample	53
Fig. 4.1 Basic concept of LS-RAPID	55
Fig. 4.2 Projection of seismic forces onto the horizontal plane	57
Fig. 4.3 Concept of shear strength reduction in progress of shear displacement	58
Fig. 4.4 Simulation flow chart for landslide simulation using LS-RAPID	59
Fig. 4.5 Combined graph of shear strength reduction in progress of shear displacement by different ring-shear test	60

Fig. 4.6 Demonstration of simulation result for the 1792 Unzen–Mayuyama landslide. a-e) the whole process of landslide simulation, f) topographic map	62
Fig. 4.7 Comparison between simulation result of LC_RAPID (a) and topographic map (b)	63
Fig. 4.8 Drawing ellipsoidal sliding surface for Hai Van station landslide	64
Fig. 4.9 Cross sections passing through the location of the bore hole	65
Fig. 4.10 Shear resistance and shear displacement of Hai Van-2 sample from undrained tress control tests	67
Fig. 4.11 Demonstration of simulation result for the active Hai Van station landslide	68
Fig. 4.12 Central section of Hai Van station landslide	69

List of Tables

Table 1.1 The most catastrophic landslides over the world	3
Table 2.1 Features of the ring-shear apparatuses from DPRI-3 to ICL-2 (modified from Sassa et al. 2004)	13
Table 3.1 Properties of Hai Van landslide	33
Table 3.2 Climatic data for Da Nang area	36
Table 3.3 Condition and results of undrained monotonic stress control test on Unzen-1 sample	43
Table 4.1 Parameters used for Unzen-Mayuyama landslide simulation in LS_RAPID model	61
Table 4.2 Parameters of Hai Van soil sample used in LS-RAPID simulation	66

Chapter 1 Introduction

Landslides, either alone or in association with the earthquakes, volcanic eruptions, wildfires and rainstorms are major cause of loss in life, injury and property damage to many area in the world in natural disasters (Figure 1.1). They represent a significant threat to lives, property, and development, particularly in developing countries in which population growth, urbanization, and poverty have led to the development of large vulnerable communities on steep slopes in mountainous areas. The susceptibility of slopes to landslides is being increased by development activities and construction which changing slope geometry, strength, loading, vegetation cover, and surface water and groundwater regimes (Anderson 2013).

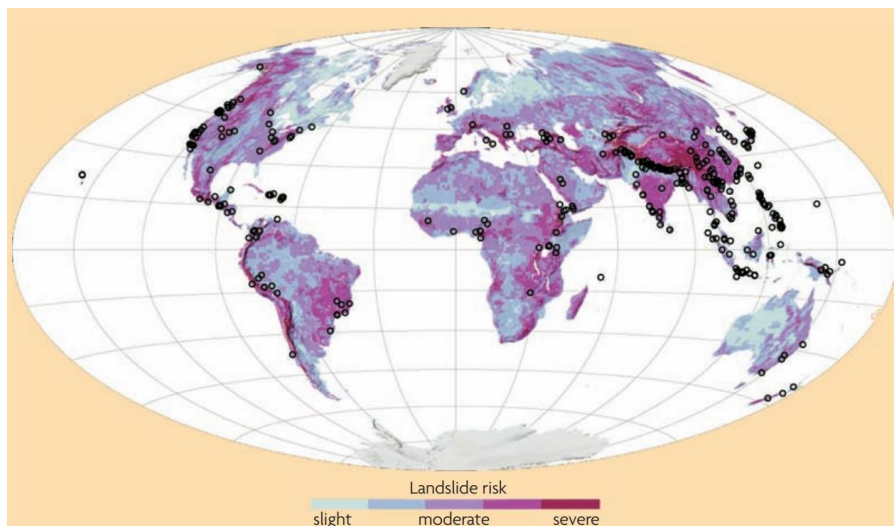


Fig. 1.1 Global landslide risk. Source: National Aeronautics and Space Administration (NASA) Note: Black dots identify the locations of landslides that occurred from 2003 to 2006. Light blue indicates areas of low risk; purple and dark red indicate areas at the highest risk

According to the UNISDR (2009), the majority of fatalities occur in lower-middle- and low-income countries and that is excess of 2 million people are exposed to landslide hazards worldwide (Anderson et al. 2013) (Figure 1.2).

Large, rapid landslides are often triggered by heavy rainfalls, earthquakes or their combined effects in many countries killing many people. Because they often occur rapidly and largely that people have no enough time to evacuate from the landslide

site or take their property out. There are many examples of disastrous landslide in the world (Table 1.1). 1792 Unzen-Mayuyama landslide, which was triggered by an earthquake, resulting in a tremendous tsunami, killed 15,000 people. During the 1920 Haiyuan, China, earthquake, many catastrophic landslides and loess flows occurred over an area of 50,000 km², buried villages and killed about 100,000 people.

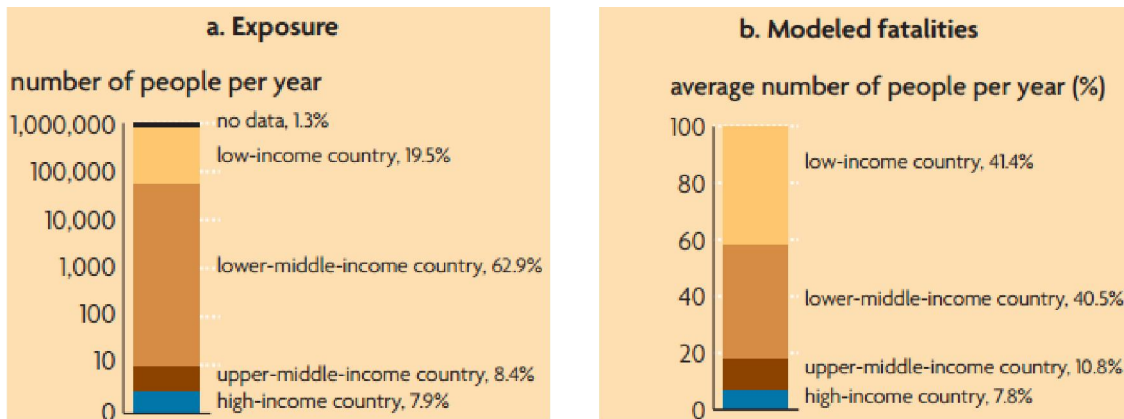


Fig. 1.2 Exposure and fatalities associated with rainfall-triggered landslides by income class. Low income = per capita GNI < \$935; lower middle income = per capita GNI \$936-\$3,705. Upper middle income = per capita GNI \$3,706-\$11,455; High income = per capita GNI > \$11,456. GNI = gross national income (Source: UNISDR 2009)

In the case of the major rain-induced landslide, over the course of 10 days in December 1999, torrential rains inundated the mountainous regions of Venezuela, causing deadly mud slides that devastated the state of Vargas and other areas in the northern part of the country. An estimated 190,000 people were evacuated, but thousands of others, likely 30,000 were killed (Figure 1.3)



Fig. 1.3 Large-scale debris flow disaster in Vargas, Venezuela on 16 December 1999 (Death toll: 30,000)

Table 1.1 The most catastrophic landslides over the world (source: USGS.gov, Wikipedia)

No	Date	Place	Name	Casualties
1	21 May 1792	Shimabara Peninsula of Nagasaki Prefecture, Japan	1792 Unzen earthquake and tsunami	15,000
2	19 May 1919	Kelud, East Java, Indonesia	Kelut Lahars	5110
3	16 Dec. 1920	Haiyuan County, Ningxia, China	1920 Haiyuan earthquake	>100,000
4	25 Aug. 1933	Diexi, Mao County, Sichuan, China	1933 Diexi earthquake	~3100
5	5 July 1938	Kwansai, Hyogo Prefecture, Japan		~1000
6	13 Dec. 1941	Huaraz, Ancash, Peru	Huaraz debris flow	4,000-6,000
7	10 July 1949	Gharm Oblast, Tajikistan	Khait landslide Yasman valley flowslide	800 ~4,000
8	1953	Wakayama Prefecture, Japan	Arida River landslides	1,046
9	1958	Shizuoka Prefecture, Japan	Kanogawa landslides	1,094
10	10 Jan. 1962	Ranrahirca, Peru	1962 Nevado Huascarán debris avalanche	4,000 - 5,000
11	09 Oct. 1963	Longarone, Italy	Vajont landslide	~ 2,000
12	31 May 1970	Yungay, Peru	1970 Nevado Huascarán debris avalanche	>22,000
13	18 Mar. 1971	Chungar, Peru	Chungar avalanche and tsunami	400-600
14	13 Nov. 1985	Armero, Tolima Department, Colombia	Armero tragedy	23,000
15	16 Dec. 1999	Vargas, Venezuela	Vargas tragedy	30,000
16	17 Jan. 2001	El Salvador	Las Coinas landslide	500-1,700
17	17 Feb. 2006	Southern Leyte, Philippines	2006 Southern Leyte mudslide	1144
18	9 Aug. 2009	XiaolinXiaolin (or Hsiao-Lin),Kaohsiung County, Taiwan		500-600
19	8 Aug. 2010	Gansu, China	2010 Gansu mudslide	1,287
20	16 June 2013	Kedarnath, Uttarakhand, India	After Uttarakhand Floods	5,700
21	02 May 2014	Ab Barak, Badakhshan, Afghanistan	2014 Badakhshan mudslides	2700

Recently, on 2 May 2014, a pair of mudslides occurred in Argo District, Badakhshan Province, Afghanistan killed 2,700 and around 300 houses were buried and over 14,000 were affected (Figure 1.4).

The disaster caused by large-scale and mega landslide is very severe, but the geo-mechanical behavior of the initiation and motion of this kind of landslides, particularly at depth in excess of 100m is not yet clearly and completely understood. The mechanical characteristics of soil at such depths differ significantly from those

in the near-surface layer, which is due to the weight of the overburden and stress environment. Therefore, it is very important establish the effective tools for to study the mechanical process of large-scale landslides and assess landslide hazard for disaster preparedness such as land-use planning, early warning, evacuation or relocation of houses (Sassa 2013).



Fig. 1.4 Badakhshan mudslide, Afghanistan on 2 May 2014 (Death toll: 2700)

Source: <http://www.dailymail.co.uk>

1.1 Background for This Study

In order to contribute to geo-disaster reduction along main transport arteries and on residential areas in Vietnam, a project “Development of landslide risk assessment technology along transport arteries in Vietnam” was adopted by the Science and Technology Research Partnership for Sustainable Development (SATREPS) which is under the auspices of the Japan Science and Technology Agency (JST) and the Japan International Cooperation Agency (JICA). The International Consortium on Landslides (ICL), Tohoku Gakuin University, Forestry and Forest Products Research Institute, and Kyoto University are Japanese partner institutions in the project. The Institute of Transport Science and Technology (ITST) has been assigned by the Ministry of Transport of Vietnam (MOT) to collaborate with the International Consortium on Landslides (ICL) in implementation of the Project in 5 years period, from 2011 to 2016. The goal of the Project will be obtained through developing of new landslide risk assessment technology, its application to forecast, monitoring and disaster preparedness of landslides in Vietnam.

As mentioned above, many people were killed by landslides, and in particular in the urbanized areas of developing countries. It is very difficult for developing countries and developed countries as well to create expensive landslide prevention works. The

most effective and economical way to reduce loss of human and property from landslides is landslide-hazard assessment and disaster preparedness including early warning, evacuation and land-use planning (Sassa et al. 2014).

For reducing human loss from landslides, it is needed to assess mechanical behavior of the initiation and motion of landslides including hazard area, speed and depth of sliding mass (Sassa et al. 2014). However, to explain the initiation and motion of landslides is a difficult work because this process occurs with pore-pressure generation, and changes in grain size, grain shape and water content in the shear zone. Studying landslide initial mechanism needs slope-stability analysis and post-failure motion needs to study landslide dynamics. The necessary geotechnical parameters and deformation for each study are different. Studying slope stability needs the peak shear resistance at failure and the mobilized shear deformation while studying landslide mobility after failure needs the steady-state shear resistance during motion.

One of the most important objectives of the project is developing an equipment to determine the geotechnical parameters of the deep-seated landslides which are more than 100m in depth. From 2012, a new high-stress dynamic-loading ring-shear apparatus, ICL-2 have been gradually developed by Professor Sassa K. and other researchers in the International Consortium on Landslides. This apparatus is the latest version of the landslide dynamic-loading ring-shear apparatus series from the model DPRI-1 in 1984 through DPRI-2, 3, 4, 5, 6, and 7, to the model ICL-1 in 2011.

Two case studies were performed to examine the capacity of the new apparatus on the 1792 Unzen-Mayuyama megaslide in Japan triggered by an earthquake and another active large-scale Hai Van station landslide in Vietnam triggered by rainfall at the laboratory of ICL in Kyoto University. Basing on those tests results, measured parameters were applied to the integrated landslide simulation model LS-RAPID for simulating the initiation and motion of the two landslides. Simulation results then can be used to understand the mechanical process of the historical landslide and also assess landslide hazard of the active landslide.

1.2 Research Objectives

The main objective of this research is to develop a new high-stress dynamic-loading ring-shear apparatus for studying deep-seated landslides.

Many terrestrial mass movements are shallow landslides, which move across bounding shear surfaces such as debris flows and mudslides involve masses of

softened material, frequently with a high moisture content, where material is transported downslope at varying speeds depending on external factors controlling shear stress and internal factors affecting shear strength (Petley 1997). In most cases, they can be examined by utilizing established methods in soil mechanics and rock mechanics such as direct shear test and triaxial test. In contrast to shallow landslides is the deep-seated landslides which have also identified in many areas worldwide. But there have been a little examination and poorly understanding of deep seated landslides in their geo-mechanical behavior, particularly at depths in excess of 100m. Petley (1997) also presented in his research that the mechanical characteristics and deformation of sediments at such depths differ significantly from those in the near-surface environment, primarily due to the weight of the overburden and stress environment.

Since 1984, Sassa has attempted to modify and improve the ring-shear apparatus based on the Imperial College and Norwegian Geotechnical Institute concept (Bishop 1971) designed to study the post-peak interval of the shear resistance-displacement curve with emphasis on residual strength. Until now, he and colleagues of the Disaster Prevention Research Institute (DPRI), Kyoto University and the International Consortium on Landslides (ICL) developed a series of nine dynamic-loading ring-shear apparatus from DPRI-1, DPRI-2, DPRI-3, DPRI-4, DPRI-5, DPRI-6, DPRI-7, ICL-1 and ICL-2.

There are three specific objectives as follows:

1. Development of the new high-stress dynamic-loading ring-shear apparatus, ICL-2.
2. Application of the new apparatus to conduct tests on samples taken from two real landslides including one case in Japan and one in Vietnam.
3. Application of the measured parameters obtained from ICL-2 for the mechanical modelling to historical 1792 Unzen-Mayuyama megaslide in Japan and landslide hazard assessment of a recent Hai Van station large-scale landslide in Vietnam.

1.3 Thesis Outline

The research includes five chapters to pursue the research objectives and their contents are outlined below.

Chapter 1 is an introductory chapter that given the background of this study on ring-shear apparatus and large-scale landslides. It also gives the objectives and organization of this dissertation.

Chapter 2 present the development of a new high-stress ring-shear apparatus ICL-2 by bringing out the need for developing new apparatus and showing its design, construction and testing procedures.

Chapter 3 describes the two real study areas of the historical 1792 Unzen-Mayuyama megaslide in Japan and the recent Hai Van station large-scale landslide in Vietnam and presents application of the new high-stress dynamic-loading ring-shear apparatus to study areas. All basic tests and tests for simulating initiation and motion of landslides on samples taken from the two landslides areas are presented in this chapter.

Chapter 4 shows the application of the measured parameters for the mechanical simulation of 1972 Unzen-Mayuyama megaslide and landslide hazard assessment of Hai Van station large-scale landslide.

Chapter 5 is conclusion derived from this study based on the overall research results

Chapter 2 Development of a New High-Stress Dynamic-Loading Ring-Shear Apparatus (ICL-2)

2.1 Introduction to Ring-Shear Apparatus

The high-stress dynamic-loading undrained ring-shear apparatus ICL-2 which developed since 2012 by Professor Sassa and other researchers of the International Consortium on Landslides (ICL) (Sassa 2014, Dang 2014, Lam 2014) will be presented in this study. It is the most improved and advanced types in ring-shear apparatus series so far.

From 1939, Hvorslev in his paper “Torsion shear tests and their place in the determination of the shearing resistance of soil” initially introduced the test configuration for the ring-shear device to investigate the residual strength of the specimen along the sliding surface. His research stated that the data on the decrease of the shearing resistance after failure are required to determine the factor of safety of earth structures in which a localized failure of the soil is allowed or cannot be prevented.

Then this concept was widely utilized and developed by Bishop et al. (1971), Bromhead (1979), Sassa (1984), Tika et al. (1989), Gibo (1994), and Garga and Sendano (2002) because of its advantage in unlimited deformation of the specimen (introduced by Sassa, 2004). There are two main styles of ring-shear device improved from its original design. Bromhead type in which shear zone is at the top of the specimen – modified by Savage and Sayed (1984), Stark and Eid (1993), Stark and Poeppel (1994), Stark and Contreras (1996), Garga and Sedano (2002), Sedano et al. (2007), Meehan et al. (2007, 2008), Merchan et al. (2011), and Bishop type in which shear zone is at the mid-height modified by Sassa (1984), Hungr and Morgenstern (1984), Tika (1989), Tika et al. (1996) as introduced by Ostric (2013).

Sassa (2004) indicated the main advantage of the Bishop type compared to other models of ring-shear apparatus is that the Bishop type could measure the friction between the soil sample and the sidewalls of the upper shear box. It is particularly

significant in the development of the ring-shear apparatus because it guarantees an accurate determination of the total normal stress acting on the soil specimen during testing. In Bishop device, sample box includes two parts (upper half and lower half) and shear zone is at the middle of the shear box, while in the Bromhead type shear zone is at the top of the specimen because this device does not have two sample boxes. These apparatus have one sample box loaded and sheared by the upper loading platen and shearing takes place between the upper loading platen, bottom of the shear box and soil sample. So the mobilized shear resistance may differ from that mobilized during shearing within the specimen, especially for sandy materials (Sassa 2004). All those devices could not prevent water leakage through the rotating gap, and they were known as drained ring-shear apparatus.

Thirty one years ago, Sassa and his colleagues of the Disaster Prevention Research Institute (DPRI), Kyoto University started to develop a new series of dynamic-loading ring-shear apparatus in order to completely simulate the landslide mechanism from the initiation to the motion. Base on the same principle as the ring-shear device of Bishop (1971) seven apparatus of DPRI series were created and improved from version DPRI-1 (1984) to DPRI-7 (2004).

This DPRI series has achieved great success in quantitatively simulating the entire process of failure of a soil sample, from initial static or dynamic loading, through shear failure, pore-pressure changes and possible liquefaction, to large-displacement, steady-state shear movement (Sassa 2004). The first version DPRI-1 is the original high-speed ring-shear apparatus used a conventional shear-speed control motor and it is also a drained testing device. To reproduce rainfall-induced landslide and earthquake-induced landslides, it is necessary to maintain an undrained condition in the specimen because of pore-water pressure is very important in the mechanism of the long runout landslides. To keep undrained condition and measure pore-water pressure during testing are very difficult. The later five apparatuses of this series from DPRI-3 (created in 1992), DPRI-4 (1996), DPRI-5 (1997), DPRI-6 (1997) and DPRI-7 (2004) have capability of shear stress-controlled tests and enables simulation of both monotonic and dynamic loading (real seismic waves or sine wave form) under undrained conditions (Ostic 2013). DPRI-3 uses a torque-control motor and a servo-control system that utilized the feed-back signal from a load cell (Sassa 1994, 1996). After that, a series of dynamic-loading ring-shear apparatus from DPRI-4, DPRI-5, DPRI-6 and DPRI-7 were established with different advantages in characteristics as followings (Sassa 2004):

- Shearing is given by the stress-control condition (more precisely by torque-control) and the speed-control test also can be conducted with the maximum speed from 33 cm/s (DPRI-3) to 300 cm/s (DPRI-7) to measure the residual friction angle of the specimen.
- These apparatus can perform experiments under undrained condition during rapid shearing by pressing rubber edges onto the bottom of the upper part of shear box at a necessary contact pressure using a servo-oil piston and gap sensor with a precision of 1/1000 mm. And pore-water pressure can be monitored by a pressure gauge connected to the filtered gutter along the circumference of the inner wall of the outer ring of the upper shear box. The maximum undrained capacities of DPRI series is 650 kPa.
- They can simulate earthquake loading (with seismic or cyclic loading) and other processes involving rapid stress (frequency up to 5Hz) changes by rapid loading and high-speed data acquisition (from 12 readings/s of DPRI-3 to 1000 reading/s of DPRI-7).
- Cyclic shear-displacement control tests, torque-control tests, and shear-speed control tests can also be performed by DPRI-4 and DPRI-7.

As introduced by Ostric (2012, 2013), Sassa (2012), Tien (2015), and Loi (2015) these undrained ring-shear apparatuses are complex and expensive then Sassa tempted to design a compact and inexpensive ring-shear apparatus. In 2011, after retirement from Kyoto University, he created the undrained portable ring-shear apparatus – ICL-1 within the framework of the cooperation project of SATREPS (Science and Technology Research Partnership for Sustainable Development) and JICA/JST (Japan International Cooperation Agency/Japan Science and Technology Agency) project “Risk identification and land-use planning for disaster mitigation of landslides and floods in Croatia”. In the development of this new apparatus, consideration had to be given to simplicity in the construction and operation, specimen preparation and time required for testing (Ostric 2013). Although a portable devise and smaller in dimensions compared to previous versions, ICL-1 can load normal stress and maintain undrained condition of pore-water pressure up to 1 MPa (Ostric 2012, 2013, Sassa 2012).

From 2012, Sassa and other researchers of the International Consortium on Landslides (ICL) were developed a new high-stress dynamic-loading ring-shear

apparatus, ICL-2. The purposes and detailed configuration of this apparatus will be presented in the next parts of this chapter.

2.2 Purposes to Develop the New High-Stress Dynamic-Loading Ring-Shear Apparatus

There are many historical and recent megaslides and large-scale landslides (shown in Table 1.1). They may trigger Tsunami, landslide dams causing great debris flows or floods as well as causing direct damages. Some cases of megaslides have been studied in detail such as the 2006 Leyte landslide in the Philippines (Catane et al. 2007, Araiba et al. 2008, Sassa et al. 2010), the 2008 Aratozawa landslide in Japan (Konagai et al. 2008, Miyagi et al. 2011). The depths of these megaslides are from 120 m to 200m (Leyte landslide), or over 150 m (Aratozawa landslide). So far dynamics of such megaslides has not been well-studied. It is needed to develop a reliable hazard assessment technology for those landslides kind.

As mentioned in previous part, DPRI series and ICL-1 ring-shear apparatus were great success in reproducing sliding-surface formation and measuring post-failure motion in rain- and earthquake-induced landslides. In spite of getting such many successes but these devices could not apply to large-scale landslides and megaslides which have the depth of over 100 m in depth, greater than 10 million m³ in volume causing a great effect either on land, coastal or under water.

The undrained ring-shear apparatus (ICL-1) was improved to maintain the undrained state up to 1000 kPa in 2011. Based on this result in 2011, the group has developed a new high-stress ring-shear apparatus (ICL-2) to simulate the initiation and motion of megaslides in 2012-2013. The successful undrained capacity of ICL-2 is 3 MPa, namely 100-200m deep landslides can be simulated effectively. Table 2.1 shows the advanced features of the ICL-2 compared to previous models of ring-shear device. This apparatus was applied to interpret the initiation and motion of the 1792 Unzen Mayuyama megaslide (volume is 3.4×10^8 m³, Maximum depth is 400 m) triggered by an earthquake. This landslide killed around 15,000 people by the landslide and the Tsunami wave induced by the landslide. The Unzen Restoration Office of the Ministry of Land, Infrastructure and Transport of Japan (MLIT) integrated various papers and reports and published two leaflets: one in English in 2002 and the other extended version in Japanese in 2003. Samples were taken from the source area for initiation and the moving area for motion. The hazard area was estimated by the undrained ring-shear tests and the integrated computer simulation model (LS-RAPID,

Sassa et al. 2010) using parameters obtained from the tests data. The estimated hazard area has reasonably agreed with the landslide moving area reported by MLIT. This research result was contributed to Landslides in 2014. This research was included in the plenary lecture of WLF3, title as “Progress in Landslide Dynamics” as the most updated progress of landslide dynamics.

Table 2.1 Features of the ring-shear apparatuses from DPRI-3 to ICL-2 (modified from Sassa et al. 2004)

Version	(1992) DPRI-3	(1996) DPRI-4	(1997) DPRI-5	(1997) DPRI-6	(2004) DPRI- 7	(2011) ICL-1	(2012) ICL-2
Inner diameter (cm)	21.0	21.0	12	25.0	27.0	10.0	10
Outer diameter (cm)	31.0	29.0	18	35.0	35.0	14.0	14.2
Max. height of sample (cm)	9.0	9.5	11.5	15.0	11.5	5.2	5.2
Shear area (cm ²)	408.41	314.16	141.37	471.24	389.56	75.36	79.79
Max. shear speed (cm/s)	30.0	18.0	10.0	224.0	300.0	5.4	50
Max. normal stress (kPa)	500	3,000	2,000	3,000	500	1000	3000
Max. pore-water pressure (kPa)	-	490	400-600	400-600	400- 600	1000	3000

2.3 Design and construction of the new ring-shear apparatus ICL-2

2.3.1 Design

Figure 2.1 presents the general view of the new high-stress dynamic-loading ring-shear apparatus (ICL-2) which has been developed to simulate megaslides up to 3 MPa in normal stress. As a part of the project IPL-175 on “Development of landslide risk assessment technology along transport arteries in Vietnam” ICL-2 will be donated to Vietnam in 2015. Therefore, the other aim of ICL-2 is for practical use, less expensive to manufacture, lower-cost maintenance and the capability to be maintained in a developing country as Vietnam. Together with the purpose of studying deep-seated landslides, they were the major considerations in the design for this apparatus. The computer system (1) including Ring-shear apparatus software can control all functions of the apparatus such as normal stress control, shear stress control, shear speed control, shear displacement control, pore-water pressure control. This computer also displays signals from sensors for shear stress/torques, normal stress/vertical load, pore pressure, effective pressure, mobilized friction angle, shear displacement and vertical displacement as time-series data plots and as stress-path

data plots. Servo-control systems drive the shear motor and gap control motor, oil servo-valves for the normal-stress control and pore-pressure control. The servo-control systems and amplifiers for data monitoring are included in the amplifier box - Main Control Unit (2). Part (3) is the main apparatus, including the shear box, loading piston, and shear- and gap-control motors. Other components are the power supply unit (4), the pore-water pressure loading unit (5), and the de-air water and vacuum system for sample saturation (6) (Sassa et al. 2014).

The new ring-shear apparatus was designed and developed in 2012-2013 in order to simulate the initiation and motion of megaslides of more than 100m in depth (Sassa 2014). And the successful undrained capacity of ICL-2 is 3 MPa.

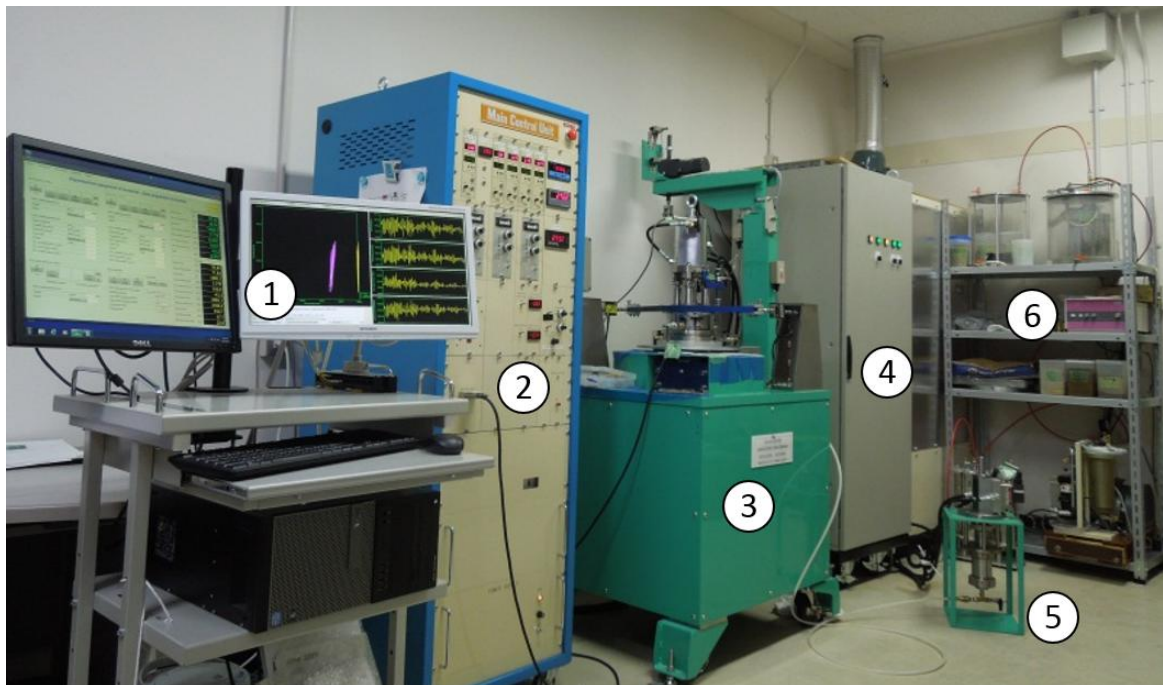


Fig. 2.1 General View of ICL-2 (From left to right: 1) Computer system , 2) Main control unit for control and monitoring, 3) Main apparatus, 4) Power supply box, 5) Pore pressure unit, and 6) de-air water and vacuum system)

2.3.2 Construction

Figure 2.2 illustrates concept of the ring-shear apparatus. Samples (disturbed) are taken from the layer where a sliding surface can be formed in the future. Then the sample is set in the ring shear box including static upper half and a rotary lower half. All stresses acting on the potential sliding surface can be reproduced in the shear box such as normal and shear stresses due to gravity and seismic stress due to seismic shaking as well as generated pore-water pressures. When shear stress

(static, seismic) is high enough to trigger sample failure, the rotary lower half of the shear box will start to turn. The annular ring-shaped sample will be sheared on a plane of relative rotary motion.

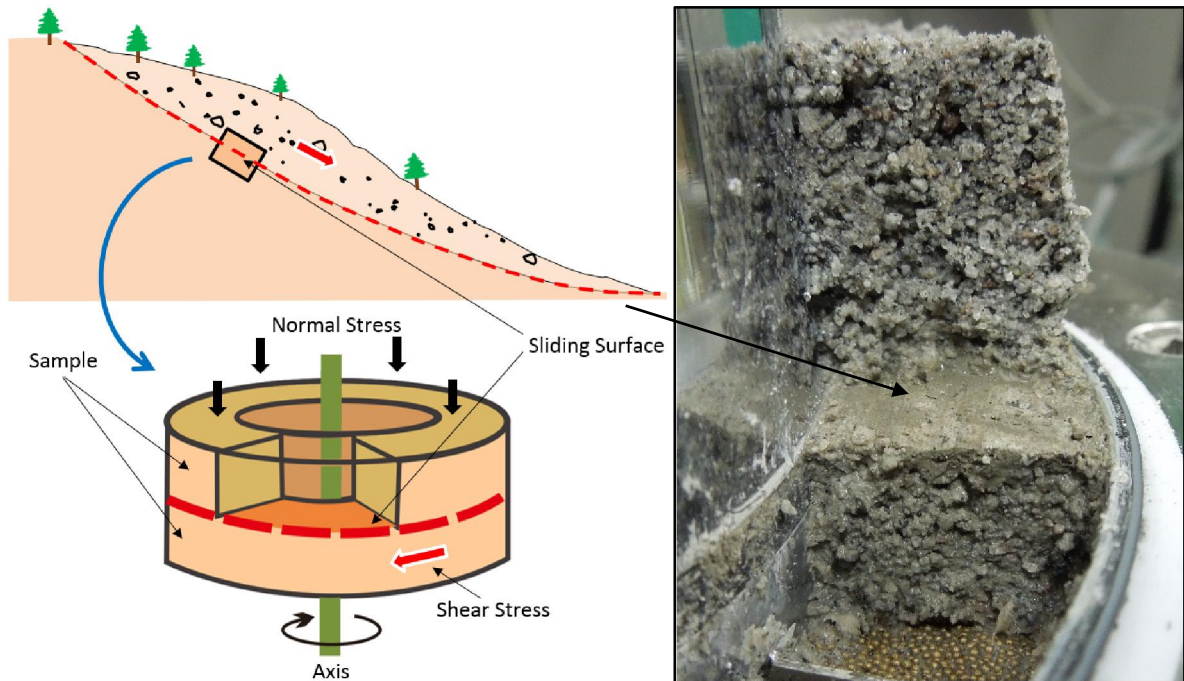


Fig. 2.2 Concept of the ring-shear apparatus (left-modified from Sassa 2013) and photo showing sliding surface after testing (right)

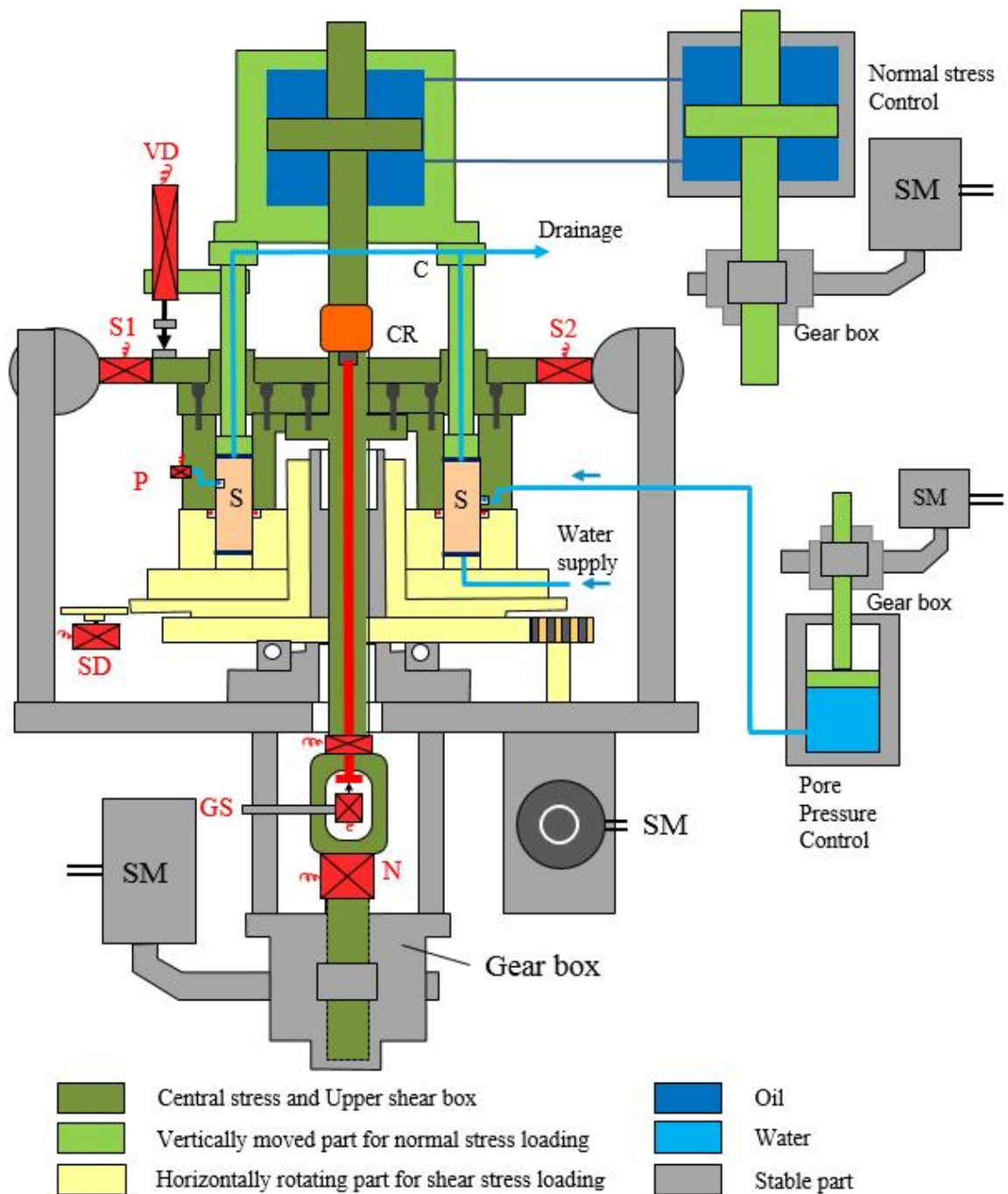


Fig. 2.3 Mechanical structure of ICL-2 apparatus (central section of main body; S- Sample; CR- Connection Ring; C- Connection; N- Load cell for Normal Stress; S1, S2- Load cell for shear resistance; GS- Gap sensor; FC- Feedback signal; CS- Control signal; PC- Computer; SG- Signal Generator; SM- Servo-motor; OP- Oil Piston; SA- Servo-amplifier)

The mechanical structure of the ICL-2 apparatus is shown in Figure 2.3. The parts of the apparatus are coded with different colors in the Figure as follows: gray (lower part), stable part; yellow (lower shear box and rotating table), rotates horizontally for shearing; dark green (upper shear box and loading cap), rotates horizontally and

moves vertically. This part is horizontally restrained by a pair of load cells (S1 and S2) which monitor shear stress and vertically restrained by the load cell which monitors normal stress (N). Each load cell is very slightly extended or compressed as required to measure forces. Light green (central axis to connect to the loading piston), can move vertically to adjust the gap between the upper and lower shear boxes. The light green colored part is fixed to the dark green part after the sample has been set until the conclusion of testing. Light gray (top, loading piston), the piston rod (light green) connects to the stable part (gray) through the load cell for normal stress (N). When oil pressure is supplied to the lower chamber (blue) of the loading piston, a tensile stress acts through the central axis (light green), to pull the housing of the loading piston (light gray) down on the sample, thus loading the normal stress.

The greatest difference between ICL-2 device and (DPRI-3 and DPRI-6) is the system for loading normal stress. Model DPRI has long loading frame consisting of two long vertical pillars and one horizontal beam. The frame is extended and compressed in pillars and deformed in beam during changes in loaded stress due to cyclic and seismic loading and sudden stress changes when grains or soil structures fail due to high normal or shear stress. In ICL series, the loading frame was removed. The basic concept returns to the DPRI-1 loading system without the loading frame. They have an air tube pressed to the sample and the loading cap which was restrained by the central axis. The loading normal stress is provided by a tensile stress along the central axis. Models ICL-1 and ICL-2 achieve this via a loading piston in place of an air tube. Oil pressure within the loading piston is controlled by servo valve (SV) using the feedback signal from the load cell (N) measuring the normal stress. When a testing programme has been selected and a control signal given for monotonic stress, cyclic or seismic stress loading, and oil is pumped into the loading piston, loading the normal stress by pulling on the central axis. The normal stress acting on the sliding surface (upward) is retained by the central axis (downward), and this load is measured by the vertical load cell (N). In this system, the role of the two long pillars used in models DPRI-5, 6, and 7 was replaced by one short central axis column and the role of the long horizontal beam is replaced by the loading piston. Deformation of this system is much smaller than in the frame loading system. This structure enables stable servo-stress control. The minimum deformation during cyclic and seismic loading and possible sudden stress change due to grain crushing on sands has enabled maintenance of an undrained state up to 3 MPa during tests.

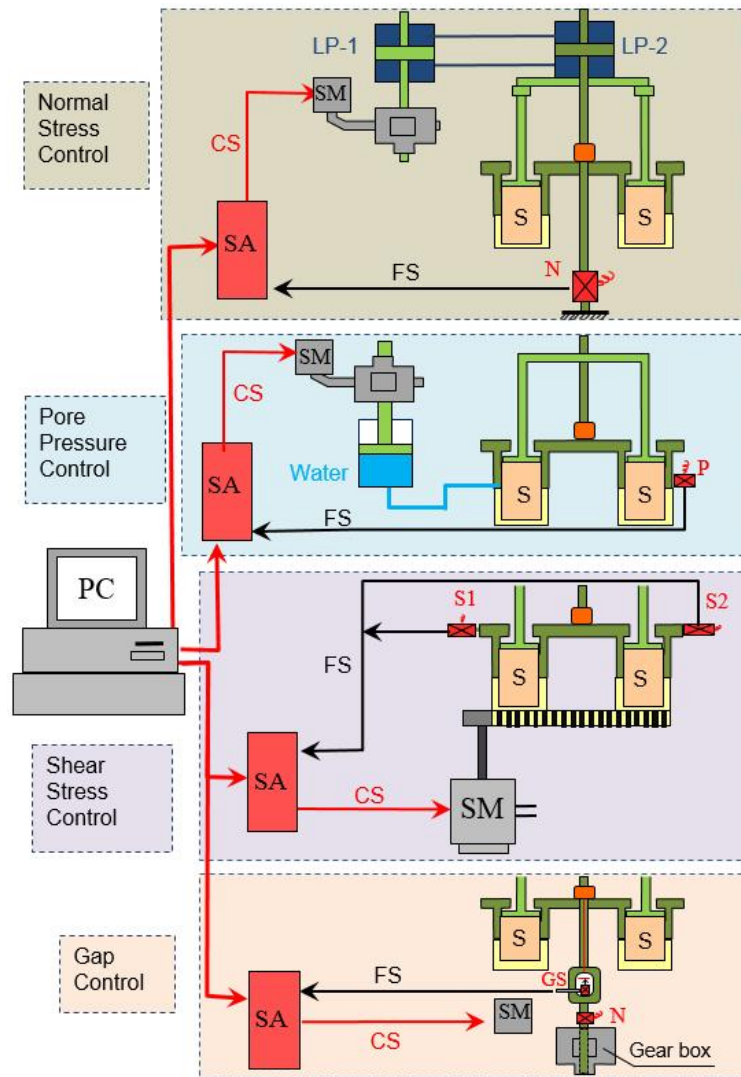


Fig. 2.4 Control System of ICL-2 apparatus

PC- Computer system; S- Sample; N- Load cell for Normal Stress; S1, S2- Load cell for shear resistance; GS- Gap sensor; FS- Feedback signal; CS- Control signal; PC- Computer; SM- Servo-motor; LP- Loading Piston; SA- Servo-amplifier

Normal-stress control system

Normal stress (static and seismic) is produced by two loading piston system (LP-1 and LP-2) controlled by a servo-motor (SM; gray color) (Figure 2.4). Then normal stress to the soil sample is transferred through three upright loading rods connected to the loading piston (LP). When a control signal (red line) is sent from the computer to increase normal stress, the servo-motor rotates and pulls the loading piston 1 (LP-1, dark blue) down, resulting in increment of the lower part of the LP-2 (LP-1 and LP-2 are designed with the same volume). Therefore normal stress to the sample will be increased. The normal stress acting on the sliding surface is measured by the vertical load cell for normal stress (N: red color). This measured value is used as the feedback signal (FS, black line). The normal stress control servo-amplifier (SA, red color) automatically controls the value of loaded normal stress to the predetermined value by sending a control signal to the servo-control motor (SM).

Gap control system

Gap control system (including gear box, servo-control motor and gap sensor, GS) (the lowest part of Figure 2.4). During the test, the gap contact force pressing the upper part of shear box to the rubber edge of the lower shear box is kept constant by keeping the gap constant. The value is maintained constant automatically by the gap control servo-amplifier (SA: red). SA sends a control signal to the servo-control motor (SM) for gap control and receiving a feedback signal from the gap sensor (GS) then, it controls the contact force to the given value. The precision of gap value in ICL-2 apparatus is 1/1000 mm. The gap between the upper shear box and the lower shear box must be precisely controlled, even when the samples dilate during shearing or cyclic loading. The contact pressure of the rubber edge must be constant and greater than the pore pressure inside the shear box, to calculate the normal stress and shear stress applied to the sample. When the sample dilates and tends to increase the gap, the servo-motor immediately responds to maintain pressure to keep the gap constant.

ICL-2 and DPRI series have a difference in the rubber edge which has a critical role for sealing. Rubber edges of all DPRI series apparatus were glued to the shear box. A constant thickness of glue is impossible to achieve and the height of the upper surfaces of the rubber edges of the inner ring and the outer ring must be equal to maintain an undrained condition. Hence after a new rubber edge had been glued to the shear box, it had to be machined by a skilled technician. In the ICL series, the rubber edges are fixed without glue. This shape (grey color in Figure 2.5) of rubber edge is processed from a constant-thickness rubber plate. A number of rubber edges of this shape can be commercially purchased in reasonable cost. The rubber edge is simply placed on the lower ring and pressed by a Teflon ring holder, and this holder is pressed in turn by a steel ring holder fixed by a set of screws. No glue or specialist machining are needed. The Teflon ring holder was designed for the high stress of ICL-2 (3 MPa). Because the rubber edge used in DPRI-6 was deformed outwards due to a high lateral stress, it could not maintain undrained state. To prevent such deformation in the ICL series, a Teflon ring horizontally supports the rubber edge. The height of the rubber edge is gradually reduced by wear during experiments. If the steel ring holder were to touch the upper ring, it would mobilize a large shear resistance and damage the upper ring. The Teflon ring is softer than steel and has low friction, and so it causes no damage. However, when wear allows the Teflon ring to touch the upper ring, it can be noticed that it is time to change rubber edge.

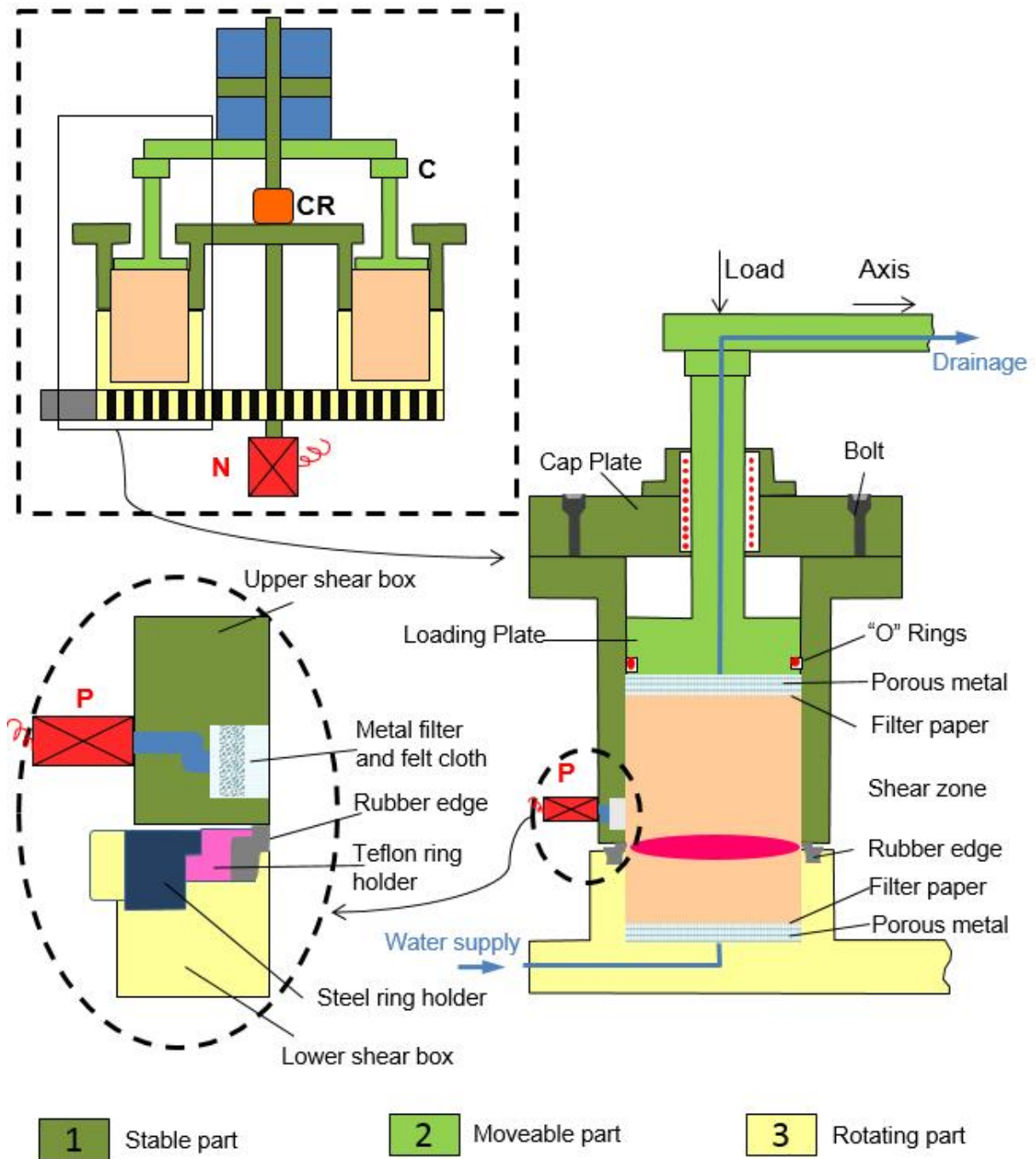


Fig. 2.5 Gap system of ICL-2 apparatus

Shear-stress control system

As shown in Figure 2.4, shear stress is generated by a servo-control shear motor (SM, gray color in the third part from the top). An electric signal of shear stress control or shear speed control is supplied by the computer through the servo amplifier (SA) to the servo motor. The servo-control shear motor rotates the lower shear box (yellow

part) through a gear, while the upper shear box (dark green part) is fixed to torque-measuring sensors S1 and S2 rigidly mounted on two pedestal pillars. The shear stress mobilized on the sliding surface is measured by S1 +S2, because the torque caused by the shear stress on the shear surface and the rubber edge shear resistance is balanced by the torque applied by the two shear load cells. The servo-control motor applies the planned shear load or shear speed by instruction from the control signal given from the computer through the servo-amplifier. The third illustration in Figure 2.4 presents the control signal (red line) to the servo-motor and the feedback signal (black line) from the shear load cell in the shear–stress control test. The shear control signal is generated in the computer. In the seismic loading tests, a pre-selected seismic wave is saved in the computer in advance. Then, the amplitudes of the shear stresses to apply and their times of application are specified in a computer file. This supplies the control signal to the servo-amplifier to apply the shear load (Sassa 2014).

Pore-water pressure control system

Figure 2.6 shows the over view of the pore-water pressure control unit to simulate rainfall-induced landslides. Pore pressure is increased following a preselected programme. The control signal is sent from the computer to the servo-motor (SM: gray color in the second part of Figure 2.4). Water pressure is generated in the piston and supplied to the sample as pore pressure. The feedback signal is returned from the pore-pressure sensor (P: red color), thus automatically controlling the pore pressure.

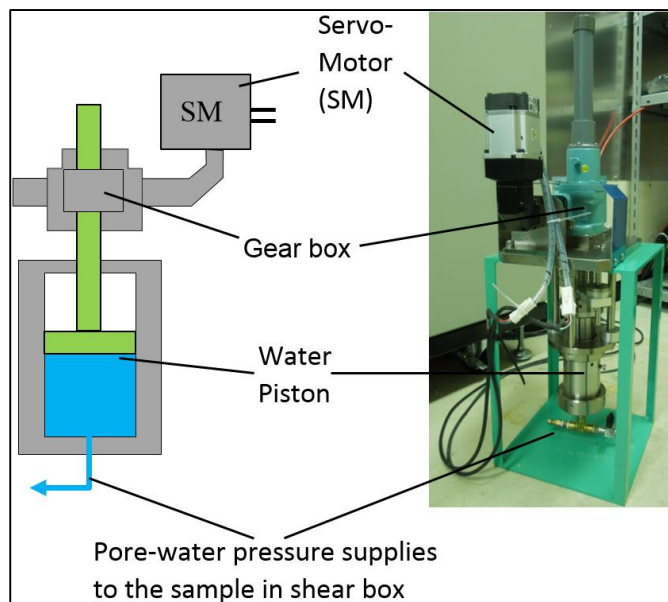


Fig. 2.6 Pore water pressure control unit

2.4 Testing Procedures

In this research, all the tests of the new apparatus were carried out following the procedures listed below:

2.4.1 Rubber edge friction checking

The shear stress mobilized on the sliding surface is equal to the measured value of the shear load cell (S1+ S2) minus the rubber-edge friction. When a normal stress is loaded on the sample in the shear box, a lateral pressure acts on the rubber edge, as shown in the Figures 2.6. In order to reduce friction and prevent leakage, rubber edges are sprayed with Teflon spray and coated with silicon grease (Ostric 2013).

The rubber edge is compressed by the lateral pressure, but due to an arch action of the rigid stainless steel shear box, less pressure will act on the soft rubber edge. The lateral pressure ratio (k is the ratio of lateral pressure to vertical pressure) is approximately expressed by the Jaky's equation (Sassa 1988, Sassa 2014) as $k=1-\sin\phi$. When $\phi=30^\circ$, $k=0.5$. We initially believed that the lateral pressure would be approximately 1/2 to 1/3 of the normal stress. We therefore chose to fill the shear box with water and consecutively loaded normal stresses of 1.0 and 1.5 MPa and sheared water in a speed-controlled test. Figure 2.7 presents the measured shear resistance of the rubber edge at 1.0, and 1.5 MPa. Both tests indicated a rubber edge friction of 30-35 kPa; however, the value varied with shear displacement. The most important value is the steady-state resistance after a large shear displacement. It was found to be 35 kPa. The precision of the shear load cell and normal stress load cell are 0.01–0.03 % of the full scale. The precision of the pore-pressure sensors is 0.14–0.15 %. The precision of the rubber-edge frictional resistance (± 2.5) will be 0.08 % of the full scale (3 MPa) of the load cell for normal and shear stresses. When conducting tests at lower normal stresses, the load cells can be replaced by those of lower capacities.

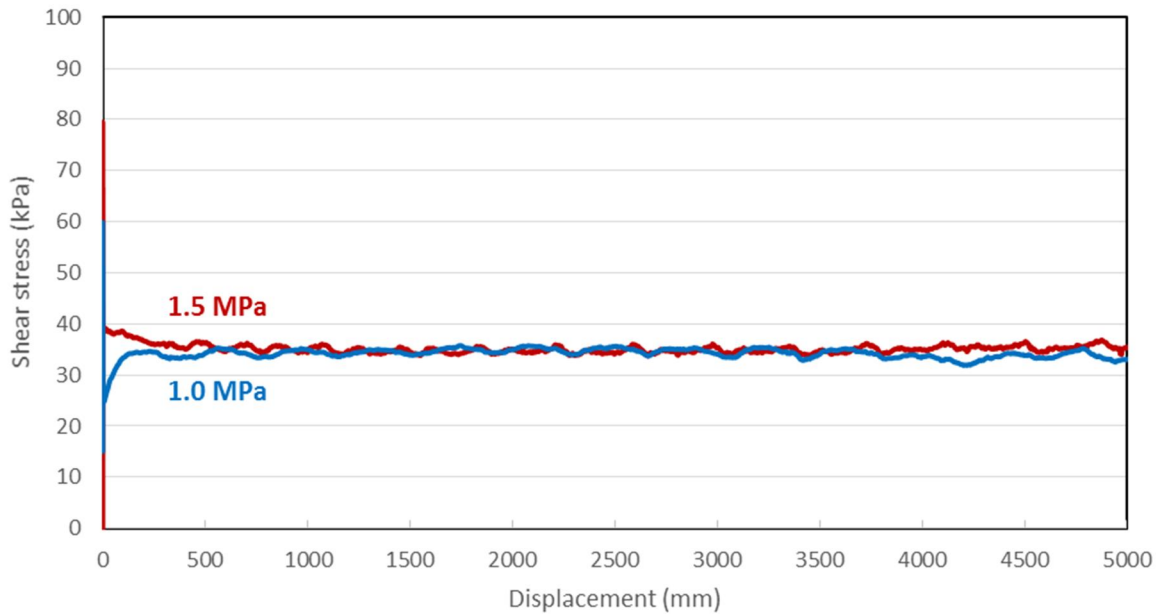


Fig. 2.7 Rubber edge friction test

2.4.2 Sample saturation

The samples should be carefully prepared in order to obtain full saturation. App 3 days prior to testing samples should be prepared, process of preparation takes 3 days (2 nights in vacuum in water tank) (Figure 2.8):

- Samples after sieving by the sieve of 2 mm in diameter are slowly poured into the bottles with de-aired water (300 ml deaired water and 500 ml of sample). Then put the bottle with sample and de-aired water in the vacuum and leave them over night.
- Next day, use vibration in combination with vacuum in around 1 hour to make the bubbles of air come out. In order to settle, leave in vacuum during night and no further vibrations.
- After 1 night the sample is settled. The water is on the top while the sample is down. Take out from the water tank (releasing the vacuum slowly) and pour out the water from the top. The sample is ready for test.



Fig. 2.8 Samples were fully saturated by vacuum tank

2.4.3 Saturation checking

To check the saturation degree of samples, B_D parameter (proposed by Sassa 1988) are used in this ring-shear apparatus. The sample is firstly consolidated under normal stress of 30 kPa in drained condition to make contact between sample and porous metal of the loading plate. Then change to the undrained condition and increase the normal stress with $\Delta\sigma = 50$ kPa, and measure the increment of excess pore pressure (Δu). Therefore, the degree of saturation can be check by the ratio B_D of excess pore pressure increment and normal stress increment ($\Delta u / \Delta\sigma$). Specimens with B_D greater than 0.95 could be considered as a full saturation. In drained tests and pore water control tests, it is not necessary to check B_D value.

2.4.4 Sample consolidation

After saturation checking, in order to create the same initial stress condition acting on the samples like in real condition, we had to apply on the sample in drained condition under the pre-decided normal stresses and shear stresses. In this research, the tests were carried out under normal stresses from 300 kPa to 3 MPa. Because the sample used in this apparatus is sand so both normal and shear stress are applied by computer in the rate of 1 kPa/s or 2 kPa/s.

2.4.5 Shearing

Soil sample can be sheared in drained, undrained or partially drained condition depend on the purpose of the test (Ostria 2013).

A drained test is the best way to measure the friction angle of a sample and also to check the apparatus without any effect of pore-water pressure. After fully saturation, sample are consolidated to pre-decided normal stress which is same as in field condition and then shear at a speed of 0.2 cm/s in the drained condition. When the shear surface had reached peak shear resistance, the drained normal stress was reduced to zero at a rate of 5 kPa/s to obtain the drained stress path and friction angle of the sample (Sassa et al. 2014).

Undrained stress control tests are used for simulating landslide because it can provide appropriate shear stresses under the triggering factors (earthquake shaking, ground-water fluctuation, or change of slope profiles due to toe erosion or filling) in the moving landslide mass (Ostria 2013, Sassa et al. 2014). First, normal stress was loaded in drained condition to the planned normal stress. Then change the shear box to undrained condition, and increase shear stress gradually at a rate of 1-5 kPa/s. When the effective stress path reached the failure line, it began to decrease due to pore-water pressure generation according to the mechanism of “Sliding-surface liquefaction” (proposed by Sassa in 1996). Then effective stress path moved along the failure line until the steady-state shear resistance was reached.

Chapter 3 Application of the New High-Stress Dynamic-Loading Ring-Shear Apparatus to Large-Scale Landslides

3.1 Introduction of Studied Landslides

Two study sites were selected for applying the new ring-shear apparatus. The first one is a historical megaslides in Shimabara Peninsula, Japan and the second one is an active landslide in Da Nang city, Vietnam.

3.1.1 *The Historical 1792 Unzen-Mayuyama Megalide in Japan*

Earthquake-induced landslides are among the most destructive phenomena related to failure of slopes during earthquakes (Trandafir 2006). Globally, many locations have over steepened and highly weathered hillsides, where large landslides could cause significant harm to local communities-many of which are already vulnerable in terms of housing structures and poverty. The 2001 earthquakes in El Salvador are a notable example in this regard, causing over 600 landslides and resulting in many hundreds of fatalities, with 585 deaths in the community of Las Colinas alone (Figure 3.1) (Anderson 2013).



Fig. 3.1 Area view of earthquake-triggered landslide in Las Colinas, El Salvador, January 13, 2001 (Source: wikipedia.org)

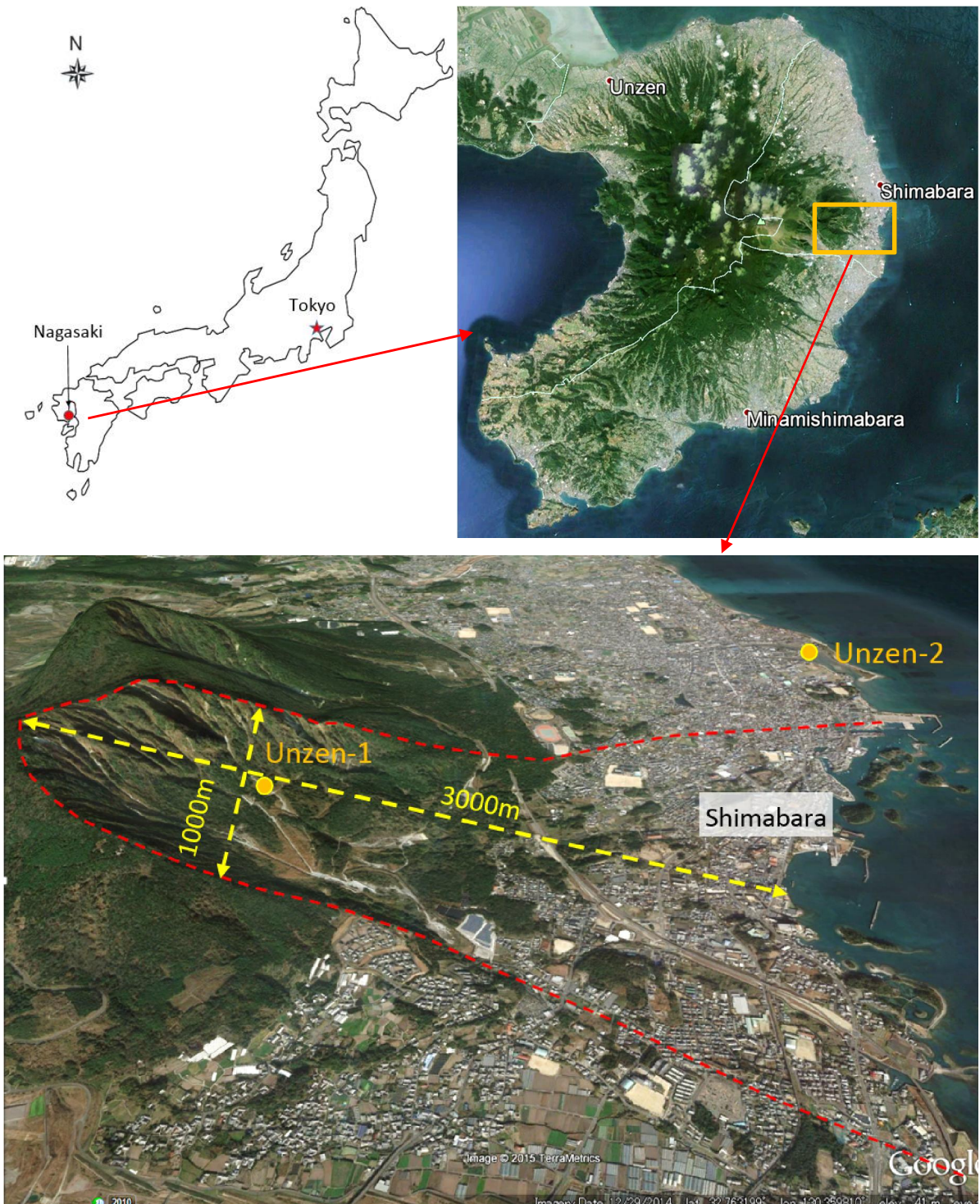


Fig. 3.2 Location map of the Unzen-Mayuyama landslide and sampling positions (from Google Earth)

Unzen is the site of Japan's most destructive volcanic disaster on record. Mt. Mayuyama, one of the Unzen Volcanoes, is situated in the eastern part of the Shimabara Peninsula, and in the west of Shimabara city. It is a lava dome composed of dacite. Following a period of eruptive activity on May 21, 1792 a megaslide was triggered by an earthquake in the Mayuyama lava dome with a volume of about $3.4 \times 10^8 \text{ m}^3$ and the maximum depth of 400m

(Sassa 2014) (Figure 3.3). The debris of the lava dome swept through Shimabara city and slammed into the Shimabara Bay, caused a massive tsunami over 10m high that wreaked havoc the Shimabara city and Higo (current Kumamoto Prefecture) on the opposite shore. This catastrophe resulted in 15,000 deaths by landslide and its resulting tsunami making it the most serious volcanic disaster in Japan (Unzen Restoration Office of the Ministry of Land, Infrastructure and Transport of Japan 2002; 2003).

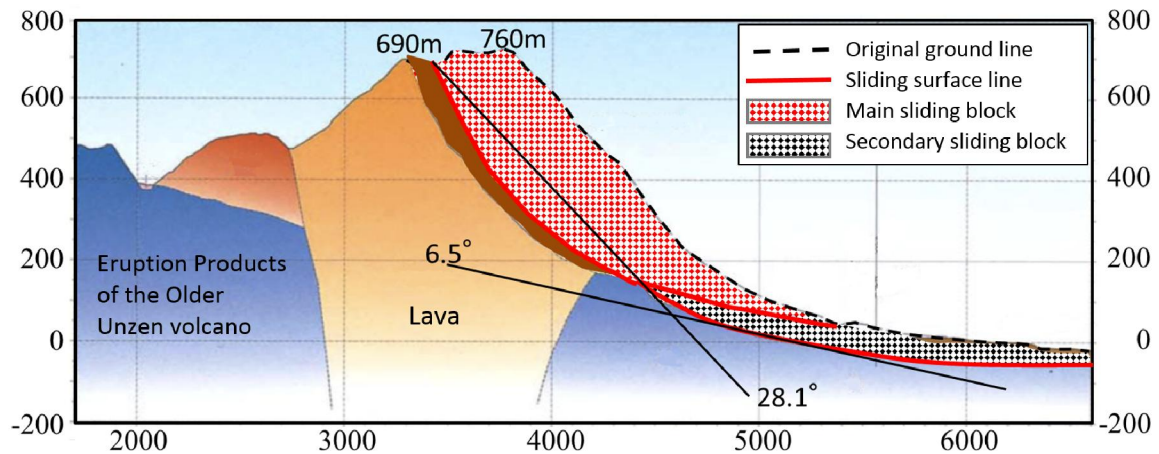


Fig. 3.3 Section of Mayuyama landslide and its interpretation

Figure 3.3 presents the section of the Unzen-Mayuyama landslide before and after the event modified from the Unzen Restoration Office of the Ministry of Land, Infrastructure and Transport of Japan (2002). The bedrock surface in the area is drawn based on the current topography and the geologic sketch map of Unzen volcano (Figure 3.4) (Shimizu et al. 2007). According to the estimated ground surface before landslide and the bedrock surface in the source area of the upper slope and the bedrock in the lower area, we suggest that there were two landslide blocks occurred in this area. Firstly, a main sliding block (block with red dots) on the upper slope moved toward the lower part and applied undrained loading on the soil mass of the lower slope (black dots). This process caused a secondary motion of the lower slope. The average slope angles of the sliding surfaces in the upper slope and lower slope are 28.1° and 6.5° respectively (Figure 3.3) (Sassa et al. 2014).

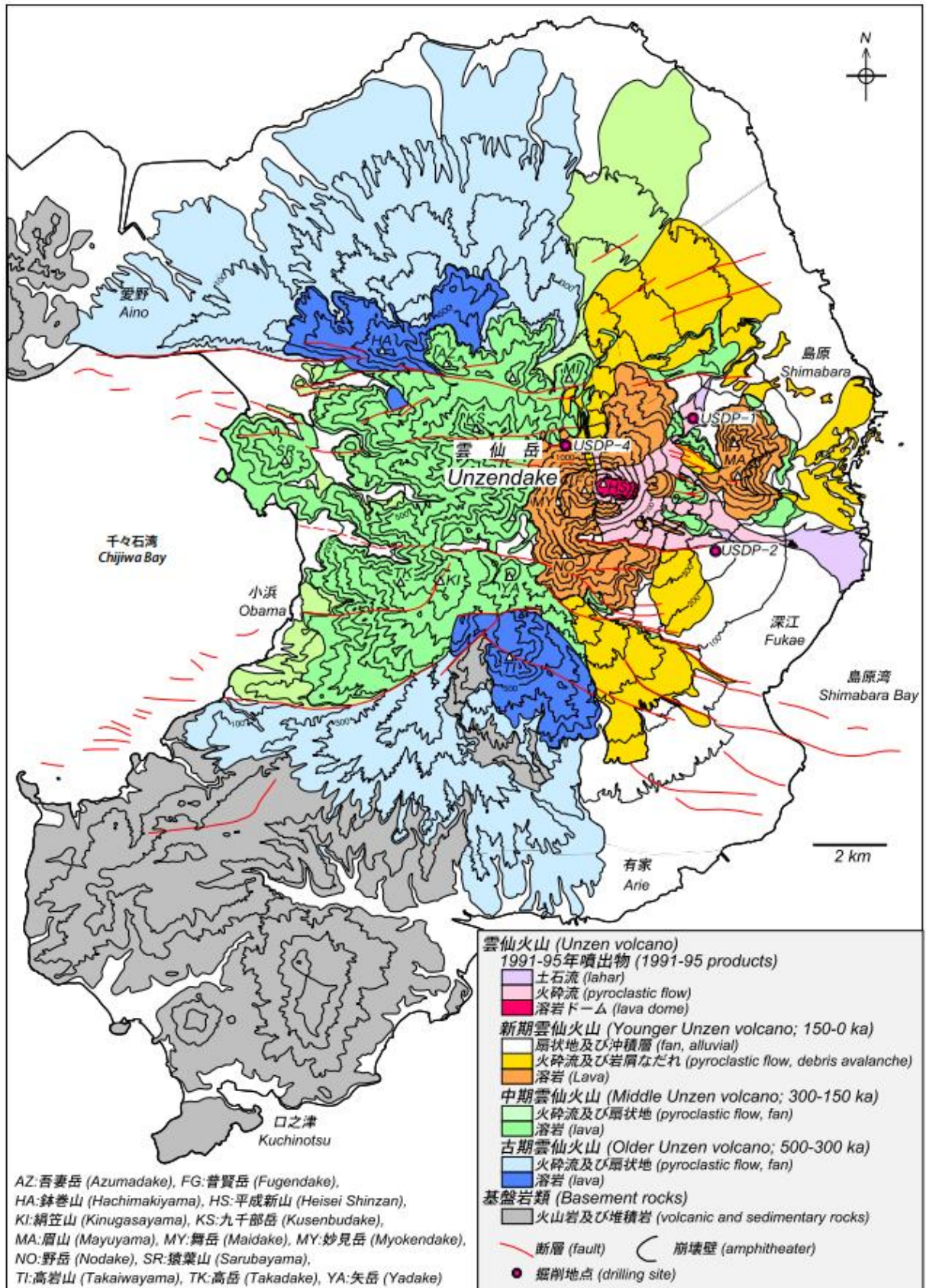


Fig. 3.4 Geologic sketch map of Unzen volcano with age data (Shimizu et al. 2007)



Fig. 3.5 Photos show the sampling locations: a) Sample Unzen-1 was taken from an exposed slope along the upstream of a check dam constructed in 2012-2013; b) Sample Unzen-2 was taken from the coastal area

During the investigation of Unzen-Mayuyama area for researching this historical megaslide, we chose two samples, one in the source area and one from the coastal area outside the landslide moving area. The location of sampling is shown in Figure 3.2 and the sample site is shown in Figure 3.5. Sample Unzen-1 was taken from a sand layer exposed along a torrent gully in the source area of the landslide. Sample Unzen-2 was taken from the coastal area outside the landslide area to represent the soil overridden by the landslide. The mountain consists of volcanic lava rock and unconsolidated eruption products (debris and sands). The sliding surface of the landslide probably formed within a sandy layer rather than in the strong intact lava rocks and boulders. We took samples from a sandy zone exposed along a torrent gully side slope in the source area. The grain-size distribution of the samples is shown in Figure 3.6 in which the Unzen-1 sample is finer than the Unzen-2 sample. The component of the sample 1 was 91% sand and 9% fine, while sample 2 was almost sandy particles.

Figure 3.7 presents the unit weight of soils in the Unzen volcano. We consolidated the sample in the ring-shear apparatus under different normal stress from 0 to 3 MPa in a saturated condition. The saturated unit weight of Unzen sample was 21 kN/m^3 at 3 MPa normal stress, and the dry unit weight was 19 kN/m^3 at 3 MPa. In shallower areas, the value would be smaller and we assumed a single value of 19.5 kN/m^3 for the entire area.

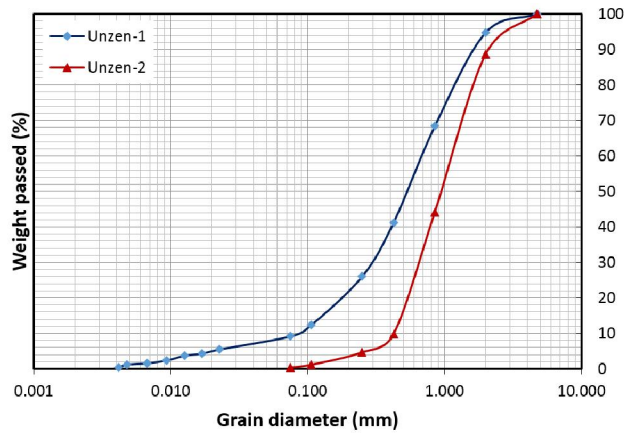


Fig. 3.6 Grain size distribution of sample Unzen-1 and Unzen-2

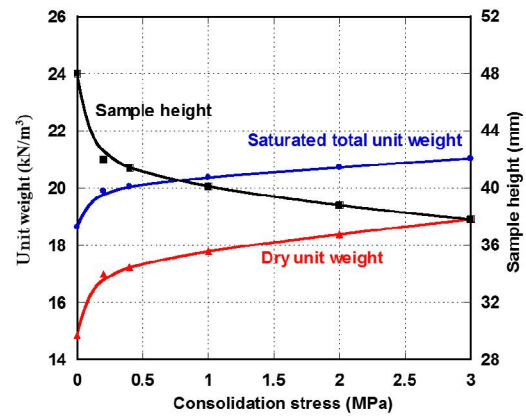


Fig. 3.7 Dry and saturated unit weight of Unzen-1 sample at different consolidation pressure

3. 1. 2 The Recent Hai Van Large-Scale Landslide in Vietnam

The second case of landslide for applying the new high-stress ring-shear apparatus is an active large-scale landslide located at Hai Van pass, Da Nang city, Vietnam. Figure 3.8 presents the location and topography of this landslide study site.

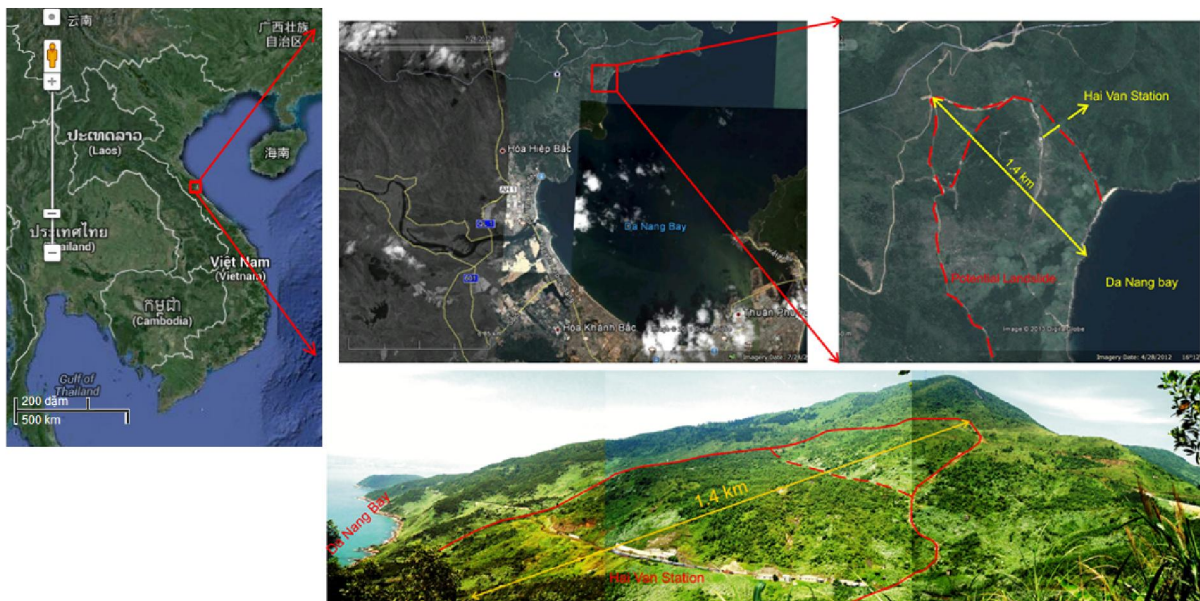


Fig. 3.8 Location and topography of Hai Van station landslide, Da Nang city, Central region in Vietnam

Hai Van area is located between Hue city and Da Nang city in middle of Vietnam, and topography of this area is characterized mountain ridge from 500m to 1500m above sea level which belongs to Annamite Mountain Range in Indochina Peninsula.

The two Vietnam transport routes, consist of Vietnam's National highway No.1, and the North-South Railway cross the Hai Van pass. The road crosses over the mountain more or less directly, climbing to an elevation of 496 m and passing south of the 1,172 m high Ai Van Son peak, while the railway hugs the coastline more closely, passing through a series of tunnels along the way.

Hai Van station is located on the sea side-slope of Hai Van pass at the height of 127 m (Figure 3.9). It has a great significance to traffic flow efficiency along the national railway. Every day, there are over 30 trains pass through this station. However, this area is often affected by landslides, for example landslides in the years of 1999, 2005, and 2007. In particular, the landslide in 1999 damaged seriously the Hai Van station and stopped its operational process several days.

The landslide in this research is the biggest landslide in Hai Van Mountain with the length of 1040 m, and depth of displaced mass of 100 -120 m. Estimated dimensions and the geometry of the landslide mass are showed in Table 3.1.

Table 3.1 Properties of Hai Van station landslide

	Properties
Length (m)	1040
Width (m)	940
Depth of slip surface (m)	100-120
Slope gradient (degrees)	20-25
Altitude (m)	280
Bed rock	Granit
Type of landslide	Deep-seated rotational landslide
Observation devices	Extensometer

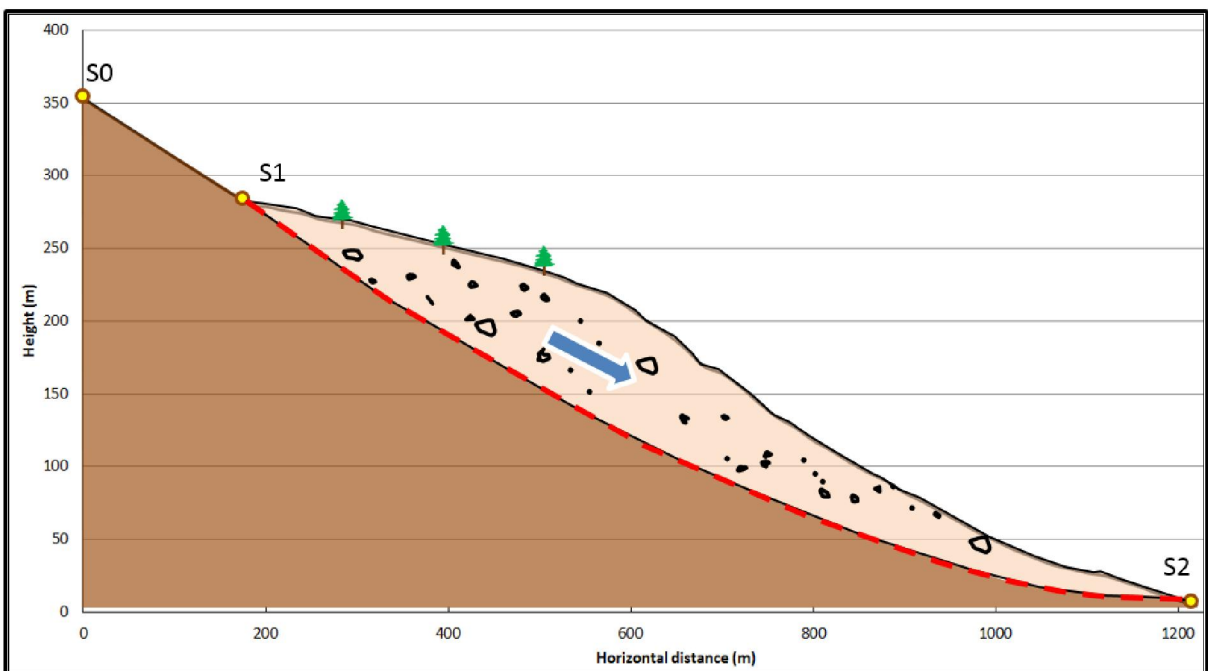
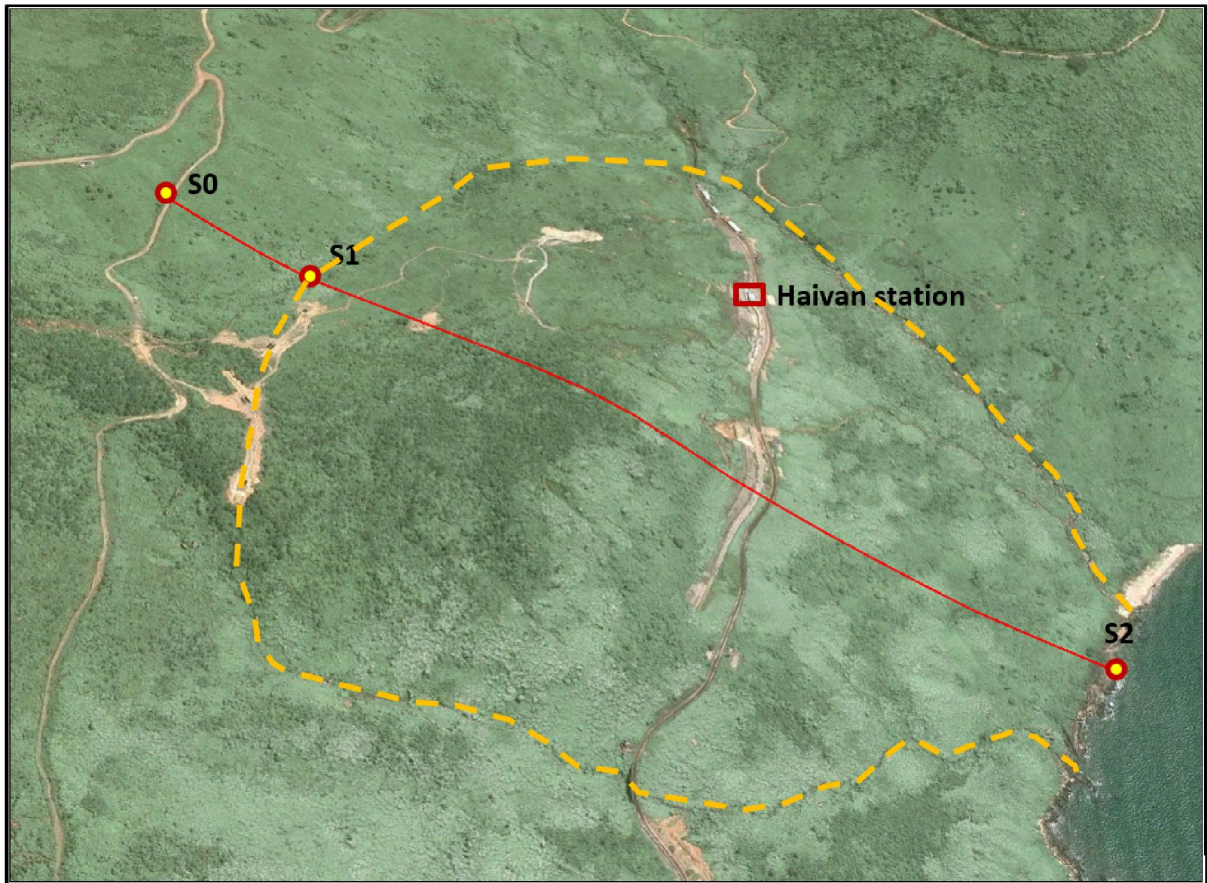


Fig. 3.9 Topography (up) and section (down) of Hai Van station landslide

Hai Van station landslide is one of the pilot study areas in the Vietnam-Japan joint research project for development of landslide risk assessment technology. The most important work in this area is to establish a landslide monitoring system for the purpose of an early warning for the safe of passengers using trains and the Hai Van

station as well. The sensor network being installed at the Hai Van station landslide area includes a robotic total station, Global Navigation Satellite System, extensometers, rain gauges, and inclinometers and vertical extensometers in boreholes.

Until now, three bore holes (BH1 with 30 m depth, BH2 with 60 m depth, BH3 with 80 m depth) and some monitoring equipment such as rain gauges, extensometers, inclinometers have been carried out in this area to survey geology, observe rainfall and displacement of the landslide mass (Figure 3.10). The daily variation of rainfall and slope displacement from 10 May 2013 to 17 January 2014 was observed and shown in Figure 3.11 (Asano et al. 2014). The accumulative displacement in this period is around 19 mm and the large displacement observed after the heavy rainfall period from 18 September 2013 to 16 November 2013. It indicates that Hai Van station landslide is an active landslide with slow movement and failure may occur in the future.

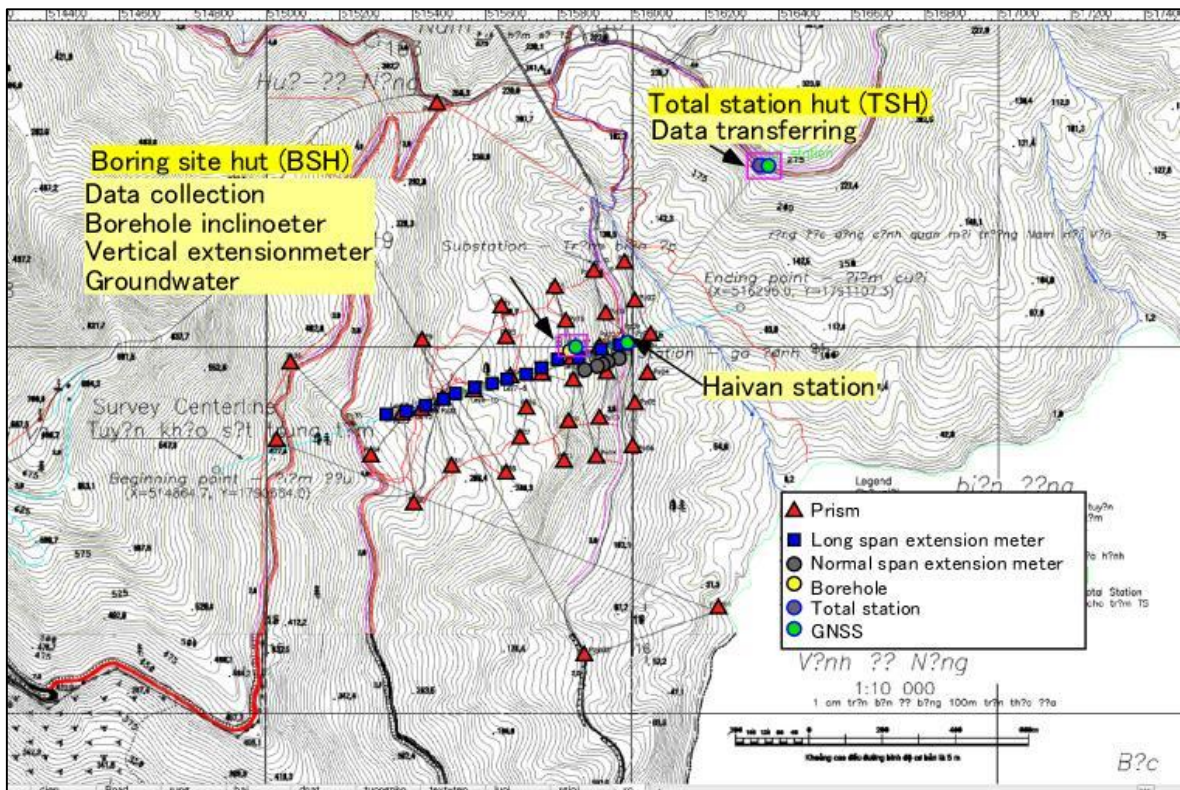


Fig. 3.10 Location map of bore holes and monitoring equipment on Hai Van station slope

Climatic and geological settings

Due to its geographical location, the overall climate of Da Nang area is strongly affected by typical tropical monsoon weather and is influenced by climates from both northern and southern Vietnam. The region has two distinct seasons with high annual

temperature and precipitation (Table 3.2) (Tien, 2015). The average annual precipitation in Da Nang is approximately 2300 mm, of which most of the precipitation occurs in the rainy season that lasts from September to December, and it is followed by a relatively dry period from February to April (as shown in Figure 3.11). During the latter period, the northeast monsoon dominates.

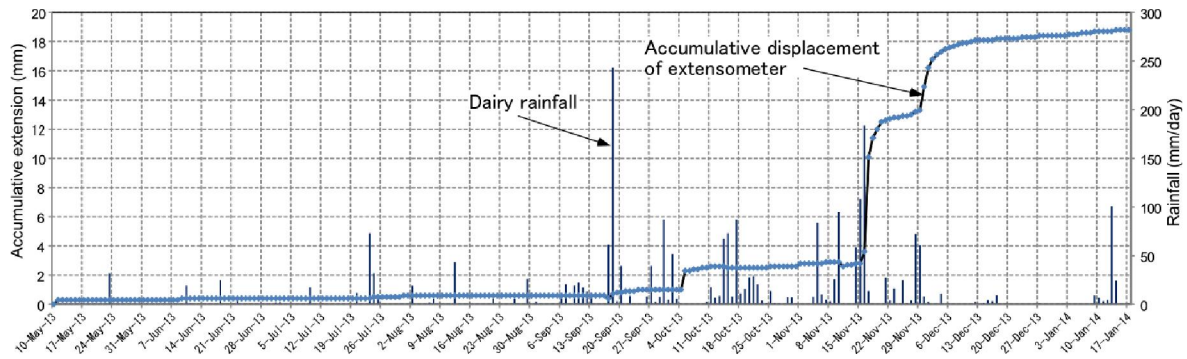


Fig. 3.11 Monitored rainfall and slope movement at Hai Van station (Asano et al. 2014)

The annual temperature variation ranges from 22.7°C to 29.9°C, and the average monthly temperature is 26°C. July is the hottest month and January is the coolest month with the average temperatures at 34.3°C and 18.5°C respectively. The annual humidity varies from 74% to 84% and there are about 144 rainy days and 2108 sunshine hours per year.

Moreover, annually this study area usually faces 1-5 typhoons (Mai 2005) occurring from August to November and bringing heavy rainfall with gust velocity up to 100km/h and choppy sea.

Table 3.2 Climatic data for Da Nang area

Climate data for Da Nang													
Month	Jan	Feb	Mar	Apr	May	Jun	Jul	Aug	Sep	Oct	Nov	Dec	Year
Record high °C	32	35	37	41	39	38	38	38	37	36	35	32	41
Average high °C	24.8	26.1	28.7	31	33.4	33.9	34.3	33.9	31.5	29.6	27	24.9	29.9
Daily mean °C	21.7	23	25.1	27.2	29.2	29.7	29.8	29.7	27.8	26.4	24.3	22.1	26.3
Average low °C	18.5	19.8	21.5	23.3	24.9	25.5	25.3	25.5	24.1	23.2	21.6	19.3	22,7
Record low °C	8	7	11	7	18	20	17	21	21	12	7	11	7
Precipitation mm	111.1	47.78	43.59	49.67	81.93	69.33	97.21	174.8	328.5	556.7	470.2	248.2	2,279
% humidity	83	83	83	82	78	75	74	76	81	84	84	84	80.6
Avg. rainy days	14	7	5	6	9	8	9	12	16	22	21	19	144
Mean monthly sunshine hours	136.4	144.1	105.4	207	257.3	237	257.3	207.7	174	145.7	120	116.6	2,108

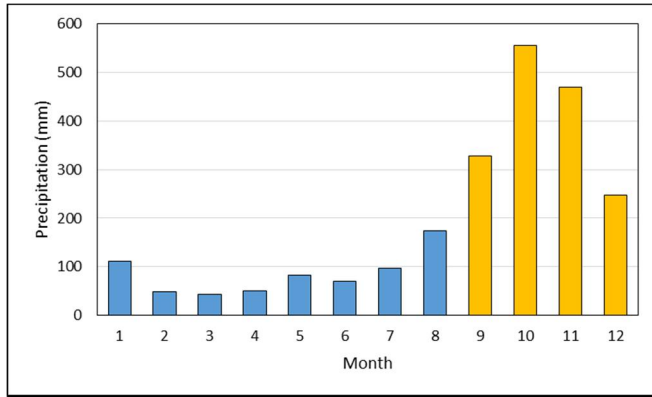


Fig. 3.12 Average monthly precipitation in Da Nang area, Vietnam

According to the result of field investigations, geological map (Figure 3.13), and lithologic description (Figure 3. 14), geological structure of this study area is mainly composed of granite, called Hai Van complex intruded in Triassic period of Mesozoic Era (from 200 million to 250 million years ago). The Hai Van complex includes three phases: phase 1 ($\gamma aT_3 hv_1$) is biotite granite and two mica-granite, phase 2 ($\gamma aT_3 hv_2$) is biotite granite, and phase 3 ($\gamma aT_3 hv_3$) consists of granite aplite, tourmaline- and garnet-bearing pegmatite veins. The boundary of those rocks is very clear. Granitic rock is weathered highly and completely until a certain depth under surface due to deep weathering. Major fault of this area is running NW-SE and NE-SW. The vertical geological section at the bore hole was described as: depth 0 to 49.15m is a weathered coarse granite layer includes clay sand and solid granite; depth 49.15 to 51.0m is a loose sand layer; depth 51.0 to 54.0 m is a weathered fine granite layer; and from depth 54m is granite bedrock. The loose sand layer was expected to be the sliding surface of the landslide.

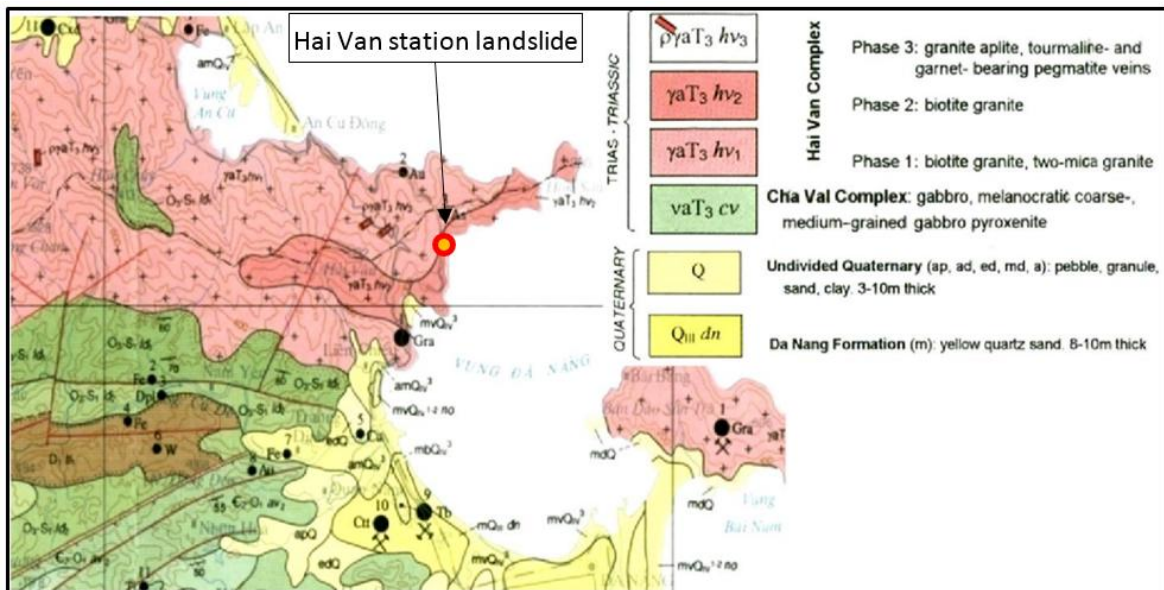


Fig. 3.13 Geological structure of Hai Van Mountain and location of Hai Van station landslide

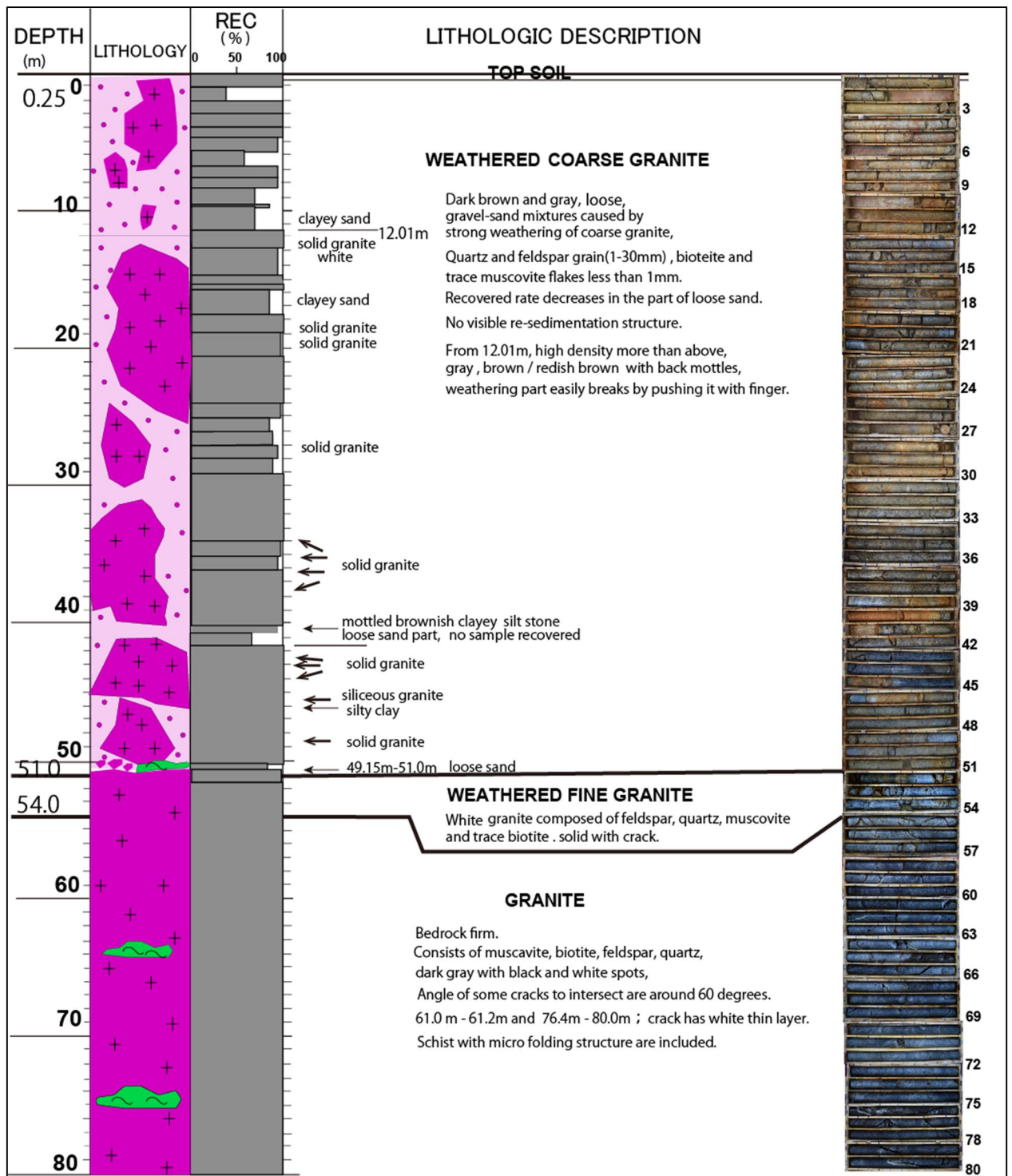


Fig. 3.14 Lithologic description of the Hai Van station slope collected from the bore hole

Soil Characteristics

In order to obtain the characteristics of weathered materials in the study area, two surface sample were taken from the location assumed to have similar material to the sliding surfaces of the potential landslides. The first sample (Haivan-1) is weathered brown granitic sand, and the second one (Haivan-2) is less weathered white granitic

sand. These two samples present for the weathered soil in this area. Sampling locations and photo of the white sand are shown in Figure 3.15.

Then, the two samples was transported to the laboratory of the International Consortium on Landslides in Kyoto University and tested to determine their physical and geotechnical properties by using conventional tests and ring-shear tests. The first is unit weight measuring by consolidating samples in the ring-shear apparatus in a saturated condition. Figure 3.16 presents the consolidation stress, sample height, dry unit weight and saturated unit weight of the samples. The saturated unit weight of Hai Van-1 reached 22.2 kN/m^3 at 400 kPa , and the saturated unit weight of Hai Van-2 reached 21.2 kN/m^3 at 500 kPa , while the dry unit weight of them reached 19 kN/m^3 and 16.5 kN/m^3 respectively.



Fig. 3.15 The sampling location in Hai Van pass area (image from Google Earth) (A) and photos of white granitic sand (Hai Van-2) taken for deep-seated landslide

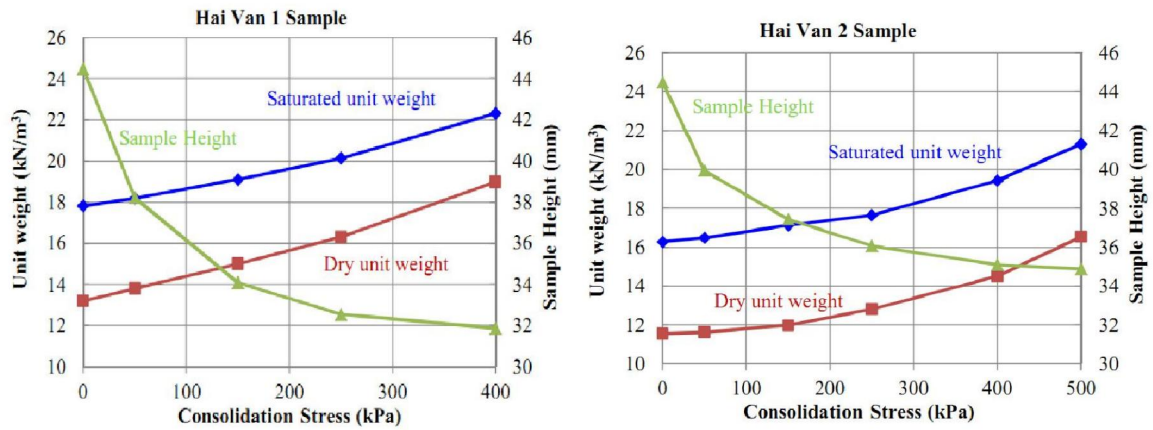


Fig. 3.16 Dry and saturated unit weight of Hai Van-1 sample (left) and Hai Van-2 sample (right) at different consolidation pressure (from Tien, 2015)

Hai Van sample weathered from granitic rock mainly consists of quartz, feldspar, clay materials (kaolin), mica. Among them, mineral of quartz is the largest component with approximately 70% (Phuc 2009). Figure 3.17 shows the grain-size distribution of the two samples. From the result of the particle analysis, the Hai Van-1 sample has more fine particles than Hai Van-2 sample. Using ASTM soil classification standard, two samples were classified as clayey sand/silty sand, in which Hai Van-1 consists of 67 % sand, 33 % fine and Hai Van-2 consists of 78 % sand, and 22 % fine.

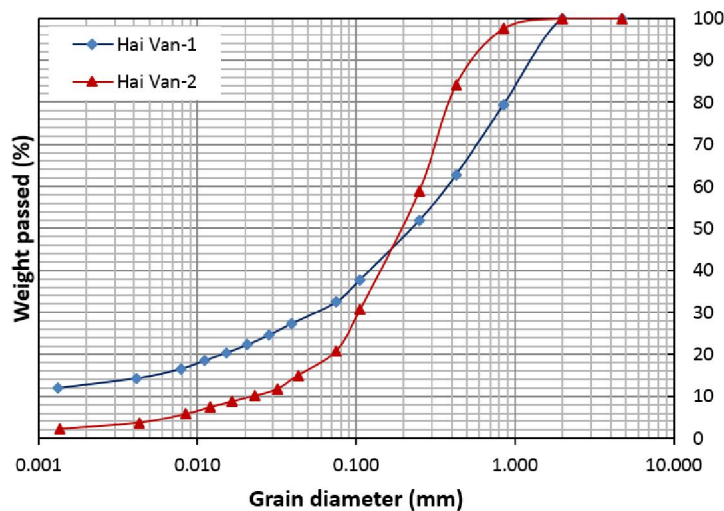


Fig. 3.17 Grain size distribution of sample Hai Van-1 and Hai Van-2 (from Tien, 2015)

3.2 Basic Tests of the ICL-2

A series of basic tests of drained speed control test, undrained monotonic stress control test were conducted to measure the geotechnical properties of the samples and

also examine the capacity and performance of the new high-stress dynamic-loading ring-shear apparatus.

3.2.1 Drained speed control test

The best way to measure the friction angles of the samples (peak friction angle ϕ_p , friction angle during motion ϕ_m) and to check the apparatus in drained condition is the drained speed control test (Sassa et al. 2014).

Figure 3.18 shows the stress path and time series data of drained speed control test on Unzen-1 sample taken from sand layer exposed along a torrent gully in the source area of the 1792 Unzen-Mayuyama landslide. After saturating with B_D value of 0.97, the sample was consolidated to 3000 kPa and sheared under constant shear speed of 0.2 cm/s in the drained condition. When shear resistance reached peak value of 2450 kPa, the normal stress was reduced to zero with a rate of 5 kPa/s. The failure line and the friction angle during motion was obtained as shown in the left graph of Figure 3.18. The right graph illustrates the temporal variation of total normal stress, shear resistance and pore water pressure. In this case, pore water pressure value was zero due to drained condition.

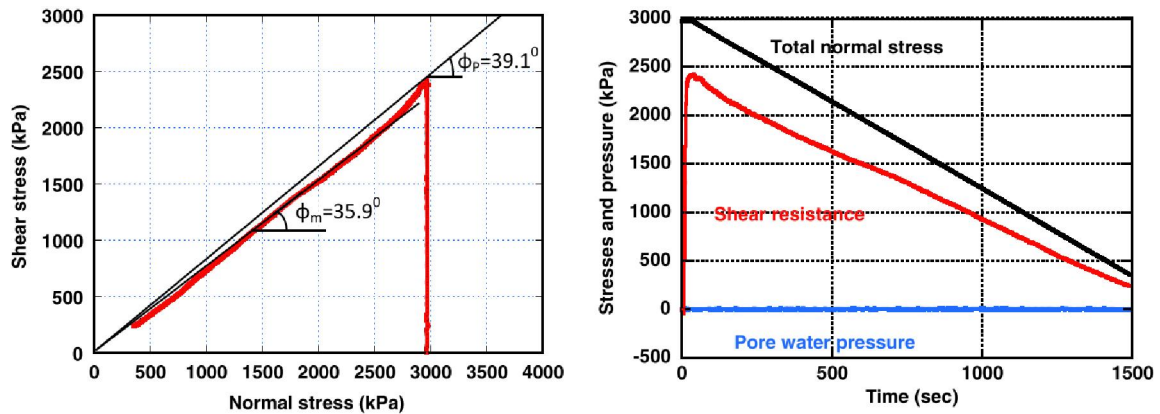


Fig. 3.18 Drained speed control test on Unzen-1 sample

$B_D = 0.97$, shear speed = 0.2 cm/s. After reaching the peak, the normal stress was reduced by the rate of $\Delta\sigma = 5$ kPa/s

Figure 3.19 illustrates the drained speed control test on Hai Van-2 sample. This test was conducted under the total normal stress of 1000 kPa. As the same testing process with Unzen-1 sample, Hai Van-2 sample was saturated and consolidated to 1000 kPa at the increasing rate of 2 kPa/s. Then a speed control test was done under constant shear speed of 0.1 cm/s in drained condition. The sample was shear until the total normal stress decreased to zero. The Left graph in Figure 3.19 shows the stress path

reached and moved down along the failure line, with peak friction angle of 35.0° , friction angle during motion of 33.0° .

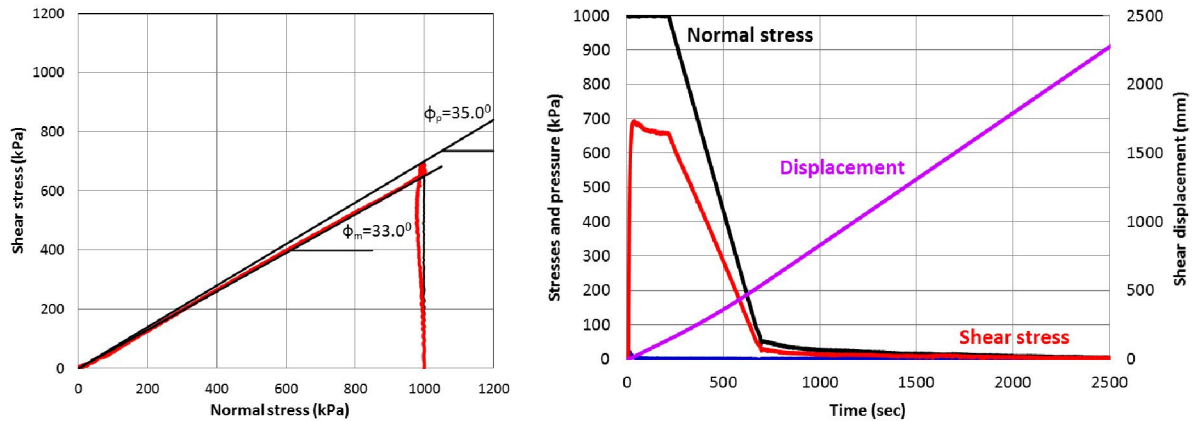


Fig. 3.19 Drained speed control test on Hai Van-2 sample. $B_D = 0.94$, shear speed = 0.1 cm/s . After reaching the peak, the normal stress was reduced by the rate of $\Delta\sigma = 2 \text{ kPa/s}$

These drained speed control tests on the two sample with different normal stress (3000 kPa on Unzen-1 sample, 1000 kPa on Haivan-2 sample) indicated that the control system and monitoring system of the ICL-2 could successfully function under high normal stress of 1000 kPa, or even under very high normal stress of 3000 kPa.

3.2.2 Undrained stress control test

Undrained stress control test is used to simulate landslide because it can provide appropriate shear stress acting within the slope due to the effect of the triggering factors such as rainfall, earthquake, or changes of slope profiles. Figure 3.20 is undrained monotonic stress control tests on Unzen-1 samples. These tests were conducted under four different normal stress of 300 kPa, 1000 kPa, 2000 kPa and 3000 kPa. The testing conditions and obtained results including shear resistance at peak, friction angle of the peak failure line ϕ_p , friction angle during motion ϕ_m , and steady state shear resistance τ_{ss} are presented in Table 3.3.

For each test, the sample was first fully saturated (B_D values from 0.93 to 0.96) and consolidated to the predetermined normal stresses in drained condition. After initial normal stresses were applied, shear box was changed to the undrained condition by closing all water valves. Then shear stresses were increased gradually at a rate of 1 kPa/s, 2 kPa/s and 5 kPa/s. The effective stress paths of all tests reached the same failure line and then went down along the failure line until reaching a certain value due to the generation of pore water pressure (steady state shear resistance). This

phenomenon of pore water generation is called as “sliding-surface liquefaction” proposed by Sassa in 1996 and elaborated in 2004, 2010, 2014. It is widely accepted as a key concept for pore-water pressure generation in a shear zone and post-failure motion of landslide.

Table 3.3 Condition and results of undrained monotonic stress control test on Unzen-1 sample

Normal stress, σ (kPa)	Friction angle at peak, ϕ_p (deg.)	Friction angle during motion, ϕ_m (deg.)	Steady state shear resistance, τ_{ss} (kPa)
375	39.8	38.5	37
1030	41.2	40.5	45
1900	40.7	39.8	80
2900	40.3	40.3	120

In the sliding-surface mechanism, the sample in the shear zone were crushed during shearing under a normal stress greater than the normal stress at steady state, which results in a volume reduction of soil sample. The reduction of volume in a fully saturated undrained state will generate excess pore water pressure, then reduce the effective stress and mobilized shear resistance.

Firstly, the stress path at a normal stress of 375 kPa (Figure 3.20(a)) reached the failure line (39.8°) showing dilative behavior and then decreased along the failure line until it reached a steady-state shear resistance of 37 kPa. Negative pore-pressure was measured just before failure. After failure, the pore pressure increased during shear displacement. This is a typical sliding-surface liquefaction behavior for a dense material: dilation of the sample near failure caused negative pore pressure, and grain crushing occurred in the shear zone. The resulting volume reduction, together with the accumulating post-failure shear displacement, generated positive pore pressure, even in the dense material.

Shear behavior at 1,030 kPa (Figure 3.2(b)) normal stress was similar, but there was no negative pore pressure, although a zero pore pressure was measured just before failure. The steady-state shear resistance was 45 kPa, slightly higher than in the test at 375 kPa. The friction angle of the peak failure line was 41.2°, which also was slightly higher than at 375 kPa.

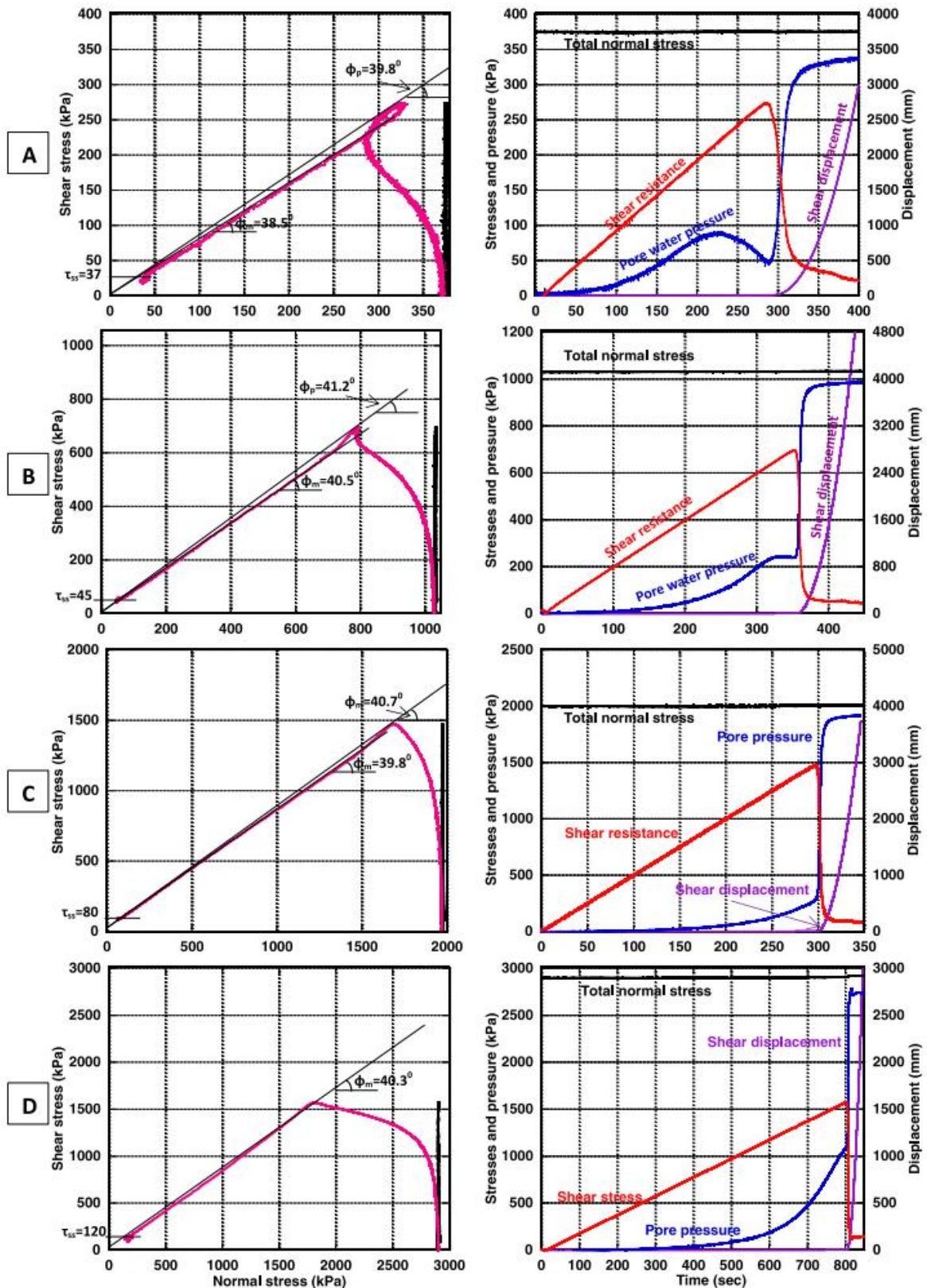


Fig. 3.20 Stress paths (left side) and time series data (right side) of the undrained monotonic stress control tests on Unzen-1 sample with different normal stress from 300 kPa to 3000 kPa. Normal stress = 375 kPa, $B_D=0.93$, $\Delta\tau=1$ kPa/s; b) Normal stress = 1,030 kPa, $B_D=0.95$, $\Delta\tau=2$ kPa/s; c) Normal stress = 1,970 kPa, $B_D=0.95$, $\Delta\tau=5$ kPa/s; d) Normal stress = 2,900 kPa, $B_D=0.96$, $\Delta\tau=2$ kPa/s

Shear behavior at 1,970 kPa (Figure 3.20(c)) normal stress was contractive. Pore-water pressure was generated during shearing before failure. The steady-state shear resistance was 80 kPa. Shear behavior at a normal stress of 2,900 kPa, close to 3 MPa (Figure 3.20(d)) presented a more contractive stress path and reached a failure line of 40.3° , then went down the line to a steady-state shear resistance of 120 kPa. The stress paths and time-series data of these four undrained monotonic stress-controlled tests showed no aberrations, and did not conflict with previous ring-shear tests such as those reported by Sassa et al. (2004, 2010) and others.

Then, all stress paths are plotted in the same graph in Figure 3.21. As shown, the four tests overlapped along the failure line during motion at 39.8°

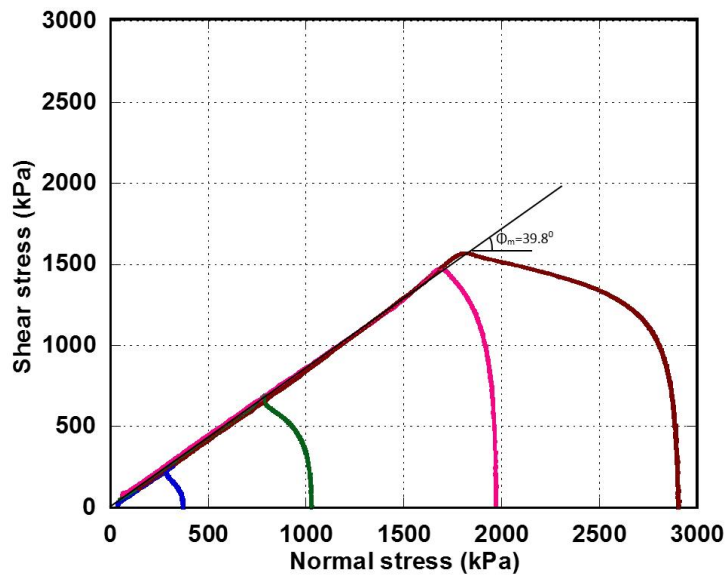


Fig. 3.21 Stress paths of undrained monotonic stress control tests on Unzen-1 sample

Figure 3.22 shows the time series data and stress path of the undrained monotonic stress control tests on Hai Van-2 sample that reached the failure line and moved down along the failure line, with an observed peak failure line. The straight line fitting the stress path gave values of the friction angle during motion, and also at peak as $\phi_p = \phi_m = 36.4^\circ$.

These undrained monotonic stress control test results presented above show the undrained capability, stress control capability and pore water pressure monitoring of the new ring-shear apparatus were successful up to 3 MPa.

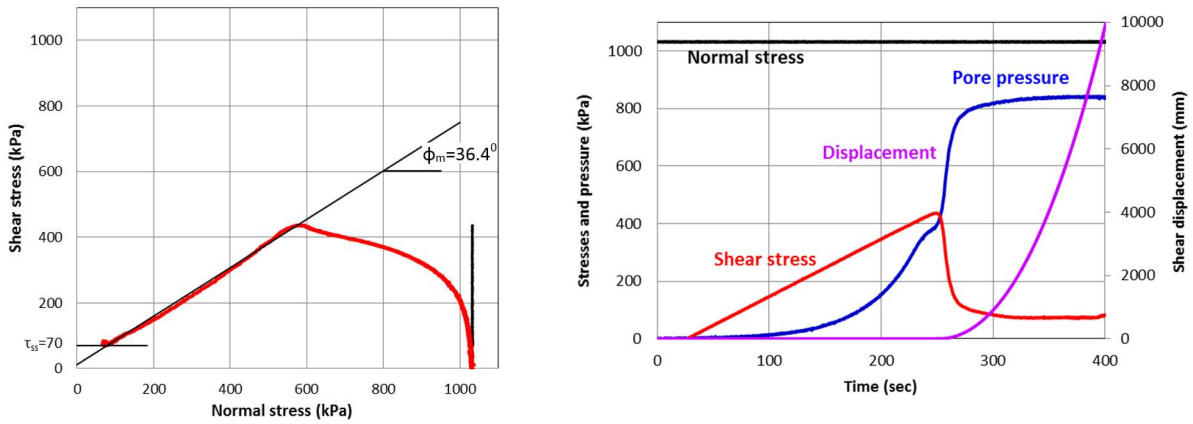


Fig. 3.22 Undrained monotonic stress control test on Hai Van-2 sample

3.3 ICL-2 tests for simulating initiation and motion of the landslides

In order to simulate natural initiation and motion of landslides we conducted some type of tests includes pore water pressure control tests, undrained cyclic loading tests, undrained dynamic-loading tests and undrained seismic loading tests. Naturally drained pore-water pressure control tests were made to trigger landslide failure by increasing only the pore-water pressure, while undrained cyclic and seismic loading tests to simulate dynamic-loading and earthquake induced landslides.

3.3.1 Pore-water pressure control test

Pore-water pressure control test is the first basic test to simulate the failure and post failure of landslide corresponding to rainfall. The landslide initiation mechanism due to pore water pressure are illustrated in Figure 3.23 (Sassa et al. 2013). The initial stress acting in a soil column of a landslide-prone slope is plotted as point I (σ_0 , τ_0). When rainfall infiltrates into the slope, ground-water level/pore-water pressure (u) increases. This reduces the effective normal stress ($\sigma-u$) acting in the slope and the stress moves to the left and shear failure will occur at the stress at failure of the failure line expressed by following equation:

$$\tau = c + (\sigma - u)\tan\varphi \quad (3.1)$$

Where: τ_f is shear stress at failure, σ is normal stress, c is cohesion, and φ is internal friction angle.

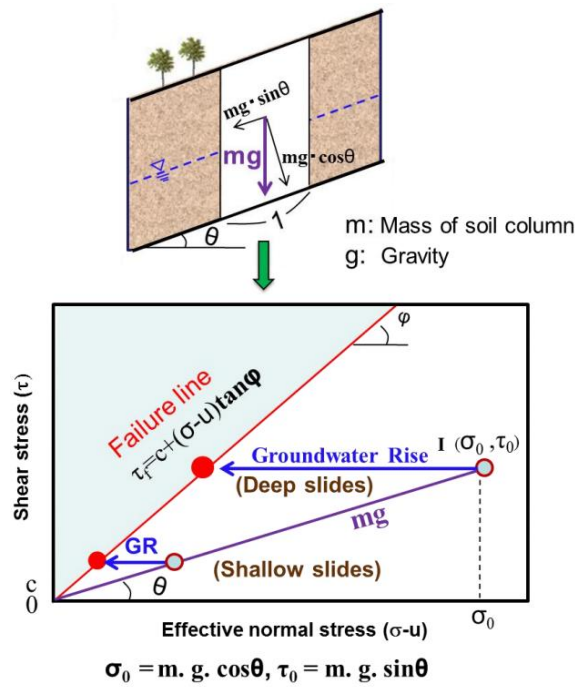


Fig. 3.23 Mechanism of landslide initiation due to pore-water pressure rise (from Sassa et al. 2013)

Figure 3.24 shows stress path and time series data of pore-water pressure control test on the sample (Unzen-1) taken from the source area of Unzen-Mayuyama landslide. The sample was saturated with B_D value of 0.98, then the initial stresses on the sliding surface were reproduced in the apparatus with 3.0 MPa normal stress and 1.5 MPa shear stress (shown as black line in Figure 3.24). This initial condition corresponded to a slope inclination of 26.5° . This is similar to the slope of the main landslide block in Figure 3.3. Then, the pore-water pressure was gradually increased until failure at a rate of $\Delta u = 1$ kPa/s. The pore-water pressure is supplied to the shear box through the middle drainage valve (Figure 2.4 and Figure 2.5). Therefore, the water is free to move from the pore-water pressure control unit through the middle valve and it is considered to be a natural drained condition. As shown in Figure 3.24, failure occurred at a pore-water pressure of 1.2 MPa (a pore-water pressure ratio $r_u = 1.2/3.0 = 0.4$). Then stress path suddenly dropped to a lower value of 113 kPa. The friction angle at failure was 39.4° .

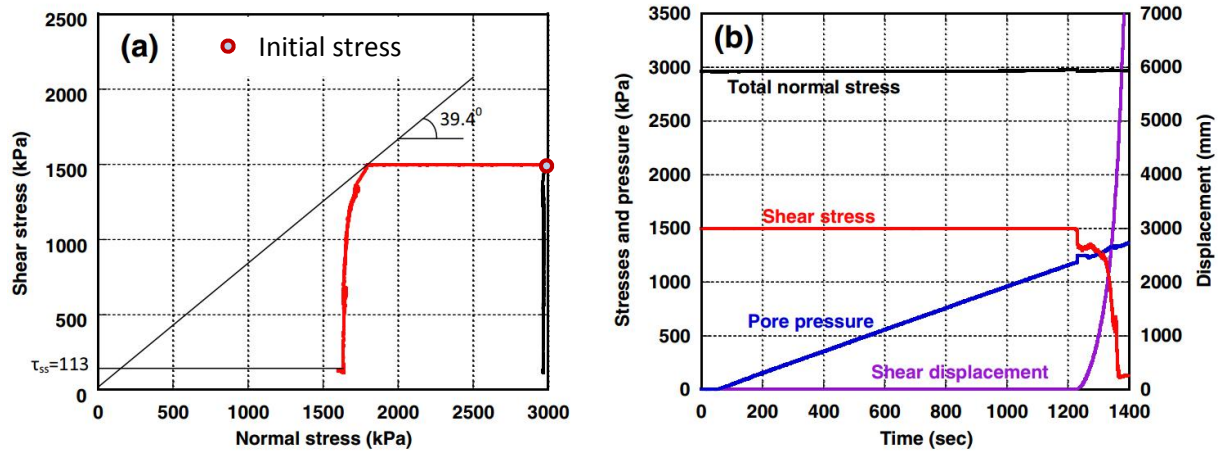


Fig. 3.24 Pore-water pressure control test on sample Unzen-1 ($B_D=0.98$, Initial normal stress of 3 MPa and initial shear stress of 1.5 MPa). a) Stress path; b) Time series data for normal stress, shear stress, pore-water pressure, and shear displacement.

We conducted the same test schedule on Hai Van-2 sample to simulate rainfall induced landslide for Hai Van station slope. The Hai Van station landslide is smaller and gentler than Unzen-Mayuyama megaslide with the initial estimated depth of sliding surface around 100 m and slope inclination of around 20° . Thus, the sample was consolidated to 1.5 MPa normal stress and 0.6 MPa shear stress in the drained condition. This initial stress corresponds to a slope of 21.8° . Then pore-water pressure was gradually increased at a rate of 1 kPa/s. Failure occurred at pore-water pressure of 730 kPa, that is, a pore-water pressure ratio $r_u = 730/1500 = 0.49$ (Figure 3.25).

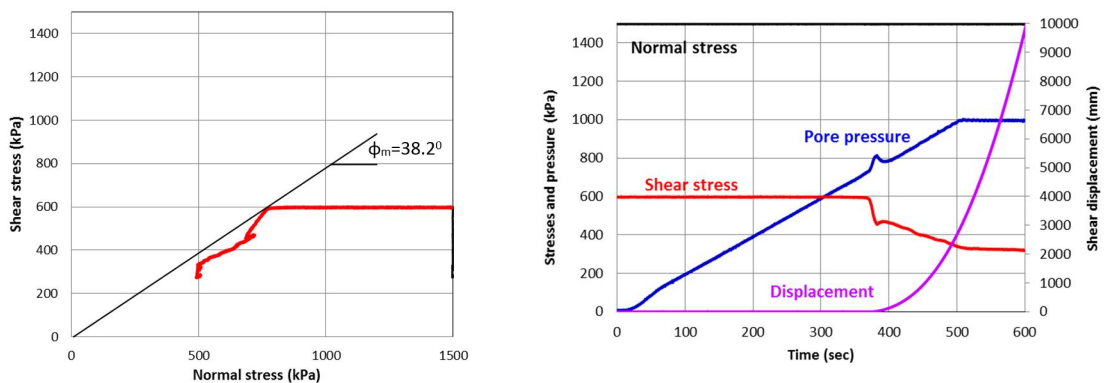


Fig. 3.25 Pore pressure control test on Hai Van-2 sample

3.3.2 Undrained cyclic loading test

The second test was performed to simulate dynamic-loading induced landslide is undrained cyclic loading test. Landslides in Vietnam are almost triggered by rainfall

and there has no earthquake induced landslide. So that, in this research, we just conducted seismic and dynamic-loading test for simulating landslide in Japan.

Initially, the Unzen-1 sample was fully saturated ($B_D = 0.98$) and consolidated at 2.0 MPa normal stress, and 1.2 MPa shear stress in drained condition. This initial stress state corresponded to the slope angle of $\arctan(1.2/2.0) = 31.0^\circ$. Then we changed to the undrained condition of shear box by closing the valves and applied the control signal for the undrained cyclic loading test. An initial cycle of shear stress increment of ± 300 kPa was to be loaded as a sine curve, in which the second, third and fourth cycles of shear stress were increased ± 300 kPa in each step. It was expected that the sample would be failure before the loading of fourth cycle when the final shear stress reached 2.4 MPa. After that, three loading cycle were kept constant before the cyclic shear stress was reduced to zero. During applying this cyclic shear stress by sending computer control signal (green line in Figure 3.26(b)) to the servo-amplifier, the normal stress was held constant of 2.0 MPa (Black line in Figure 3.26). The shear resistance, pore-water pressure, and shear displacement are plotted in Figure 3.26b by red line, blue line and purple line respectively. The shear stress reached the failure line and decreased after the peak of the third loading cycle due to generation of pore water pressure. As shown in the stress path, the peak shear resistance was reached at 1650 kPa, peak friction angle of 40.5° and friction angle during motion of 39.6° were calculated. The steady state shear resistance was 81 kPa. Shearing stopped after 180 seconds and the displacement reached 10 meters.

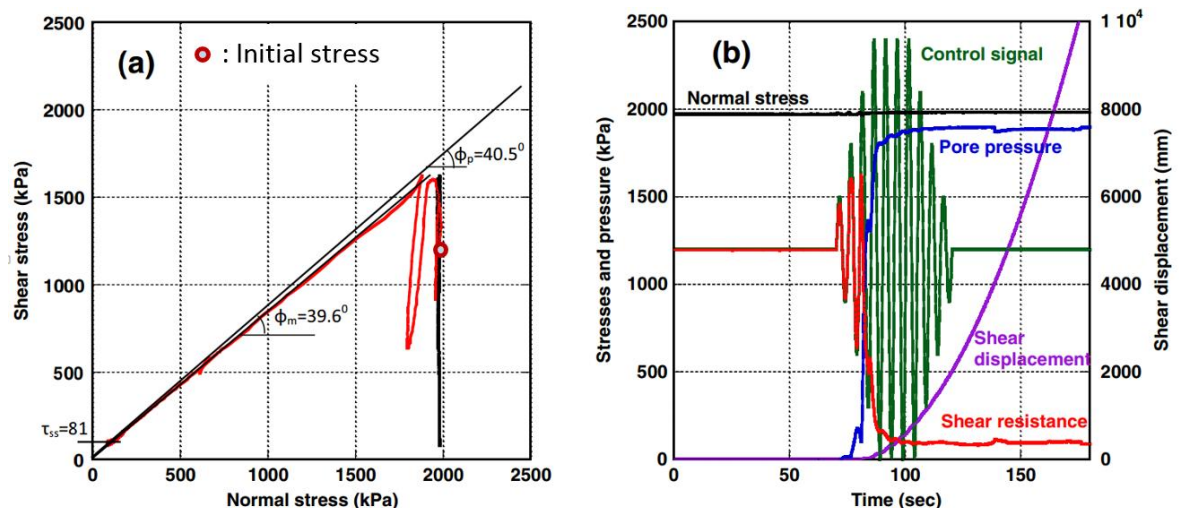


Fig. 3.26 Undrained cyclic loading test on Unzen-1 sample, $B_D = 0.98$. a) Stress path, b) Time series data for normal stress, control signal (cycle rate of 0.2 cycle/s, shear stress step of 300 kPa), and pore-water pressure, shear resistance, and shear displacement.

3.3.3 Undrained seismic loading test

The most advanced and complicated test of the new ring-shear apparatus is a seismic loading test to simulate earthquake induced landslide, in which effect of pore water pressure and earthquake shaking are combined. The mechanism of combined earthquake and pore-water pressure initiated landslide is illustrated in Figure 3.27 (Sassa et al. 2013). Initial stress acting on the sliding surface is expressed by point I (σ_0, τ_0). When rainfall occurs, pore water pressure will increase and make the initial stress point I move to A due to decreasing of effective normal stress ($\sigma-u$). In this state, an additional small seismic stress may cause failure of the soil mass.

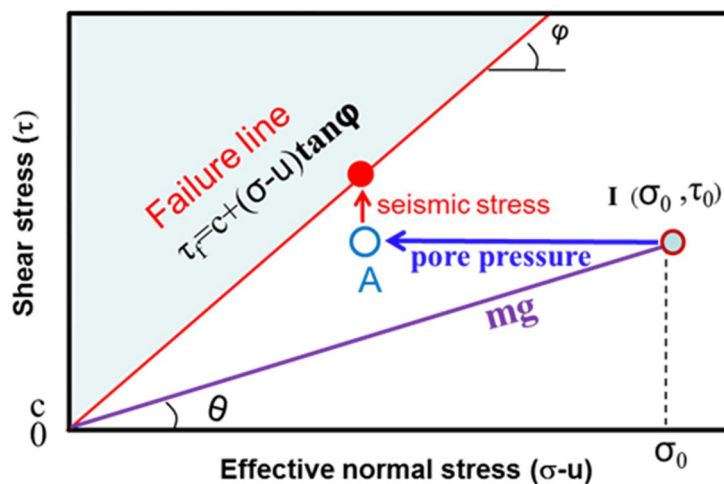


Fig. 3.27 Mechanism of Landslide initiation due to combined effect of seismic loading and pore-water pressure rise (Sassa et al. 2013)

According to the investigation, the 1792 Unzen-Mayuyama landslide was triggered by an earthquake shaking with the estimated magnitude $M=6.4\pm 0.2$ (Usami 1996, reintroduced in Sassa 2014), namely a seismic intensity of VII during the earthquake, estimated by the Unzen Restoration Office. Because of more than 30% of houses were destroyed in the Shimabara area, it is believed that the seismic acceleration was around 400 cm/s^2 or greater. The Japanese seismic intensities (Usami 1996) are:

V: $80\text{-}250 \text{ cm/s}^2$, where walls and fences are cracked, and Japanese gravestones fall down

VI: $250\text{-}400 \text{ cm/s}^2$, where less than 30% of Japanese wooden houses are destroyed

VII: More than 400 cm/s^2 , where more than 30% of the houses are destroyed, landslides are triggered and faults rupture the ground surface.

There was no record of the 1792 earthquake so we investigated recent earthquake induced landslides and chose a similar one to apply for landslide simulation. We used the 2008 Iwate-Miyagi Nairiku earthquake ($M=7.2$) triggered the Aratozawa landslide (67 million cubic meters) in Miyagi prefecture for the ring-shear test and for the computer simulation for 1792 Unzen-Mayuyama landslide. The procedure of this test was carried out as follows. Initially, the saturated sample of Unzen-1 ($B_D=0.94$) was consolidated to 3.0 MPa normal stress. Then 1.5 MPa of shear stress was load in the drained condition to create the initial stress state, corresponding to a slope angle of 26.6° . Then, pore-water pressure was increased with the rate of $\Delta u=2$ kPa/s until pore pressure reached 800 kPa, namely, a pore-water pressure ratio $r_u = 800/3000=2.7$. The exact value of pore pressure ratio was unknown but base on the pore water pressure control test presented above, it must be smaller than 0.4 which could trigger the landslide.

The N-S component of the 2008 Iwate-Miyagi earthquake record was loaded (the maximum acceleration is 739.9 cm/s^2) as the additional seismic stress. Figure 3.28 presents the test result. The right figure shows the time series data of control signal, normal stress, pore water pressure, shear resistance and shear displacement. In the control signal (green line), the maximum value is 2,469 kPa (1500+969 kPa) and the minimum value is 369 kPa (1500-1131 kPa). The acceleration (a) was calculated from the ratio of seismic acceleration and gravitational acceleration: $a/g=969/1500$ or $a/g=1131/1500$, because $ma=960 \text{ kPa}$ and $mg=1500 \text{ kPa}$, expressing the landslide mass at unit area as m . The acceleration corresponds to $(969/1500) \times 980 = 633 \text{ cm/s}^2$ and $(-1131/1500) \times 980 = -739 \text{ cm/s}^2$ (negative acceleration), so the control signal applied to the ring-shear apparatus exactly corresponded to the seismic record.

The failure occurred at the shear stress of 1825 kPa, at $a/g = (1825-1500)/1500 = 0.22$, the necessary acceleration at failure was 215.6 cm/s^2 . This result showed that smaller earthquake shaking could cause failure of the landslide under an initial condition of pore water pressure ratio of 0.27. The friction angle during motion was calculated as 41.0° and the steady-state shear strength was 157 kPa.

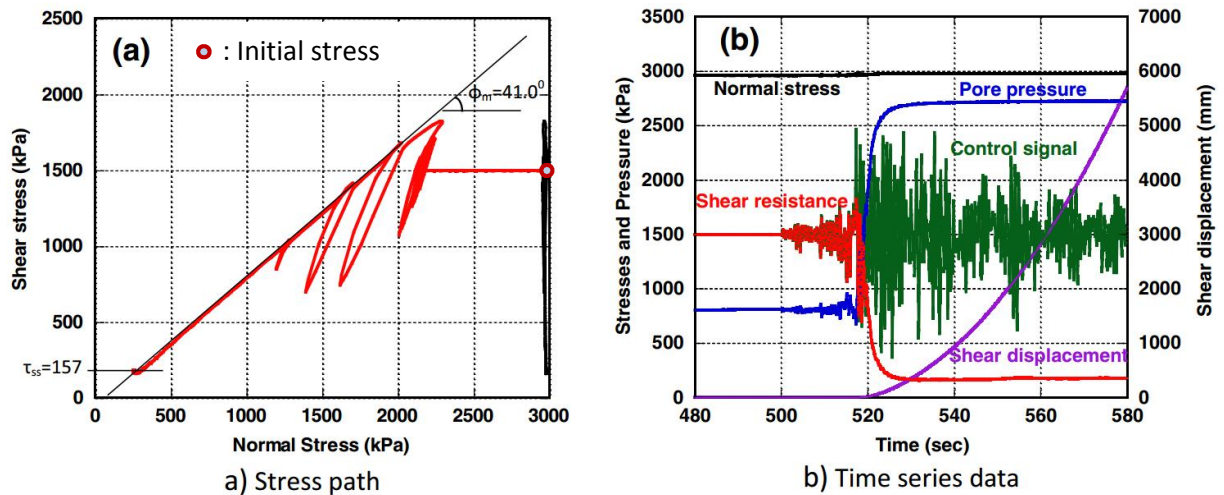


Fig. 3.28 Undrained seismic loading test on Unzen-1 sample taken from the source area . $B_D = 0.94$, pore pressure was 800 kPa, additional seismic loading was from +969 kPa to -1131 kPa, failure stress 1825 kPa

3.3.4 Undrained dynamic-loading test

As presented in previous part, we collected two samples from the Unzen-Mayuyama landslide area during field investigation for simulating complete process of landslide from the initiation to motion. Sample Unzen-1 taken from the source area is to study the initiation of the landslide. Sample Unzen-2 taken from exposed ground along the coast, close to the landslide area, but not covered by the landslide source area mass is to study the motion of the landslide. The sample Unzen-2 was assumed to present soils in the deposition area along the coast.

When the upper landslide mass (red dot zone of Figure 3.3) moves to the lower slope, it applies undrained dynamic-loading to the soil mass of the lower slope (black dot zone in Figure 3.3). This initiated the motion of the lower slope in addition to the motion of the upper part. The last test of the ICL-2 was carried out to research the mechanism of undrained dynamic-loading on the lower layer of Unzen-Mayuyama landslide. The test result are shown in Figure 3.29 with the initial stress state I ($\sigma_0 = 1000$ kPa, $\tau_0 = 150$ kPa) corresponding to a slope inclination of 8.5° . Then normal stress was increase 2790 kPa which is close to the maximum stress of the ICL-2 in undrained condition (black line in Figure 3.29) due to rapid movement of the slide mass. A high pore-water pressure (blue line in Figure 3.29(b)) was generated from the second 15. When shear stress increased to 720 kPa, the lower mass failed and move together with the upper slide mass. The friction angle during motion was 39.4° and the steady state shear resistance reached 80 kPa.

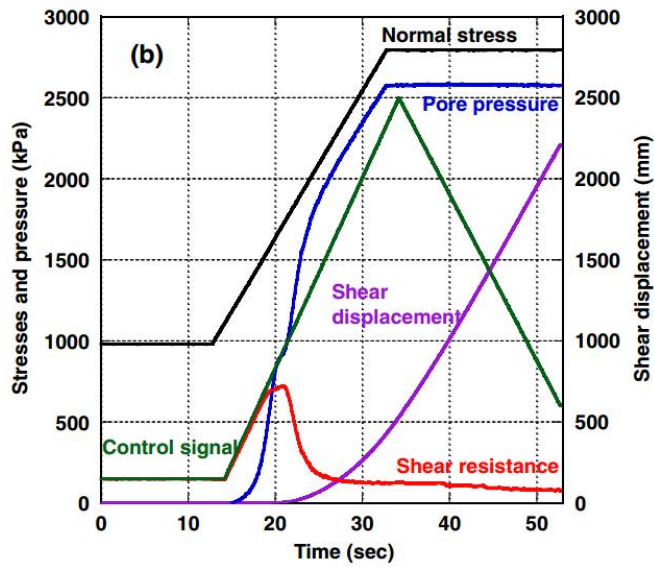
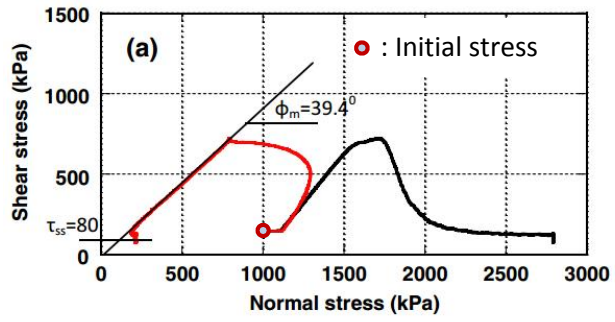


Fig. 3.29 Undrained dynamic-loading test on Unzen-2 sample. $B_D=0.97$, initial stresses ($\sigma_0=1,000$ kPa, $\tau_0=150$ kPa)

Chapter 4 Application of the Measured Parameters to Landslide Hazard Assessment

4.1 Introduction to LS-RAPID Simulation Program

The LS-RAPID is an integrated landslide simulation model developed to assess the initiation and motion of landslides triggered by rainfalls, earthquakes or the combination of rainfalls and earthquakes (Sassa 2010, Sassa 2012, He 2014, Gradiski 2014). This software is the first simulation model can reproduce the whole process of landslide from initial stable state to deposition based on the measured parameters from the ring-shear apparatus (peak friction angle, friction angle during motion, shear resistance at the steady state, and other with physical meaning) (Sassa et al. 2004). Landslide simulated by LS-RAPID can be triggered by pore water pressure (pore water pressure ratio) due to rainfall and resulting groundwater rise or by seismic loading (real seismic record or simple cyclic waves) (Sassa et al. 2014).

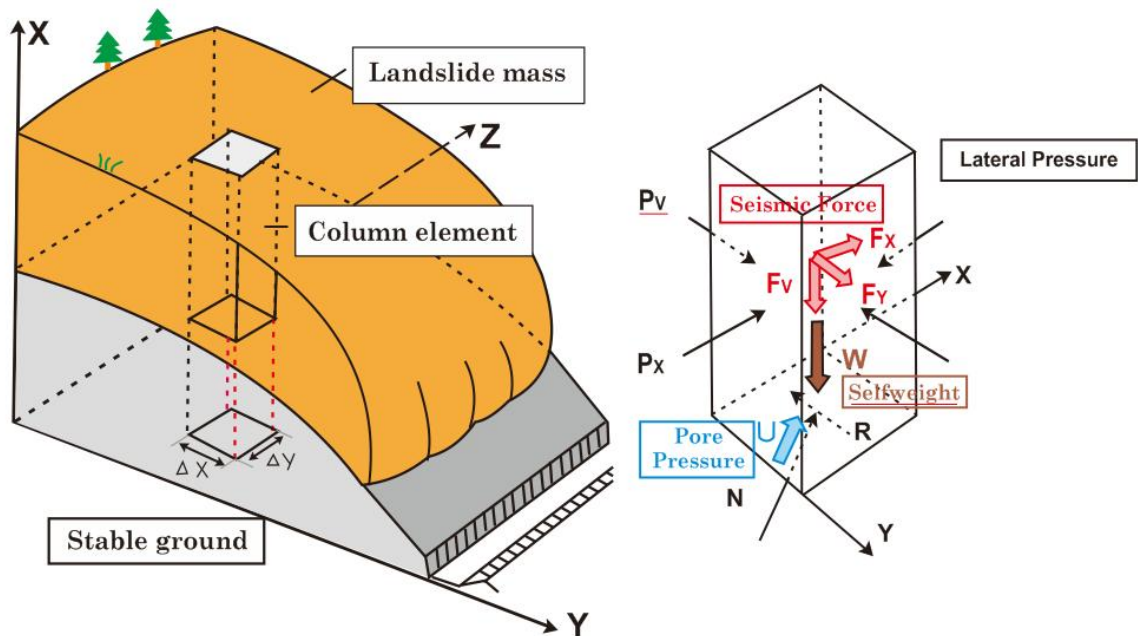


Fig. 4.1 Basic concept of LS-RAPID (from Sassa et al. 2010)

The basic concept of the LS-RAPID simulation model is illustrated in Figure 4.1. In this model, it is considered a vertical imaginary column within a moving landslide mass. All forces acting on the column are determined as followings: (1) self-weight

of column (W), (2) seismic forces (include vertical seismic force F_v , horizontal seismic forces F_x and F_y), (3) lateral pressure acting on the side column walls (P), (4) shear resistance acting on the bottom (R), (5) normal stress acting on the bottom (N), and (6) pore water pressure acting on the bottom (U).

The landslide mass (m) will be accelerated by the acceleration (a) given by the sum of these force: driving force (self-weight + seismic forces) + lateral pressure ratio + shear resistance.

$$am = (W + Fv + Fx + Fy) + \left(\frac{\partial Px}{\partial x} \Delta x + \frac{\partial Py}{\partial y} \Delta y \right) + R \quad (4.1)$$

Where, R includes the effects of forces of N and U in Fig.4.1 and works in the upward direction of the maximum slope line before motion and in the opposite direction of landslide movement during motion.

According to Sassa (1988), the angle of slope is different in the position of column in landslide mass and all stresses and displacements are projected to the horizontal plane and calculated on the plane.

Projection of gravity (g) and vertical seismic acceleration (gKv), and horizontal seismic acceleration acting in x direction (gKx) and y direction (gKy) are shown in Figure 4.2.

Expressing Eq. 4.1 in x and y directions, we obtained Eq. 4.2 and Eq. 4.3. Assuming the total mass of landslide does not change during motion (the sum of landslide mass flowing into a column (M , N) plus the increase of height of soil column is zero), we obtain Eq. 4.4. Equations 4.2, 4.3 and 4.4 are those obtained by Sassa 1988 plus the effects of triggering factors of earthquakes and pore water pressure.

$$\frac{\partial M}{\partial t} + \frac{\partial}{\partial x}(u_o M) + \frac{\partial}{\partial y}(v_o M) = gh \left\{ \frac{\tan \alpha}{q+1} (1 + Kv) + Kx \cos^2 \alpha \right\} - (1 + Kv) kgh \frac{\partial h}{\partial x} - \frac{g}{(q+1)^{\frac{1}{2}}} \cdot \frac{u_o}{(u_o^2 + v_o^2 + w_o^2)} \{ h_c (q + 1) + (1 - r_u) h \tan \phi_a \} \quad (4.2)$$

$$\frac{\partial N}{\partial t} + \frac{\partial}{\partial x}(u_o N) + \frac{\partial}{\partial y}(v_o N) = gh \left\{ \frac{\tan \beta}{q+1} (1 + Kv) + Ky \cos^2 \beta \right\} - (1 + Kv) kgh \frac{\partial h}{\partial y} - \frac{g}{(q+1)^{\frac{1}{2}}} \cdot \frac{u_o}{(u_o^2 + v_o^2 + w_o^2)} \{ h_c (q + 1) + (1 - r_u) h \tan \phi_a \} \quad (4.3)$$

$$\frac{\partial h}{\partial t} + \frac{\partial M}{\partial x} + \frac{\partial N}{\partial y} = 0 \quad (4.4)$$

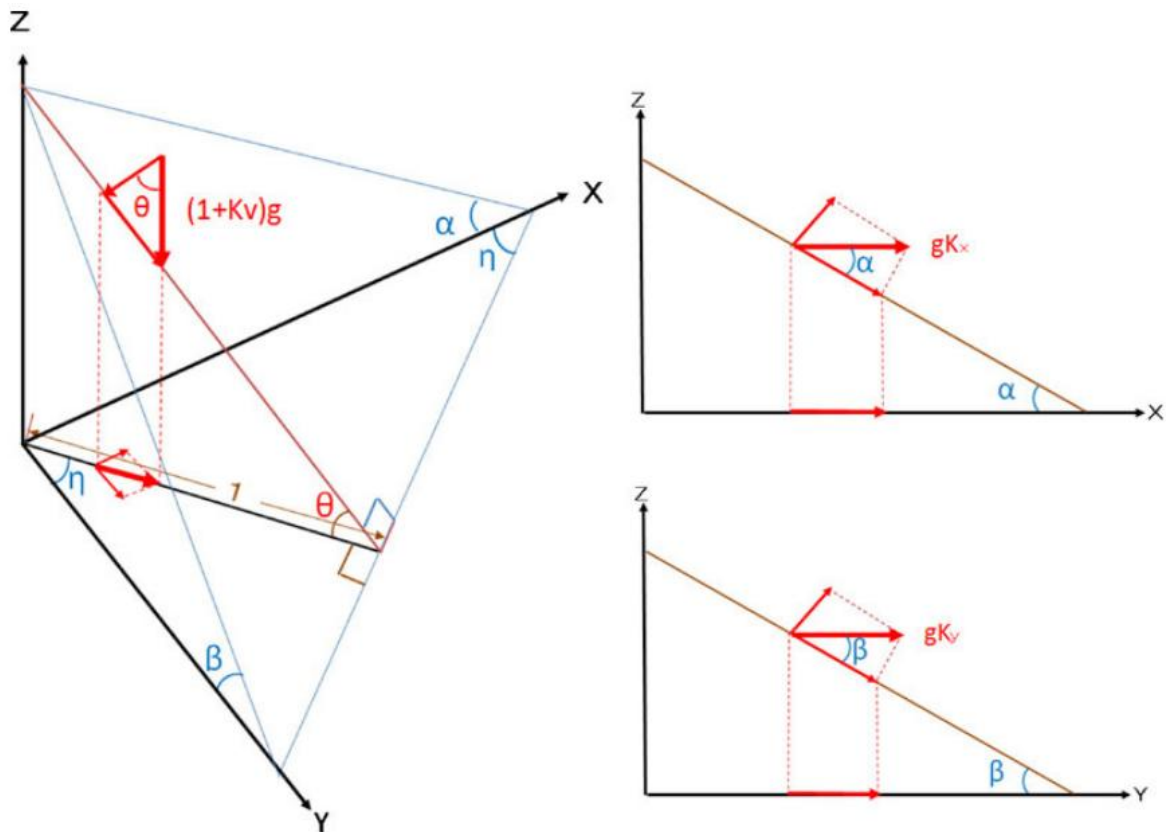


Fig. 4.2 Projection of seismic forces onto the horizontal plane. Left, gravity and vertical seismic force; Right, horizontal seismic forces (x and y directions); K_v , K_x , K_y are seismic coefficients to the vertical, x , and y direction, respectively (Sassa, 2010)

Where,

h is height of soil column within a mesh

g is gravity (acceleration)

α , β are angles of the ground surface to x - z plain and y - z plain, respectively

u_o , v_o , w_o are velocity of a soil column to x , y , z directions, respectively (velocity distribution in z direction is neglected, and regarded to be a constant)

M , N are discharge of soil per unit width in x , y directions, respectively ($M=u_o h$, $N=v_o h$)

k is lateral pressure ratio (ratio of lateral pressure and vertical pressure)

$\tan \phi_a$ is apparent friction coefficient mobilized at the sliding surface of landslide

h_c is cohesion c expressed in the unit of height ($c=\rho g h_c$, ρ is density of soil)

$$q = \tan^2 \alpha + \tan^2 \beta$$

$$w_o = - (u_o \tan \alpha + v_o \tan \beta)$$

K_v , K_x , K_y are seismic coefficients to the vertical, x and y directions

r_u is pore pressure ratio (u/σ)

The initiation process of this model consists of four sub-processes: (1) Initial state in which soil layer exists in a stable condition under the friction coefficient at peak ($\tan \phi_p$); (2) Failure will occur due to the rise of ground water level during rains, seismic loading during earthquakes, or the combination of them; (3) Transient state from peak to steady state in which pore water pressure generation and resulting shear strength reduction in progress with shear displacement; (4) Steady state in which the landslide mass moves with no further strength reduction.

The shear behavior from the pre-failure state to a steady state was described in Figure 4.3. Firstly, the friction angle at peak (ϕ_p) is kept in the pre-failure state until the shear displacement DL (Point of failure, start of strength reduction). In the real slopes, shear stress does not start from zero but it is relatively close to the peak. Then, shear strength will reduce from DL to DU (End of strength reduction) in the shear displacement along a line in the logarithmic axis. Finally, a steady state landslide motion will start under the apparent friction coefficient at steady state ($\tan \phi_{a(ss)}$) after DU in the shear displacement.

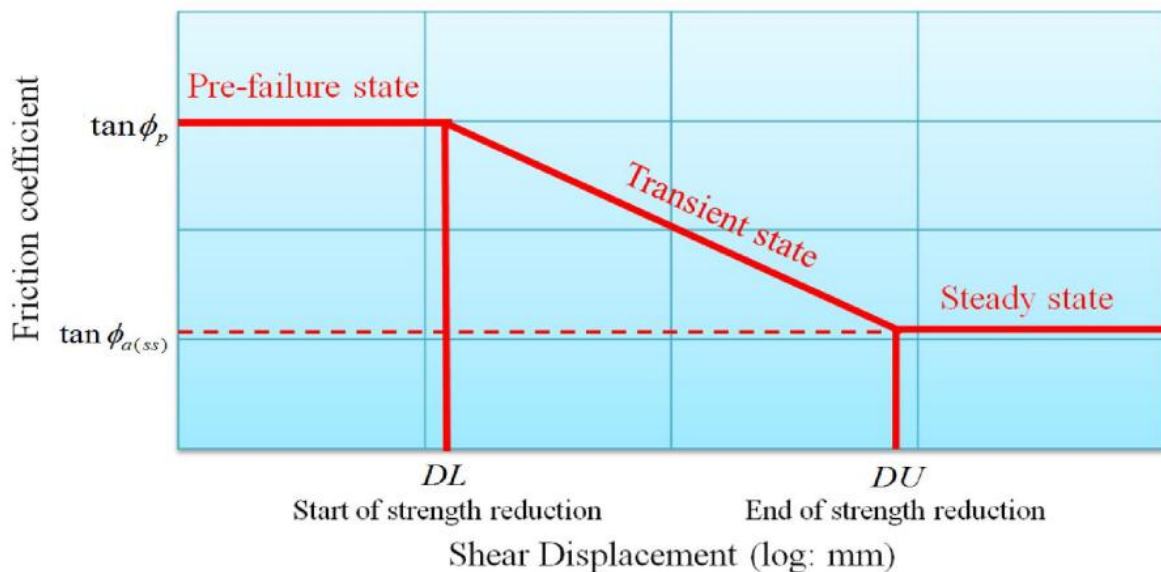


Fig. 4.3 Concept of shear strength reduction in progress of shear displacement (Sassa et al., 2010)

Detailed procedure on generating LS-RAPID format topographical DEM data, creating sliding surface topography, defining soil parameters, setting the landslide simulation conditions, and viewing the results of landslide simulation are presented in the manual of LS-RAPID. Figure 4.4 shows the simulation flow chart for landslide simulation using LS-RAPID (He et al. 2014).

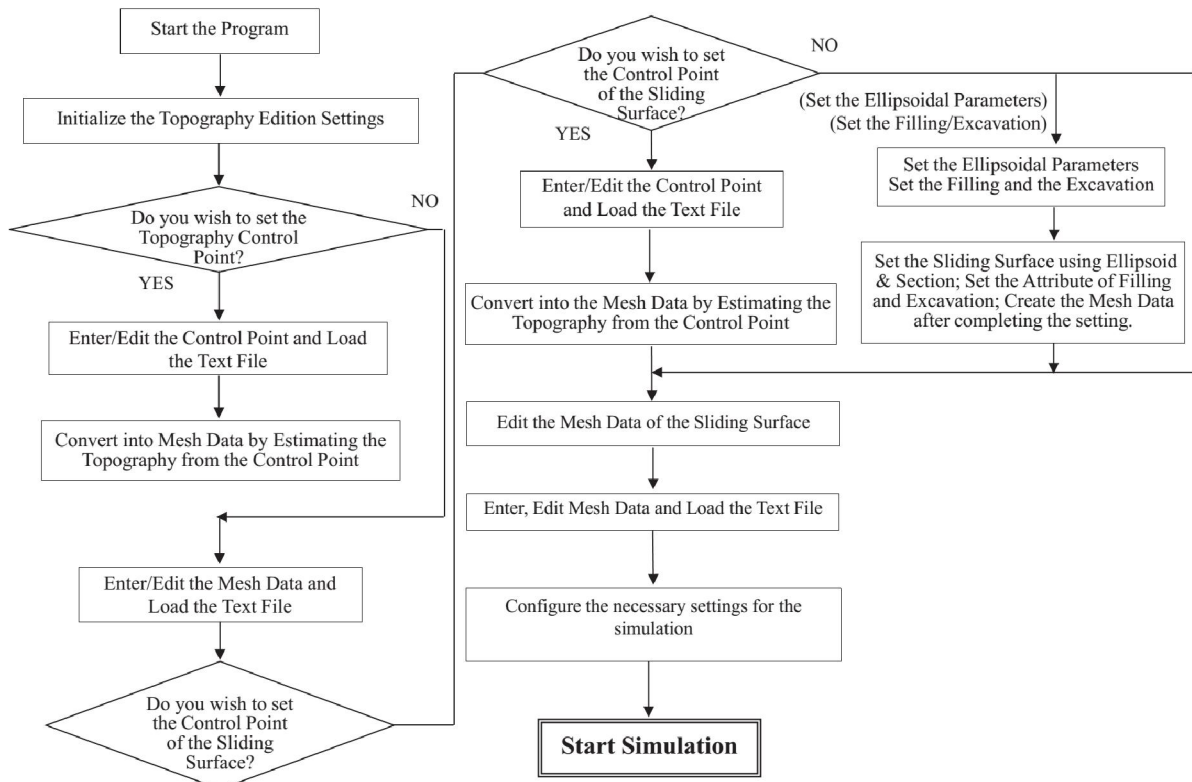


Fig. 4.4 Simulation flow chart for landslide simulation using LS-RAPID (He et al. 2014)

In this research, author applied the LS-RAPID software for simulating the mechanical process of the historical Unzen-Mayuyama landslide in Japan and for hazard assessment of the recent Hai Van station landslide in Vietnam. The first application is to simulate an occurred landslide and compare to the real landslide situation. Therefore, the capability and reliability of the model can be checked. Then, we apply the model to the active landslide and assess the potential hazard caused by that landslide.

4.2. Application for Simulating the Mechanical Process of the 1792 Unzen-Mayuyama Megalandslide in Japan

Firstly, LS-RAPID model was tried to apply to the 1792 Unzen-Mayuyama megalandslide triggered by a nearby earthquake. From the result of the testing and

research presented in previous chapters, the geotechnical parameters obtained in the ring-shear tests and the 2008 Iwate-Miyagi earthquake record were used to simulate in the model. Those parameters are listed in Table 4.1.

- (1) The most important parameter is the steady state shear resistance (τ_{ss}) (Sassa et al. 2010). From the undrained monotonic stress control tests results (Figure 3.17), the steady state shear strength is 120 kPa in the landslide source area (deeper area), and 37-80 kPa in the landslide moving area (shallower area).
- (2) Peak friction angle (ϕ_p) in the tests is from 39.80 to 41.20. The tests were conducted in saturated condition and the maximum loading stress (near 3 MPa- corresponding to less than 200m depth) is smaller than the real stress of the landslide (maximum depth was 400m). So we selected the peak friction angle of 42.0° for this landslide.
- (3) Friction angle during motion is 40.0°
- (4) Critical shear displacement for start of strength reduction (DL) and the start of steady state (DU) are 6 mm and 90 mm. These values were determined from the shear stress and the shear displacement curves for the tests conducted for sample Unzen-1 and Unzen-2 (Figure 4.5)

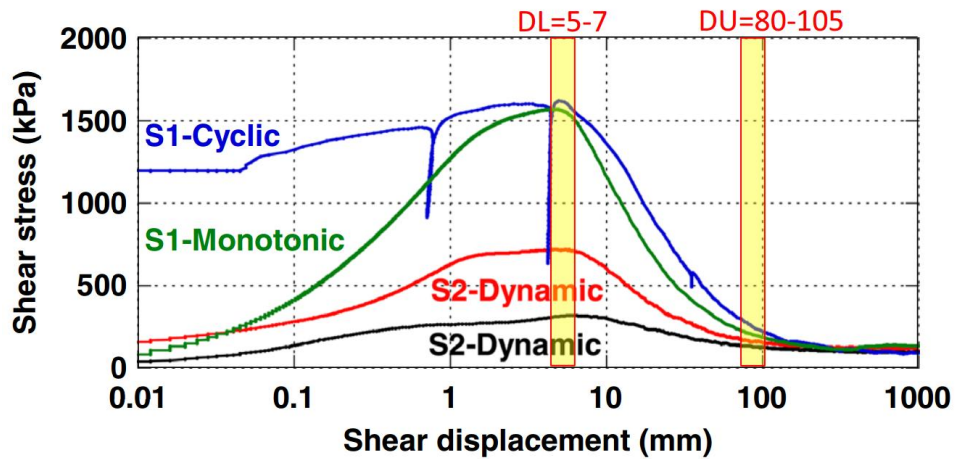


Fig. 4.5 Combined graph of shear strength reduction in progress of shear displacement by different ring-shear test

Table 4.1 Parameters used for Unzen-Mayuyama landslide simulation in LS_RAPID model (from Sassa et al. 2014)

Parameters used in simulation	Value	Source
Parameters of Soils in the source area (Deeper area)		
Steady state shear resistance (τ_{ss})	120 kPa	Test data
Lateral Pressure ratio ($k=\sigma_h/\sigma_v$)	0.7–0.8	Estimation (see text)
Friction angle at peak (ϕ_p)	42.0°	Test data
Cohesion at peak (c)	10 kPa	Assuming small
Friction angle during motion (ϕ_m)	40.0°	Test data
Shear displacement at the start of strength reduction (D_L)	6 mm	Test data
Shear displacement at the start of steady state (D_U)	90 mm	Test data
Pore pressure generation rate (B_{ss})*	0.7–0.9	Estimated
Total unit weight of the mass (γ_t)	19.5 kN/m ³	From the test
Parameters of Soils in the moving area (shallower area)		
Steady state shear resistance (τ_{ss})	30–80 kPa	Test data
Lateral Pressure ratio ($k=\sigma_h/\sigma_v$)	0.8–0.9	Estimated
Friction angle at peak (ϕ_p)	40.0°	Test data
Cohesion at peak (c)	10 kPa	Assuming small
Friction angle during motion (ϕ_m)	40.0°	Test data
Shear displacement at the start of strength reduction (D_L)	6 mm	Test data
Shear displacement at the end of strength reduction (D_U)	90 mm	Test data
Pore pressure generation rate (B_{ss})	0.7–0.9	Estimated
Total unit weight of the mass (γ_t)	19.5 kN/m ³	From the test
Triggering factor		
Excess pore pressure ratio in the fractured zone (r_u)	0.21	Assumption
0.5 times of the 2008 Iwate–Miyagi earthquake	Max:370 cm/s ²	Wave form of the Ground motion record at MYG004
Parameters of the function for non-frictional energy consumption		
Coefficient for non-frictional energy consumption	1.0	Data (Sassa et al. 2010)
Threshold value of velocity	100 m/s	A few times greater than maximum reported speed
Threshold value of soil height	400 m	Maximum depth of the initial source area
Other factors		
Steady state shear resistance under sea	10 kPa	Data (Sassa et al. 2004)
Unit weight of sea water	10.1 kN/m ³	Average sea water density

- (5) Pore-water pressure generation rate (B_{ss}) is 0.7-0.9 in the source area, and 0.99 under the sea because of completely saturation. Outside of the landslide it was 0.2 as the ground was assumed to be unsaturated.
- (6) Lateral pressure ratio (k) is 0.7-0.9. The ratio was assumed to be 0.9 in the coastal area and under the sea. Outside of the landslide, it was 0.4 (unsaturated).
- (7) Unit weight of soils: 19.5 kN/m³, estimated from consolidation of sample and saturated and dry unit weight of sample Unzen-1 (Figure 3.7).
- (8) Pore-water pressure ratio before earth quake was assumed to be 0.21.
- (9) Seismic loading: Iwate-Miyagi earthquake

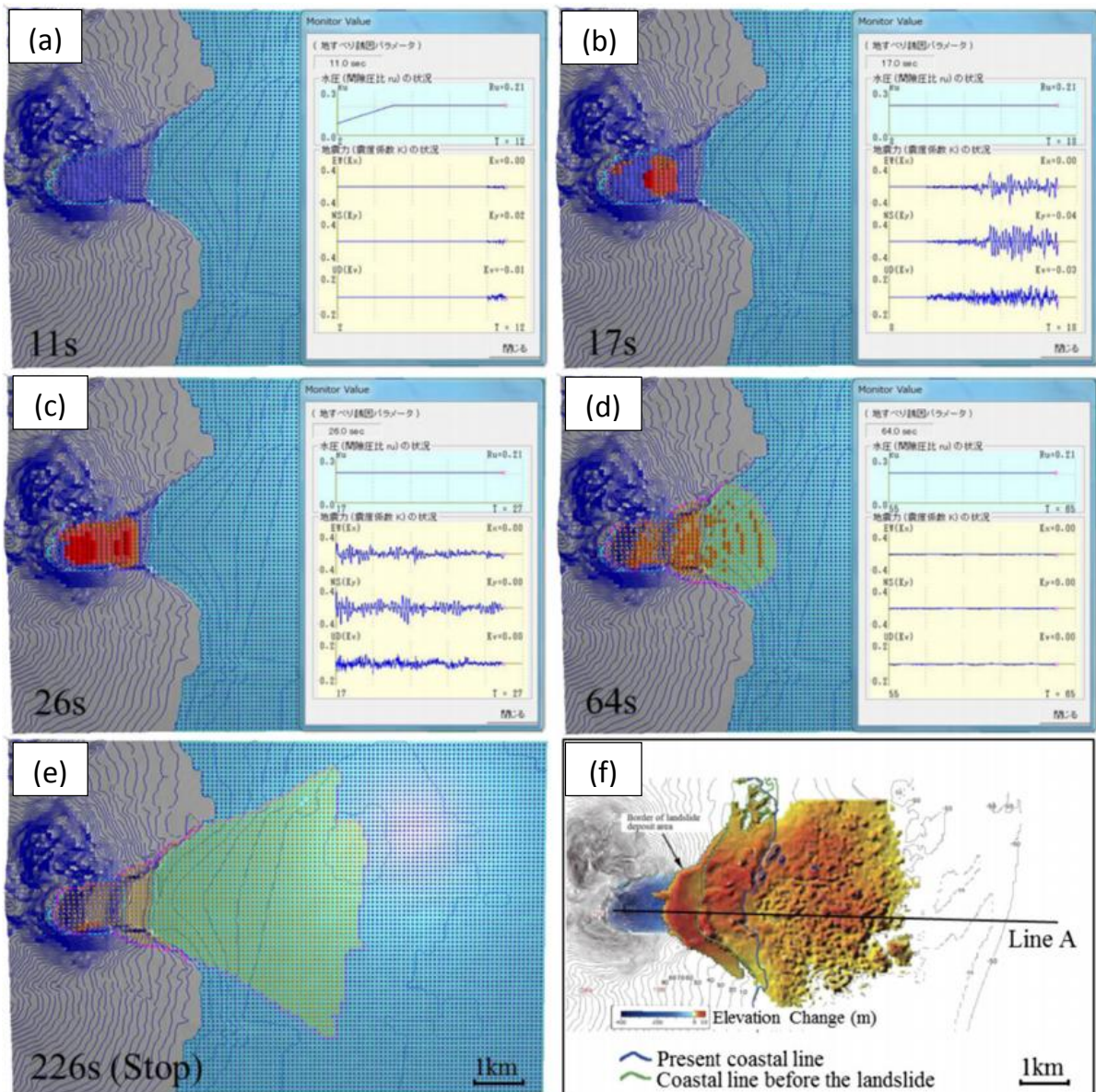


Fig. 4.6 Demonstration of simulation result for the 1792 Unzen–Mayuyama landslide. a-e) the whole process of landslide simulation, f) topographic map

Then, the simulation results are demonstrated in Figure 4.6. Red color ball represent the moving mass, blue color balls represent the stable mass, and light green area presents the deposition area of the landslide. At 11s, the pore-water pressure reached 0.21 and the earthquake started, but no movement occurred. From 17s, the main shock of the Iwate-Miyagi earthquake struck the area, the pore water pressure ratio kept constant of 0.21, and failure was starting from the middle part of the slope and in a small part on the left edge of the slope. At 26s, the whole landslide mass was moving while the earthquake shaking. At 64s, the earthquake already stopped, the landslide mass continued moving and entered into the Shimabara bay. At 226s, the landslide mass stopped and deposited.

Figure 4.6f is the topographic map made by the Unzen Restoration Office of the Ministry of Land, Infrastructure and Transport of Japan (2002). It shows the similar between the area covered by simulated landslide and the actual topography. In addition, the section of line A in the topographic map (Figure 4.6(f)) and the E-W section (same position with line A) of the LS-RAPID model were made to compare (Figure 4.7). The comparison indicated that both movements were very similar. The travel distances of the landslide mass were also very close, in which the travel distance in the simulation is 6.6 km and the real distance from the field investigation is 5.9 km.

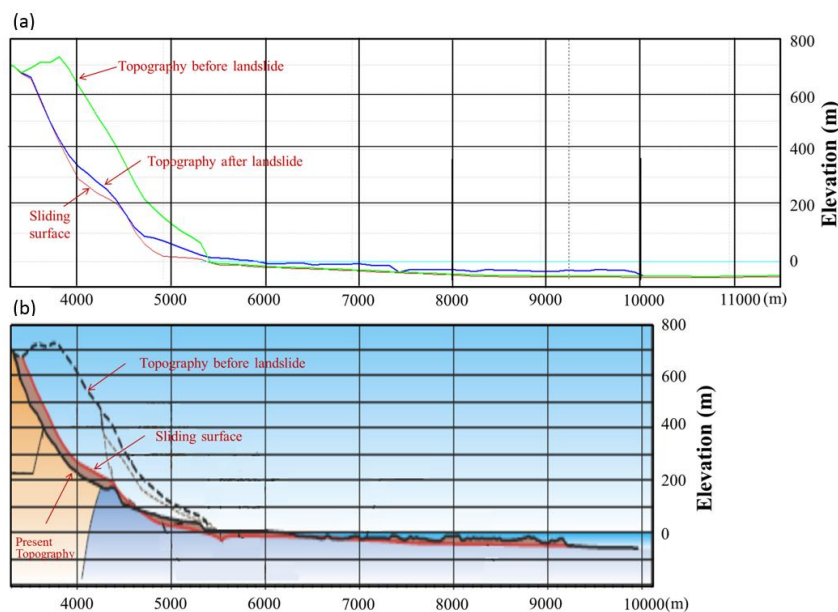


Fig. 4.7 Comparison between simulation result of LC_RAPID (a) and topographic map (b)

4.3. Application for Landslide Hazard Assessment of the Hai Van Station Large-Scale Landslide in Vietnam

The second application of the LS-RAPID model in this research is to an active landslide in Da Nang province, Vietnam. It is expected that the potential hazard of this landslide could be assessed by using the simulation result.

Because of there is almost no earthquake occurred in this study area and landslides are often triggered by rainfall, we conducted the simulation of the Hai Van station landslide in Vietnam by increasing the pore-water pressure ratio (r_u) as the triggering factor.

Firstly, we created a landslide body on the digital map of Hai Van station area by a tool of LS-RAPID as an ellipsoid (Figure 4.8) as following steps: drawing the central

line of landslide (Figure 4.8a), specifying two crossing points of the sliding surface and the ground surface as points (A) and (B) (Figure 4.8b), selecting the location of center of ellipsoid (Figure 4.8b), and selecting one location (x,z) of point C which is located on the ellipsoid line and the x value of center of ellipsoid by monitoring the shape of landslide body (Figure 4.8c).

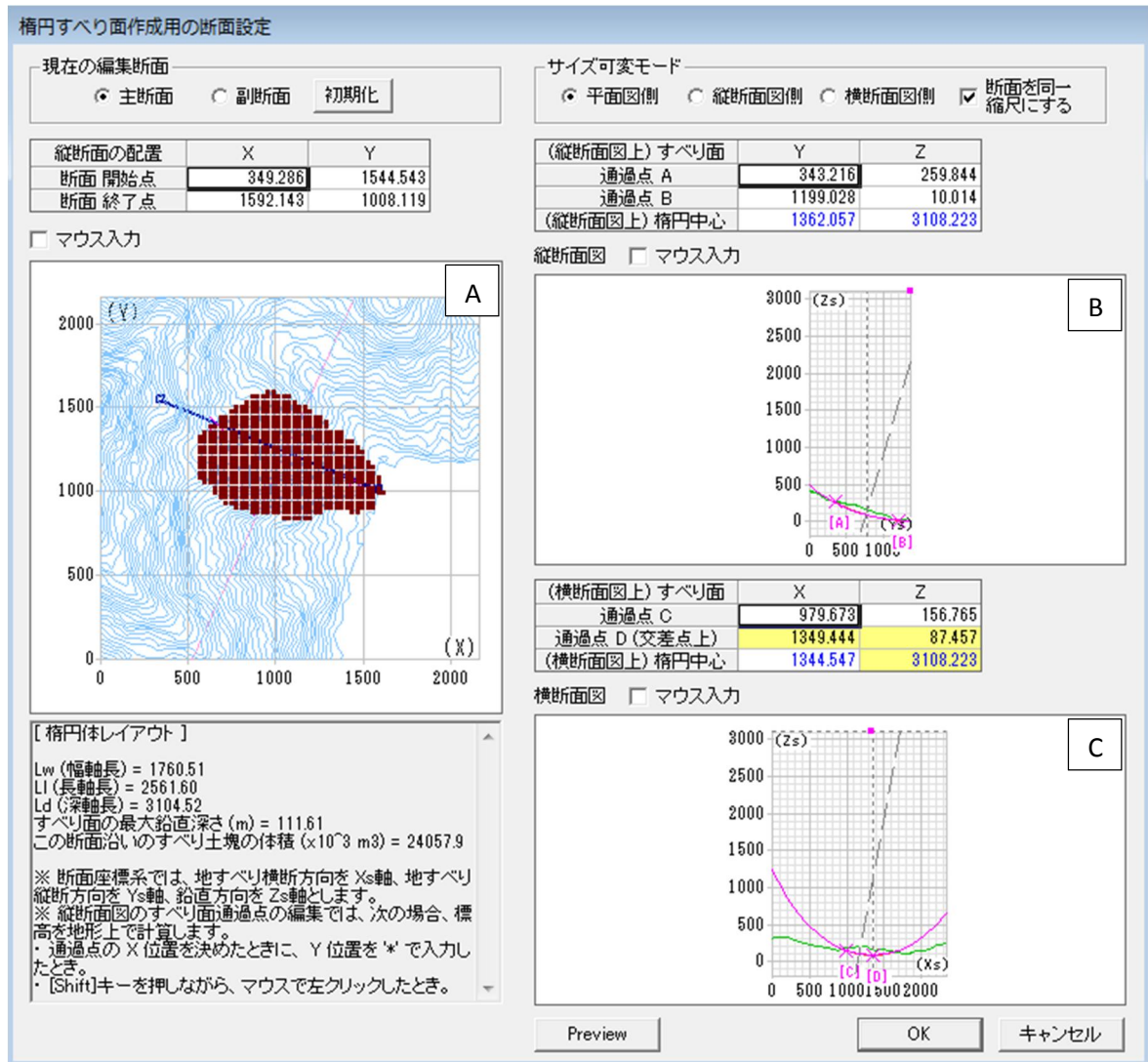


Fig. 4.8 Drawing ellipsoidal sliding surface for Hai Van station landslide

In order to check the drawn landslide body and sliding surface, we created longitudinal and latitudinal crossing section crossing the location of bore hole (yellow point in Figure 3.10 and Figure 4.9) by using “section setting” tool of LS-RAPID. The sections in Figure 4.9 showed that the depth of the sliding surface is around 50 which is appropriate to the loose sand layer from 49.15 to 51m of the drilling log (Figure 3.14).

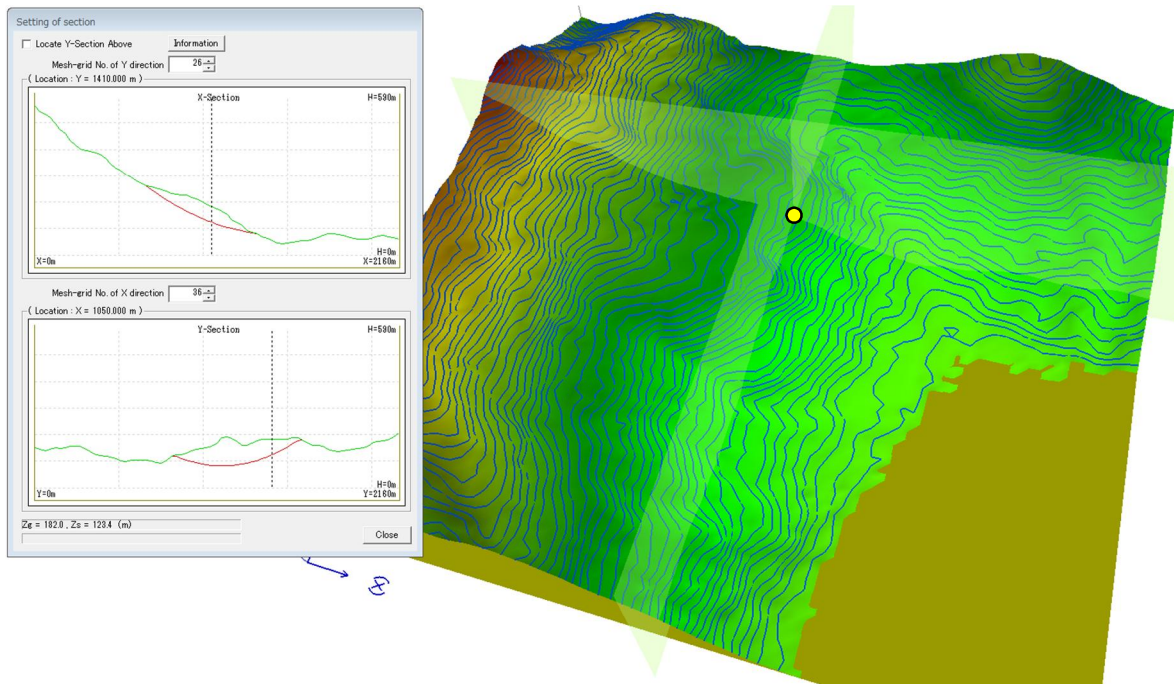


Fig. 4.9 Cross sections passing through the location of the bore hole

The parameters used in the computer simulation are achieved mainly from test results of the new ring-shear apparatus (ICL-2), others were obtained from our field investigation. Those data are list in the Table 4.2.

- (1) The steady-state shear strength (τ_{ss}) of Hai Van-2 sample obtained from the undrained monotonic stress control test under normal stress of 1 MPa (Figure 3.22) is 70 kPa.
- (2) Peak friction angle (ϕ_p) in the tests is from 35.0° to 38.2° (Figure 3.19, 3.22, 3.25) and friction angle during motion is from 33.0° to 36.4° (Figure 3.19 and 3.22). The tests were conducted under fully saturated condition and the loading stresses were from 1.0 MPa to 1.5 MPa corresponding to around 60-80 m deep, while the maximum depth of sliding surface estimated from LS-RAPID model was more than 100 m. The samples taken from the surface may be more weathered than that in this deep landslide body. So we selected the values of peak friction angle and friction angle during motion to input to the computer simulation are 39.0° and 37.0° , respectively.
- (3) According to the drilling logs obtained from the bore holes on the Hai Van station slope, this landslide mass consist alternately of clayey sand layers, silty sand layer, and moderately weathered to highly weather granite layers so the lateral pressure ratio k should be small and we assumed the ratio to be 0.3 for all parts of the Hai Van slope.

- (4) The shear displacement of shear strength reduction was estimated from two undrained stress control tests (one test with normal stress of 1.0 MPa, one test with normal stress of 1.5 MPa). Figure 4.10 shows the critical shear displacement for start of strength reduction (DL) is 4-5 mm and the start of steady state (DU) is 90-102 mm. DL=5 and DU=100 were inputted to the computer simulation.
- (5) The Hai Van landslide body is quite stiff in the top, moderate in the middle, and flat in the lower part so pore-water pressure rate $B_{ss} = 0.2-0.3$ was set in the part of head scarp because it would be not saturated, $B_{ss} = 0.5-0.7$ in the middle part, and $B_{ss} = 0.8-0.9$ in the lower part which is probably saturated.
- (6) As the result presented in Figure 3.16, the saturated unit weight of Hai Van-1 sample and Hai Van-2 sample were 22.2 kN/m^3 and 21.1 kN/m^3 at 400 kPa normal stress and 500 kPa normal stress respectively. The dry unit weight were 17.0 kN/m^3 and 16.5 kN/m^3 . In deeper areas, the value would be higher so a single value of 19 kN/m^3 was chosen to use for the entire area.

Table 4.2 Parameters of Hai Van soil sample used in LS-RAPID simulation

Parameters	Value	Source
Steady state shear resistance (τ_{ss} , kPa)	70	Test data
Lateral pressure ratio ($k=\sigma_h/\sigma_v$)	0.3	Estimation
Friction angle at peak (ϕ_p , degree)	39.0	Test data
Cohesion at peak (c , kPa)	30	Estimation
Friction angle during motion (ϕ_m , degree)	37	Test data
Shear displacement at the start of strength reduction (DL, mm)	5	Test data
Shear displacement at the start of steady state (DU, mm)	100	Test data
Pore pressure generation rate (B_{ss})	0.2-0.9	Estimation
Total unit weight of the mass (γ_t , kN/m^3)	19	Test data
Excess pore pressure ratio in the fractured zone (r_u)	0.5	Test data
Slope angle (θ , degree)	20-25	Investigation
Landslide depth (H , m)	100-120	Investigation
Unit weight of water (γ_w , N/m^3)	9.8	Normal value

(7) The pore water pressure control ring shear test on Hai Van-2 sample (Figure 3.25) indicated that pore pressure ratio $r_u = 0.49$ would trigger the landslide in Hai Van area. So we increased the value of r_u from 0 to 0.5 in the computer simulation as the triggering factor of the landslide.

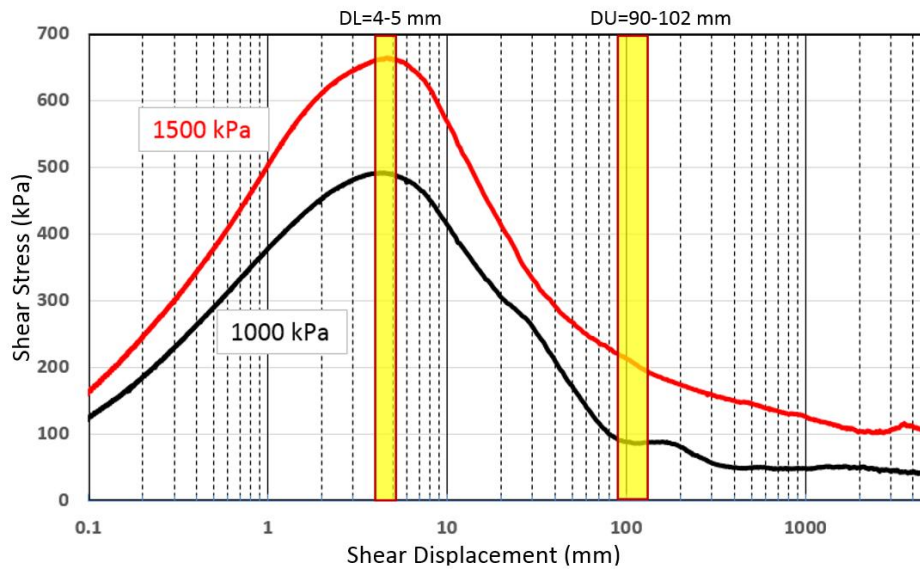


Fig. 4.10 Shear resistance and shear displacement of Hai Van-2 sample from undrained stress control tests

The simulation result of the Hai Van station landslide is presented in Figure 4. 11. In Figure 4.11A, bright green line is the landslide border and blue color balls present the current state of the Hai Van slope. Then, pore-water pressure ratio was increased and failure started from the right-middle of the slope when r_u reached 0.31 at 37.8s (red color balls, Figure 4.11B, C). At 47.5s, r_u reached 0.40 and failure spread the lower half of the slope with velocity of 9.2 m/s (Figure 4.11D). At 59.5s, r_u reached 0.50 and kept constant until the end of the simulation. At 69.3s, the whole landslide mass was formed and moved down with the velocity of 19.1m/s (Figure 4.9F). At 84.5s, the simulated landslide mass continued moving to the Da Nang sea with the maximum velocity of 20.4m/s (Figure 4.9G) and stopped moving ($v=0$ m/s) after 123.7s (Figure 4.11H).

Figure 4.12 shows central sections of the Hai Van landslide. Current ground surface before landslide, sliding surface, and ground surface after simulation are also presented. As a result, the total landslide volume and the vertical maximum depth of the landslide were calculated to be $24057.9 \times 10^3 \text{ m}^3$ and 111 m.

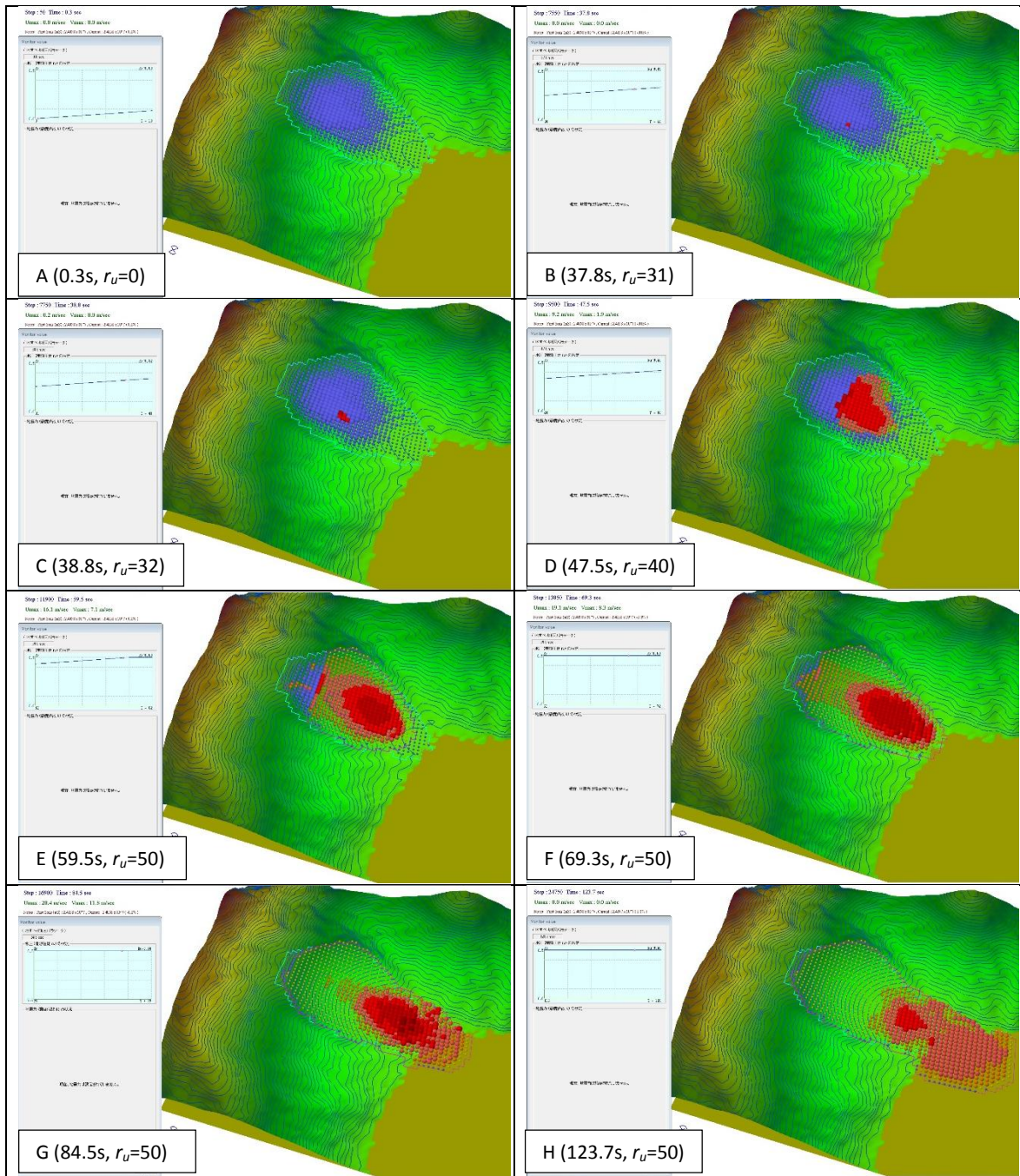


Fig. 4.11 Demonstration of simulation result for the active Hai Van station landslide

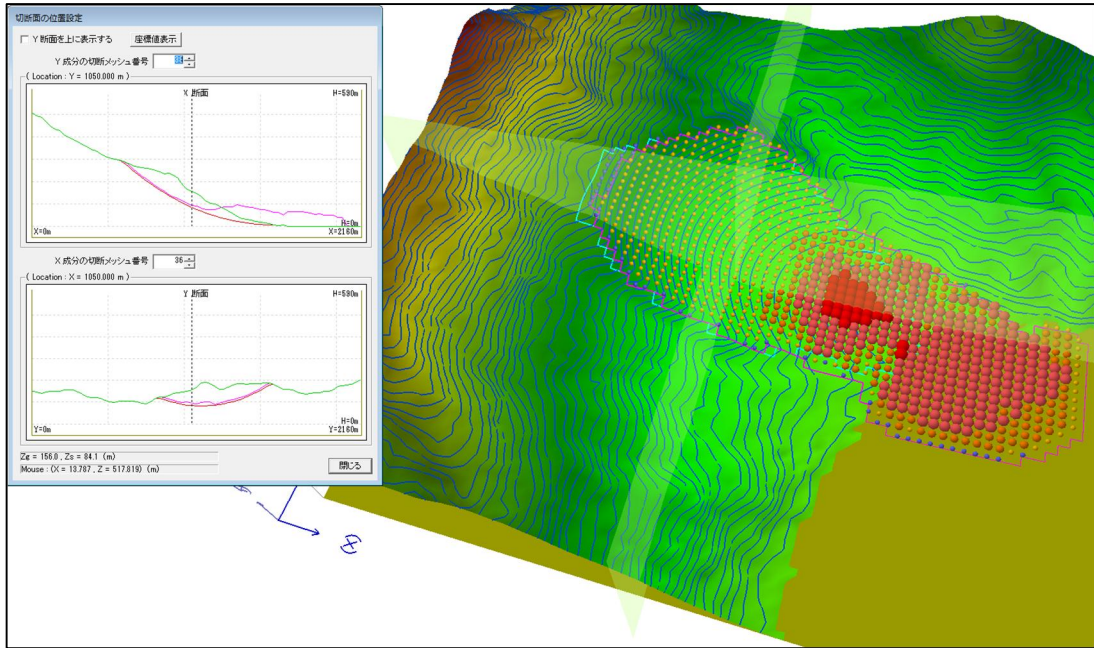


Fig. 4.12 Central sections of Hai Van station landslide (Green line presents current ground surface before landslide; Red line presents the sliding surface; and pink line shows the ground surface left after landslide simulation)

Chapter 5 Conclusions

Since 1984, a new series of ring-shear apparatus from DPRI-1 to DPRI-7, ICL-1 and ICL-2 have been designed and developed by professor Sassa and his colleagues. The author had a great opportunity for contributing to develop ICL-2. Among these apparatuses, DPRI-1 is the initial high-speed ring-shear apparatus using a conventional shear-speed control motor. DPRI-3 is the first dynamic-loading ring-shear apparatus to reproduce seismic loading using a shear torque-control motor, air piston, gap control motor under the servo-control system of all stresses. Model DPRI-5 and DPRI-6 were developed to simulate earthquake-induced landslide using the real seismic record to study a rapid disastrous landslide triggered by the 1995 Hyogo-ken Nambu earthquake. They succeeded in reproducing the formation of a sliding surface within the apparatus and measuring post-failure motion in rain- or earthquake-induced landslides. However, the maximum undrained capacities in the DPRI devices ranged from 300 to 650 kPa.

In 2011, ICL-1 was developed as a part of Japan-Croatia research project. This is a transportable apparatus within three counterpart universities. There have been more and more megaslides and large-scale landslides causing many severe disasters in the world. For studying those large-scale landslide, it is needed to develop a new apparatus which can test under a high stress state. ICL-2 was developed to simulate the initiation and motion of megaslides and large-scale landslide of more than 100m in thickness. The undrained capacity as well as the maximum loading normal stress of ICL-2 is 3 MPa.

The concept, design, construction and testing procedures of the latest ring-shear apparatus ICL-2 were presented in chapter 2. Then, in chapter 3, two real cases of large-scale landslide were applied to ICL-2. The first is the historical 1792 Unzen-Mayuyama megaslide in Japan triggered by an earthquake and the second is the active Hai Van large-scale landslide in Viet Nam. A series of tests were conducted on the samples taken from those two landslides to examine the performance of the new high-stress ring-shear apparatus as well as to simulate initiation and motion of the landslides. Finally, in chapter 4, all parameters measured from the undrained ring-shear tests were inputted to the integrated landslide simulation model (LS-RAPID). In case of the former landslide, we input the initial pore-water pressure ratio before

the triggering earthquake $r_u = 0.21$, then gave the seismic record of the 2008 Iwate-Miyagi earthquake (maximum acceleration = 370 cm/s^2) into the LS-RAPID as triggering factor. In case of the latter landslide, we simulated rain-induced landslide. So we increased a pore-water pressure ratio up to $r_u = 0.5$ as the triggering factor and other parameters obtained from the ring-shear tests and our field investigation to the computer simulation. The mechanism and hazard area of the landslides have been well demonstrated.

The main conclusions of this research are as follows:

1. A new high-stress dynamic-loading ring-shear apparatus was developed with the following advanced characteristics compared to previous ring-shear devices.

- (1) The greatest difference between ICL-2 device and others in DPRI series is the system for loading normal stress. Normal stress was loaded from the long loading frame over the shear box in DPRI Series. While Normal stress was loaded by pulling the central axis of shear box in ICL-2. The deformation of loading parts during changing stresses are much smaller in ICL-2, it enabled to make a higher undrained capability.
- (2) Another difference is the rubber edge which has a critical role for sealing. Rubber edges of all DPRI series apparatus were glued to the shear box. A constant thickness of glue is impossible to achieve and the height of the upper surfaces of the rubber edges of the inner ring and the outer ring must be the equal to maintain an undrained condition. Therefore, the rubber edge was made smooth by a lathe machine in a company or a specific file tool by a professional engineer. But this process is not easy to be conducted aboard. In the ICL series, the rubber edge is simply placed on the lower ring and pressed by a Teflon ring holder, and this holder is pressed in turn by a steel ring holder fixed by a set of screws. Smoothing process by lathe or file is not needed.
- (3) Difference of ICL-1 and ICL-2 is capacity of normal stress and shear speed. Maximum shear speed of ICL-1 is 5.4 cm/sec , the maximum normal stress and the undrained capacity is 1 MPa . ICL-2 has a higher capacity of shear speed (50 cm/sec) and the maximum normal stress and undrained capacity is 3 MPa .

2. Major test results using this new apparatus are as follows.

- (1) Undrained tests were successful up to 3 MPa in the monotonic speed-control test, monotonic stress control test, pore-water pressure control test, cyclic-shear-stress loading test and seismic-shear-stress loading test using the real earthquake records. Undrained monotonic loading tests were conducted on the same sample of the Unzen-Mayuyama landslide under difference normal stresses ranging from 300 kPa to 3 MPa. The friction angle during motion was almost constant of around 39.80 and the undrained steady state shear resistance was from 37 to 120 kPa. In case of the sample from Hai Van landslide tested under 1 MPa normal stress, the friction angle during motion and the steady state shear resistance were 36.40 and 70 kPa, respectively.
- (2) The pore-water pressure control tests for simulating the landslides suggested that a pore-water pressure ratio of 0.4 in case of Unzen sample and 0.49 in case of Hai Van sample could trigger landslide without an earthquake. And the undrained seismic loading test on Unzen sample under a pore-water pressure ratio of 0.27 showed that the Unzen-Mayuyama landslide could be initiated by a seismic acceleration of 216 cm/s².

3. The results of computer simulations using the measured parameters for the Unzen Mayuyama landslide in Japan and the Hai van Landslide in Viet Nam are:

- (1) The historical Unzen-Mayuyama landslide was well simulated in which the landslide hazard area and its central section were similar to those surveyed by the Unzen Restoration Office of the Ministry of Land, Infrastructure and Transport of Japan. The travel distances of the simulated landslide and actual landslide were also very similar (6.6 km in simulation and 5.9 km in reality). This application of the new ring shear apparatus (ICL-2) to the large-scale landslides proved that the apparatus and the integrated computer simulation (LS-RAPID) are reliable and effective tools for simulating the mechanism of the large-scale landslides and assessing their hazard.
- (2) In the computer simulation of the active landslide in Viet Nam, failure started from a middle point of the slope when the pore-water pressure ratio (r_u) reached the value of 0.31. Then, the pressure ration was kept increasing until 0.50 and failure spread over the slope due to progressive failure. Finally, the whole landslide mass has been formed and moved down to the sea with the maximum velocity of 20.4 m/s. The total landslide volume and the vertical

maximum depth of the landslide were calculated to be $24057.9 \times 10^3 \text{ m}^3$ and 111 m, respectively.

The triggering factor of this landslide is rainfall causing pore water pressure ratio of 0.31 or higher. Using this value and combining with rainfall data and monitored pore water pressure in bore holes, we can predict the time of this landslide, thereby reduce landslide disaster.

Content of this thesis are mainly based on papers as follows:

1. Dang K, Sassa K, He B, Nagai O (2014) Test results of a new high-stress ring-shear apparatus (ICL-2) developed for Vietnam Project. Proceedings of SATREPS Workshop on Landslide Risk Assessment Technology, 29-30 July 2014, Hanoi, Vietnam, pp. 32-41
2. Dang K, Sassa K, Duc DM, Tien DV (2014) Landslides in Vietnam and the JICA - JST joint research project for landslide disaster reduction. Proceedings of the 1st regional symposium on landslides in the Adriatic-Balkan region, pp. 193-197.
3. Sassa K, Dang K, He B, Takara K, Inoue K, Nagai O (2014) Development of a new high-stress undrained ring-shear apparatus and its application to the 1792 Unzen-Mayuyama megaslide in Japan. *Landslides*, Vol.11, No.5, pp. 827-842.
4. Sassa K, He B, Dang K, Nagai O and Takara K (2014) Plenary: progress in Landslide Dynamics. *Landslide Science for a Safer Geoenvironment* (Sassa, Canuti, Yin, eds), Vol.1, pp.37-67.

References

1. Anderson MG, Holcombe E (2013) Community-based landslide risk reduction: managing disasters in small steps. Washington, D.C.: World Bank. Doi: 10.1596/978-0-8213-9456-4.
2. Asano S, Abe S, Nagai O (2014) Development of landslide monitoring and data transfer system in the Hai Van station landslide and the initial extensometer monitoring result behind the station. Proceedings of the SATREPS workshop on landslides in Vietnam, pp. 190-194.
3. Bishop AW, Green GE, Garga VK, Anderson A, Brown JD (1971) A new ring-shear apparatus and its application to the measurement of the residual strength. *Geotechnique*, Vol. 21, No. 4, pp. 273-328.
4. Bromhead EN (1979) A simple ring-shear apparatus. *Ground Engineering*, Vol. 12, No. 5, pp. 40-44.
5. Dang K, Sassa K, Duc DM, Tien DV (2014) Landslides in Vietnam and the JICA - JST Joint Research Project for Landslide Disaster Reduction. Proceedings of the 1st Regional Symposium on Landslides in the Adriatic-Balkan Region, pp. 193-197.
6. Dang K, Sassa K, He B, Nagai O (2014) Test results of a new high-stress ring-shear apparatus (ICL-2) developed for Vietnam project. Proceedings of SATREPS Workshop on Landslide Risk Assessment Technology, 29-30 July 2014, Hanoi, Vietnam, pp. 32-41.
7. Gradiski K, Sassa K, He B, Arbanas Z, Arbanas S M, Krkac M, Kvasnicka P, Ostric M (2014) Application of integrated landslide simulation model LS-RAPID to the Kostanjek landslide, Zagreb, Croatia. Proceedings of the 1st Regional Symposium on Landslides in the Adriatic-Balkan Region, pp. 11-16.
8. Garga VK, Sendano JI (2002) Steady state strength of sands in a constant volume ring shear apparatus. *Geotech Test J* 25(4):414–421
9. Gibo S (1994) Ring shear apparatus for measuring residual strengths and its measurement accuracy. *Journal of Japan Landslide Society* 31(3):24–30.
10. He B, Sassa K, Nagai O, Takara K (2014) Manual of LS-RAPID numerical simulation model for landslide teaching and research. Proceedings of Proceedings of the 1st Regional Symposium on Landslides in the Adriatic-Balkan Region, pp. 5-10.
11. Lam HQ, Dang K, Pham VT, Doan HL, Nguyen KT, (2014) Recent Development of the New High-stress Undrained Ring-shear Apparatus (ICL-

- 2) and its Application. Proceeding of SATREPS 2014 Workshop “Landslide Risk Assessment Technology”, 29-30 July 2014, Hanoi, Vietnam, pp: 168-173
12. Loi DH (2015) Study on the 2014 Hiroshima landslide disasters using ring-shear. Master thesis, Graduate School of Engineering, Kyoto University.
 13. Mai DT, Thanh NT (2005) Precipitation extremes over Vietnam. The 5th International Scientific Conference on the Global Energy and Water Cycle, 20-24 June 2005. Orange County, California, American, 4 pages.
 14. Ostric M, Liutic K, Krkac M, Sassa K, Bin H, Takara K, Yamashiki Y (2012) Portable ring shear apparatus and its application on Croatia landslides. *Annals of Disaster Prevention Research Institute, Kyoto University*, No. 55B, pp. 57-65.
 15. Ostric M (2013) Development of portable un-drained ring-shear apparatus and its application. Doctoral Thesis, Graduate School of Engineering, Kyoto University. 127 pages.
 16. Phuc LD (2009) Granitoid petrology of Hai Van massif. *Science & technology development*, Vol 12, No.05, pp. 46-54 (in Vietnamese).
 17. Petley DN, Allison RJ (1997) The mechanics of deep-seated landslides. *Earth surface processes and landforms*, Vol 22, pp 747-758.
 18. Sassa K (1984) The mechanism starting liquefied landslides and debris flows. *Proceedings of 4th International Symposium on Landslides*, Toronto, June, pp. 349-354.
 19. Sassa K (1988) Motion of Landslides and Debris Flows-Prediction of hazard area. Report for Grant-in-Aid for Scientific Research by Japanese Ministry on Education, Science and Culture (Project No. 61480062), pp.15.
 20. Sassa K (1988) Geotechnical model for the motion of landslides. Special Lecture of 5th International Symposium on Landslides, "Landslides", 1. Rotterdam: Balkema. 37-55
 21. Sassa K (1992) Keynote lecture: Access to the dynamics of landslides during earthquakes by a new cyclic loading high-speed ring shear apparatus. *Proc. of the 6th International Symposium on Landslides*, In "Landslides" Balkema, Vol.3, pp.1919-1938.
 22. Sassa K (1994) Development of a new cyclic loading ring shear apparatus to study earthquake-induced-landslides. Report for Grant-in-Aid for Developmental Scientific Research by the Ministry on Education, Science and Culture, Japan (Project No. 03556021), pp.1-106.

23. Sassa K (1996) Prediction of earthquake induced landslides. Proceedings of 7th International Symposium on Landslides, A.A. Balkema, Trondheim, 17–21 June, pp.115-132.
24. Sassa K, Dang K, He B, Takara K, Inoue K, Nagai O (2014) Development of a new high-stress undrained ring-shear apparatus and its application to the 1792 Unzen-Mayuyama megaslide in Japan. *Landslide*, Vol.11, No.5, pp. 827-842.
25. Sassa K, Fukuoka H, Wang G, Ishikawa N (2004) Un-drained dynamic-loading ring-shear apparatus and its application to landslide dynamics. *Landslides*, 1(1), pp. 7-19.
26. Sassa K, Fukuoka H, Scarascia-Mugnozza G, Evans S (1996) Earthquake induced-landslides: distribution, motion and mechanisms. Special Issue for the Great Hanshin Earthquake Disasters, *Soils and Foundations*, pp. 53-64.
27. Sassa K, Fukuoka H, Wang GH, Ishikawa N (2004) Undrained Dynamic-loading Ring Shear Apparatus and its Application to Landslide Dynamics. *Landslides*, Vol. 1, No. 1, pp. 7-19.
28. Sassa K, He B, Dang K, Nagai O and Takara K (2014) Plenary: progress in Landslide Dynamics. *Landslide Science for a Safer Geoenvironment* (Sassa, Canuti, Yin, eds), Vol.1, pp.37-67.
29. Sassa K, He B (2013) TXT-Tool 3.081-1.1 Landslide initiation mechanism. *ICL Landslide Teaching Tools*: 205-213.
30. Sassa K, He B (2013) TXT-Tool 3.081-1.2 Landslide dynamics. *ICL Landslide Teaching Tools*: 215-237.
31. Sassa K, He B, Miyagi T, Strasser M, Konagai K, Ostric M, Setiawan H, Takara K, Nagai O, Yamashiki Y, Tutumi S (2012) A hypothesis of the Senoumi submarine megaslide in Suruga Bay in Japan—based on the undrained dynamic-loading ring-shear tests and computer simulation," *Landslides*, Vol. 9, No. 4, pp. 439-455.
32. Savage SB, Sayed M (1984) Stresses developed in dry cohesionless granular materials sheared in an annular shear cell. *Jorunal of Fluid Mech*, Vol. 142, pp. 391-430.
33. Sedano, J.A.I., Vanapalli, S.K. and Garga V.K., 2007, "Modified Ring-shear Apparatus for Unsaturated Soils Testing," *Geotech. Test. J.*, Vol. 30, No. 1, pp. 39-47.
34. Shimizu, H., Matsushima, T., Nakada, S., Fujii, T., Hoshizumi, H., Takarada, S., Miyabuchi, Y., Ui, T., Miyake, Y., Sugimoto, T., Nagai, D., 2007, Unzen

- eruption: Disaster and recovery. Intra meeting excursion of Shimabara 2007
Cities on volcanoes 5 conference, 28p.
35. Stark TD, Eid HT (1993) Modified Bromhead ring shear test procedure. *Geotech. Test. J.*, Vol. 16, No. 1, pp. 100-107.
 36. Stark TD, Poeppel AR (1994) Landfill liner interface strengths from torsional ring-shear tests. *Journal of Geotechnical Engineering Division, ASCE*, Vol. 120, No. 3, pp. 597-615.
 37. Stark TD, Contreras IA (1996) Constant Volume Ring-shear Apparatus. *Geotech. Test. J.*, Vol. 19, No. 1, pp. 3-11.
 38. Tien, P.V. (2015) Analyzing Failure Characteristics and Potential of Landslides in Hai Van Mountain, Vietnam. Master thesis, Graduate School of Engineering, Kyoto University.
 39. Tika TE, Vaughan PR, Lemos LJ (1996) Fast shearing of preexisting shear zones in soil. *Geotechnique*, Vol. 46, No. 2, pp. 197-223.
 40. Tika TM (1989) The effect of rate of shear on the residual strength of soil. PhD thesis, University of London (Imperial College of Science and Technology), 494 p.
 41. <http://landslides.usgs.gov/learn/majorls.php>
 42. http://en.wikipedia.org/wiki/List_of_landslides
 43. http://en.wikipedia.org/wiki/1792_Unzen_earthquake_and_tsunami